Alma Mater Studiorum · Università di Bologna

Scuola di Scienze
Corso di Laurea Magistrale in Fisica

ZOOMED SIMULATIONS OF HALO SEGREGATION IN COSMOLOGICAL MODELS WITH TWO SPECIES OF COUPLED DARK MATTER

Relatore:
Prof. LAURO MOSCARDINI

Presentata da:
ENRICO GARALDI

Correlatore:
Dr. MARCO BALDI

Sessione II
Anno Accademico 2013/2014

Abstract

The ordinary matter accounts only for a few percent of the total mass-energy density of the Universe, which is largely dominated by some "dark" components. The standard way to describe this cosmic Dark Sector is through the ΛCDM model. Although it appears to be consistent with most of the presently available data, it also presents some fundamental problems that have so far remained unsolved, which leave room for studying different cosmological models.

In this Thesis I aim to investigate a recently-proposed model of Dark Sector, called the "Multi-coupled Dark Energy" (McDE), which features modified interactions with respect to the standard ΛCDM model. In particular, in this model the Dark Matter is composed by two different types of particles with opposite couplings to a scalar field that accounts for the Dark Energy. The background and linear perturbations evolution of this model are indistinguishable from the ones of the standard ΛCDM model.

In the present Thesis a series of zoomed numerical simulations of the McDE model are presented for the first time. They feature a number of regions with different resolution, centred on a single halo, which allow to study in detail a single structure of interest without dramatically increasing the computational time needed.

A code called ZInCo, developed appositely for the purposes of this Thesis, is also presented. The code produces initial conditions suitable for cosmological simulations, featuring regions of different resolution, independent from the cosmological model being studied and preserving all the prominent features of the power spectrum imposed.

The ZInCo code was used to produce initial conditions for a series of zoomed numerical simulations of the McDE model, which show for the first time, thanks to the higher resolution reached in the region of interest, that the segregation effect, typical of this model, occurs significantly earlier than previously estimated. Moreover, the radial density profiles obtained show a flattened centre in the early stages of the segregation. The latter effect could help solving the "cusp-core" problem of the ΛCDM model and place constraints on the possible values of the coupling strength.

Sommario

La materia ordinaria copre soli pochi punti percentuali della massa-energia totale dell'Universo, che è invece largamente dominata da componenti "oscure". Il modello standard usato per descriverle è il modello ΛCDM. Nonostante esso sembri consistente con la maggior parte dei dati attualmente disponibili, presenta alcuni problemi fondamentali che ad oggi restano irrisolti, lasciando spazio per lo studio di modelli cosmologici alternativi.

Questa Tesi mira a studiare un modello proposto recentemente, chiamato "Multi-coupled Dark Energy" (McDE), che presenta interazioni modificate rispetto al modello ΛCDM. In particolare, la Materia Oscura è composta da due diversi tipi di particelle con accoppiamento opposto rispetto ad un campo scalare responsabile dell'Energia Oscura. L'evoluzione del background e delle perturbazioni lineari risultano essere indistinguibili da quelle del modello ΛCDM.

In questa Tesi viene presentata per la prima volta una serie di simulazioni numeriche "zoomed". Esse presentano diverse regioni con risoluzione differente, centrate su un singolo ammasso di interesse, che permettono di studiare in dettaglio una singola struttura senza aumentare eccessivamente il tempo di calcolo necessario.

Un codice chiamato ZInCo, da me appositamente sviluppato per questa Tesi, viene anch'esso presentato per la prima volta. Il codice produce condizioni iniziali adatte a simulazioni cosmologiche, con differenti regioni di risoluzione, indipendenti dal modello cosmologico scelto e che preservano tutte le caratteristiche dello spettro di potenza imposto su di esse.

Il codice ZInCo è stato usato per produrre condizioni iniziali per una serie di simulazioni numeriche del modello McDE, le quali per la prima volta mostrano, grazie all'alta risoluzione raggiunta, che l'effetto di segregazione degli ammassi avviene significativamente prima di quanto stimato in precedenza. Inoltre, i profili radiale di densità ottenuti mostrano un appiattimento centrale nelle fasi iniziali della segregazione. Quest'ultimo effetto potrebbe aiutare a risolvere il problema "cusp-core" del modello LambdaCDM e porre limiti ai valori dell'accoppiamento possibili.

Contents

1 Introduction 1
- 1.1 The ΛCDM Model . . . 2
  - 1.1.1 From the Cosmological Principle to the Dark Sector problem . . . 2
  - 1.1.2 The Cosmological Standard Model . . . 8
- 1.2 Observational Evidence . . . 10
  - 1.2.1 Dark Matter Evidence . . . 10
  - 1.2.2 Dark Energy Evidence . . . 13
- 1.3 Problems of the ΛCDM Model . . . 15
  - 1.3.1 The fine tuning problem . . . 16
  - 1.3.2 The coincidence problem . . . 16
  - 1.3.3 The cusp-core problem . . . 18
  - 1.3.4 Other problems . . . 19

2 Elements of Density Perturbation Theory 21
- 2.1 Jeans Scale . . . 21
- 2.2 Linear Evolution . . . 22

3 The Cosmological Model 27
- 3.1 Quintessence . . . 27
- 3.2 Interacting Quintessence . . . 29
- 3.3 Multi coupled Dark Energy . . . 33
  - 3.3.1 Background evolution . . . 35
  - 3.3.2 Linear perturbations . . . 40
  - 3.3.3 Non-linear perturbations . . . 42

4 Statistical and Numerical Tecniques 53
- 4.1 Statistical Tools . . . 53
  - 4.1.1 Power Spectrum . . . 53
  - 4.1.2 Halo Mass Function . . . 55
  - 4.1.3 Radial Density Profile . . . 56
- 4.2 N-body simulations . . . 59
  - 4.2.1 Algorithms for N-body simulations . . . 60
  - 4.2.2 The GADGET code . . . 66

4.2.3 Initial Conditions . . . 68
4.2.4 Simulations of non-standard Cosmologies . . . 69
4.2.5 Zoomed Simulations . . . 72
4.3 Codes . . . 73

5 The ZInCo code 75
5.1 Producing the zoomed Initial Conditions . . . 75
5.2 Details of the code . . . 76
5.3 Testing the zoomed initial conditions . . . 82

6 The Simulations 87
6.1 Hardware . . . 89
6.1.1 PLX . . . 89
6.1.2 Hydra . . . 89
6.2 Diluted simulations . . . 89
6.3 Zoomed simulations . . . 91

7 Results 103
7.1 Early Segregation . . . 103
7.2 Radial Density Profiles . . . 110
7.2.1 Profiles in the uncoupled model . . . 110
7.2.2 Profiles in the coupled model . . . 114
7.2.3 Profiles at high redshift . . . 120
7.3 Halo Mass Function . . . 122

8 Conclusions 127
8.1 The ZInCo code . . . 127
8.2 Zoomed simulations of the McDE model . . . 128
8.3 Early Segregation . . . 128
8.4 Radial Density Profiles . . . 129
8.5 Problems and Perspectives . . . 130

Bibliography 133

A Details and Tests of the ZInCo code 137
A.1 Input parameters . . . 137
A.2 Benchmark Tests . . . 138

B The Leapfrog algorithm 145

C Details of the GADGET code 147
C.1 Performance . . . 147
C.2 Input . . . 148

Chapter 1

Introduction

From the middle of the last century, the existence of some new kind of matter has become progressively more and more clear. The first hint in the direction of the so-called "missing matter" is dated 1937, when the swiss astronomer Fritz Zwicky observed that, in order to explain the velocity of the galaxies in the Coma cluster, it has to contain much more matter than estimated from the luminous objects inside it[1].
At that time, the missing matter was believed to be ordinary (*i.e.* baryonic) matter, invisible some unknown reasons. The estimation of the cluster's mass in a non-gravitational way was based on the brightness of the cluster itself, so the hypothesis to explain the missing matter were all related to objects with small brightness, ranging from white and brown dwarf stars to black holes, from neutron stars to exoplanets, collectively called MACHOs (MAssive Compact Halo Objects).
As time passed, however, it became clear that the missing matter, called Dark Matter since it appears not to emit nor to absorb light, cannot be explained with baryonic matter. The main proof comes from the Cosmic Microwave Background (CMB) through the information it encodes about the history of the Universe as *e.g.* the evolution of cosmic structures.
Despite the proofs about the presence of the Dark Matter that are now robust, the problem of *what* the dark matter is remains an open problem for cosmology and for physics in general, both from an observational and a theoretical point of view.

In recent years, another cosmological problem appeared: observations about some particular type of supernovæ showed that the expansion of the Universe has started accelerating in the "recent" cosmological history. This is the problem of the Dark Energy, that remains unsolved at the present day.
The most natural, and most accepted, solution to this problem is the presence of some sort of cosmological constant, *i.e.* an additional term in the Einstein's equation which could be understood as a vacuum energy density (see Section 1.1 for details). However, every attempt to calculate the value of this constant as the vacuum energy predicted by quantum field theory failed, predicting a value that mismatches the observed one by about 120 orders of magnitude. Moreover, a similar cosmological constant requires a fine tuning

of the initial conditions in order to provide a cosmic evolution which is consistent with observational constraints.

The widely accepted theoretical framework concerning the dark components of the Universe is called ΛCDM model. Although it explains with good precision the observations about the content and the history of the Universe, it still suffers some problems, mainly the absence of a strong theoretical background for both the Dark Matter and the Dark Energy and the necessity of a fine tuning. A number of alternative theories for both the Dark Matter and the Dark Energy have been proposed, but they still suffer the same problems that plague the ΛCDM model.

1.1 The ΛCDM Model

1.1.1 From the Cosmological Principle to the Dark Sector problem

One of the main assumptions of the Standard Cosmological Model is the so-called *cosmological principle*, which states that:

> The Universe is homogeneous and isotropic at sufficiently large scales.

At present time, this principle starts to hold true at scales of hundreds of megaparsec[1], because at smaller scales the matter clustering (*e.g.* stars, galaxies, clusters of galaxies, ...) produces inhomogeneity and anisotropy.

The main proof supporting the cosmological principle comes from the Cosmic Microwave Background (CMB), a radiation that comes from every direction of the space and that corresponds to a black body radiation with temperature approximately 2.7 K. The CMB is a "picture" of how was the Universe 380,000 years after the Big Bang. The temperature fluctuations of the CMB, after taking into account all the effects that modify the original spectrum, are of the order of $\delta T/T \approx 10^{-5}$. This extremely low ratio shows that the Universe was, and now on sufficiently large scales is, isotropic. To prove the homogeneity of the Universe is more difficult and has not been done yet in a definitive way. However in some particular conditions it could be possible to determine the homogeneity with the CMB only[9].
Beside the difficulty of proving the cosmological principle, the latter is widely accepted as a useful and reliable approximation in modeling the Universe.

The cosmological principle above presented determines a specific form for the space-time metric $g_{\mu\nu}$. In particular it imposes the following constraints:

- $g_{00} = c^2$ to recover the correct null geodesic: $\frac{\mathrm{d}s^2}{\mathrm{d}t^2} = c^2$;

[1] The parsec (pc) is the fundamental unit of length in cosmology. It is defined as the distance from the Earth of a star that has an annual parallax of one arc second. It corresponds approximately to: 1 pc $\approx$ 3.26 light years $\approx 3.1 \cdot 10^{16}$ m.

- $g_{0j} = g_{i0} = 0$ to fulfil the isotropy requested by the cosmological principle (otherwise there would be different mixing of space and time for different directions);
- $dl^2 \equiv -g_{ij}\mathrm{d}x^i\mathrm{d}x^j = a(t)^2\left[\frac{\mathrm{d}r^2}{1-Kr^2} + r^2\mathrm{d}\Omega^2\right]$ with: $\mathrm{d}\Omega^2 = \mathrm{d}\theta^2 + \sin^2\theta\mathrm{d}\phi^2$ in order to take into account all the possible space geometries:
  - spherical, for $K = +1$;
  - planar, for $K = 0$;
  - hyperbolic, for $K = -1$.

The metric obtained by imposing these constraints is the so-called Friedmann-Lamaître-Robertson-Walker (FLRW) metric, that is:

$$\mathrm{d}s^2 = c^2\mathrm{d}t^2 - a(t)^2\left[\frac{\mathrm{d}r}{1-Kr^2} + r^2\mathrm{d}\Omega^2\right] \ , \tag{1.1}$$

where $a(t)$ is called the scale factor and represents how *space* evolves in time without changing its geometry, and K is called the curvature parameter.

A number of different measurements of the space curvature point toward a flat space (see *e.g.* [13] for the latest observational data). In this particular condition, the FLRW metric reduces to the usual Minkowski metric, given by:

$$\mathrm{d}s^2 = c^2\mathrm{d}t^2 - \delta_{ij}\mathrm{d}x^i\mathrm{d}x^j \ . \tag{1.2}$$

Using the cosmological principle, the FLRW metric, the field equations of General Relativity and the assumption that the content of the Universe behaves like a perfect fluid, we will come to the Friedmann equations, which describe the dynamics of the Universe as a whole.

The General Relativity field equation reads:

$$G_{\mu\nu} \equiv R_{\mu\nu} - \frac{1}{2}Rg_{\mu\nu} = 8\pi G T_{\mu\nu} \ , \tag{1.3}$$

where $R_{\mu\nu}$ is the Ricci tensor, $R \equiv R^{\mu}_{\ \mu}$ is the scalar curvature, G is the gravitational constant and $T_{\mu\nu}$ is the energy-momentum tensor. The Ricci tensor definition

$$R_{\mu\nu} \equiv \Gamma^{\lambda}_{\mu\nu,\lambda} - \Gamma^{\lambda}_{\mu\lambda,\nu} + \Gamma^{\lambda}_{\mu\nu}\Gamma^{\eta}_{\lambda\eta} - \Gamma^{\lambda}_{\mu\eta}\Gamma^{\eta}_{\lambda\nu} \tag{1.4}$$

is related to the Christoffel symbol:

$$\Gamma^{\lambda}_{\mu\nu} \equiv \frac{1}{2}g^{\lambda\alpha}\left(g_{\alpha\mu,\nu} + g_{\alpha\nu,\mu} - g_{\mu\nu,\alpha}\right) \ , \tag{1.5}$$

where a comma means a derivative with respect to the tensor index that follows (*i.e.* $\phi_{,\alpha} \equiv \mathrm{d}\phi/\mathrm{d}x^{\alpha}$). The scalar curvature is defined as the trace of the Ricci tensor.
For the FLRW metric, in unit of c=1[2], we obtain:

[2]The c=1 unit system (also called "natural system of units") will be used through this whole Thesis where not specified otherwise.

- $G^0_0 = -3\left(H^2 + \frac{K}{a^2}\right)$;
- $G^0_j = G^i_0 = 0$;
- $G^i_j = -\left(3H^2 + 2\dot{H} + \frac{K}{a^2}\right)\delta^i_j$;

where H is the Hubble's constant, defined as: $H \equiv \dot{a}/a$, and a dot denotes a derivative with respect to the cosmic time t.

The assumption of a perfect fluid gives a specific form of the energy-momentum tensor, that reads:

$$T^{\mu\nu} = -pg^{\mu\nu} + (p + \rho c^2)u^\mu u^\nu \ , \tag{1.6}$$

where p is the pressure of the fluid, ρ is its energy density and u^μ is the four-velocity of the fluid.
Moreover, a perfect fluid is characterized by a continuous velocity field with the property that for every reference frame comoving with a volume element dV the surrounding fluid is seen isotropic. In this comoving frame, the four-velocity is $u^\mu = (-1, 0, 0, 0)$.

The Einstein's equations (1.3) then become a tensor equation with the energy-momentum tensor (1.6), but only two independent components of this equation are non-trivial: the component (00) and the component (ii), which are:

$$\ddot{a} + \frac{4\pi}{3}G\left(\rho + 3p\right)a = 0 \ , \tag{1.7}$$

$$\dot{a}^2 + K = \frac{8\pi}{3}G\rho a^2 \ . \tag{1.8}$$

These are usually called Friedmann's equations. From the last one the curvature can be derived, *i.e.* :

$$\frac{K}{a^2} = H^2\left(\frac{\rho}{\rho_{crit}} - 1\right) \ , \tag{1.9}$$

where the critical density ρ_{crit} has been highlighted. This is the density value that correspond to an exactly flat space geometry. Comparing the above equation with the equation (1.8), the expression of ρ_{crit} can be derived:

$$\rho_{crit} = \frac{3H^2}{8\pi G} \ . \tag{1.10}$$

Note that both H and ρ_{crit} are functions of time, and so this relation specifies the critical density *at a given time* t. Moreover, the density of a generic component x of the cosmic fluid is expressed using the density parameter $\Omega_x \equiv \rho_x/\rho_{crit}$.
Furthermore, the two Friedmann's equations are related each other by the adiabaticity condition (that holds true since the Universe is a closed system):

$$\mathrm{d}U = -p\mathrm{d}V \ , \tag{1.11}$$

that in a cosmological context becomes:

$$\mathrm{d}(\rho a^3) = -p\mathrm{d}a^3 \ . \tag{1.12}$$

Using the Friedmann's equations it is possible to well explain the evolution of the Universe, provided the presence of some sort of "dark" components, which account for approximatively the 95% of the total matter-energy.
The problem of the so-called Dark Matter comes from several observations that point in the direction of a lack of baryonic matter, that is: there is (a lot) less baryonic matter than the quantity needed to explain the gravitational observations.
As explained above, the first hint came from observations of the velocities of the galaxies in the Coma cluster by the swiss astronomer Fritz Zwicky. As time passed, a lot of different proofs piled up. The problem of the Dark Matter can be summarized as follows: measurements of the curvature of the Universe give results compatible with a flat geometry, but measurements of the "standard" content of the Universe point toward a density far below the critical one.

Measurements of the curvature of the Universe

The main way to measure the spatial curvature of the Universe is by means of the CMB. The CMB anisotropies can be used as a standard ruler, *i.e.* a distance which does not depend on other quantities that characterize the Universe. This is due to the fact that these anisotropies, called Baryon Acoustic Oscillations (BAO), depend on the sound horizon at recombination, which is a well-know length scale and result in CMB overdensity spots that, for a flat Universe, should space each other by about 1 degree on average.
If the Universe has positive curvature (which means a closed Universe) the angles for a fixed distance will appear bigger than in the case of a flat Universe. On the contrary, for an open Universe the angles will appear smaller. So using standard rulers as *e.g.* the CMB anisotropies and measuring the angle under which they are seen, the curvature of the Universe can be determined.
Many experiments have done such measurements and the results are all compatible with a flat Universe. These experiments can be complemented by testing BAO not only at the recombination redshift but also for lower redshifts, where the BAO scale is measured by looking at the spatial distribution of the collapsed structures in our Universe. The results point once again toward a flat geometry of space[10].

Another way to test the curvature of the Universe involves a particular type of supernovæ denominated Ia. These are standard candles, *i.e.* their intrinsic luminosity can be determined without relying on some properties of the Universe, so measurements of their apparent brightness can be converted into a measure of their distance. Since the evolution of the Universe depends on the total density parameter of the Universe itself, at a fixed redshift the distance measurement can be used to determine the curvature. Also this method supports a flat geometry.

Measurements of the content of the Universe

The baryon matter content of the Universe ρ_b can be measured in different ways, the simplest of which is counting the visible matter in a given cosmic volume and extrapolate the total baryon density, relying on the cosmological principle that assures that for a sufficiently large region of the Universe, the local density is equal to the total density. A review of some different experiments of this kind can be found in [11].
Another way[12] of achieving the same result consists in studying the relative abundances of the light elements in the Universe, which are: hydrogen, deuterium, tritium, helium (both ^{3}He and ^{4}He) and lithium. Since their evolution is well-known through the theory of nucleosynthesis in the early Universe and depends on the baryon density, by comparing their observed densities with the predicted ones the baryon density can be constrained.

The radiation density of the Universe is easily computed from the CMB temperature, and results *nowadays* in a very small contribution to the mass-energy budget of the Universe.

The content of the Universe can be estimated also through the acoustic peaks of the CMB, called Baryonic Acoustic Oscillation, as described in section 1.2.

The latest measurement of the density parameters of the different components of the Universe comes from the ESA mission "PLANCK", and give the following scenario[13]:

- $\Omega_{baryon} \approx 0.05$,
- $\Omega_{radiation} \approx 10^{-5}$,
- $\Omega_{totalmatter} \approx 0.32$.

Dark Matter

The results presented above clearly show that the baryon matter alone is not sufficient in order to explain the total matter content of our Universe. Other evidence of this result comes from conceptually different experiments, *e.g.* gravitational lensing, galaxy rotation curves and velocity dispersions, Lyman-alpha absorption systems. A review of the proofs related to the presence of the dark matter can be found in [15], whilst a description of the main evidence supporting the Dark Matter can be found in Section 1.2.
These results also show that, since the total density of the Universe is very close to the critical density, the Dark Matter alone cannot explain, along with the baryons and the radiation, the whole energy content of the Universe.

There are many theoretical proposals that aim at explaining the presence of the Dark Matter, but none of them has yet been proved. The most remarkable candidates include *e.g.* neutralino (the supersymmetric partner of the neutrino), Kaluza-Klein particles and axions. Since it is not in the purpose of this Thesis to widely discuss the different theoretical proposal, the interested reader can found a review of the different Dark Matter

models and of their experimental evidence in [16].

The Dark Matter particle candidates can be divided into two groups, and this classification is important when the effects of the Dark Matter on the structures' growth are investigated. We define the derelativization time (t_{nX}) as the time when a particle (of Dark Matter for our purpose) X becomes non-relativistic, defined by:

$$A \cdot k_B T(t_{nX}) \approx m_X c^2 \ , \tag{1.13}$$

where A is a statistical factor that depends on the nature of the particle (*i.e.* a boson or a fermion) and is roughly approximated by a factor 3. Since the temperature T is a decreasing function of the time, heavy particles becomes non-relativistic before the lighter ones.
Furthermore, we define the decoupling time t_{DX} as the time when the particle X decouples from the rest of the "cosmological fluid" components. It is defined as:

$$\tau_{COLL}(t_{DX}) = \tau_H(t_{DX}) \ ,$$

where τ_{COLL} is the typical time for the reactions involving X particles and photons and τ_H is the typical time for the expansion of the Universe. Thus:

$$\frac{1}{n_X \sigma_X c} = \frac{1}{H} \ , \tag{1.14}$$

where n_X is the number density, σ_X is the cross section and c is the speed of light.
Comparing t_{nX} and t_{DX} for a fixed particle type, we can find three categories of particles:

- Hot Dark Matter: $t_{nX} >> t_{DX}$;
- Cold Dark Matter: $t_{nX} << t_{DX}$;
- Warm Dark Matter: $t_{nX} \approx t_{DX}$.

Although the previous claim about the lack of strong theoretical background for the Dark Matter is still true, some motivations concerning the presence of new types of matter comes from both supersymmetry and string theory. The former predicts the existence of a supersymmetric partners for every known particle with opposite statistics (*i.e.* fermion or boson); one or more of these particles not yet observed could provide a viable explanation of the missing matter. The latter provides a wide range of particles that could solve the problem of what the Dark Matter is. However, both of them lack of experimental testing and, moreover, present some problems in the description of the missing matter that must be overcome in order to produce an acceptable theory of the Dark Matter.

Dark Energy

About fifteen years ago (the first evidence of the Dark Energy is dated 1998[17, 18]), observations of type Ia supernovæ showed clearly that the Universe expansion has started

to accelerate in a cosmologically recent epoch. As time passed other proofs of the accelerating expansion came out, *e.g.* through the already mentioned BAO and the CMB power spectrum along with the lensing effects.

From the Friedmann's equation (1.7) it is easy to see that in order to have a positive acceleration $\ddot{a}$ the condition

$$\rho + 3p < 0 \tag{1.15}$$

must be fulfilled. For a generic perfect fluid we can define the equation of state:

$$p = w\rho \ , \tag{1.16}$$

where w is a parameter that depends on the fluid. For example, the radiation has $w = 1/3$, while non-relativistic matter has $w \approx 0$.
If we put this equation of state into equation (1.15), we obtain

$$w < -\frac{1}{3} \ , \tag{1.17}$$

which means that the fluid responsible of the acceleration must have a negative pressure, *i.e.* a repulsing, expanding force.
Since this condition cannot be fulfilled by matter (dark or not) or radiation, the existence of a new kind of energy, that has been called Dark Energy, must be assumed.

The theoretical framework for the Dark Energy is extremely poorly defined. The most reasonable way to explain the Dark Energy is the introduction of a cosmological constant, as we will see below, but the quantum field theory evaluation of its value overestimates the observed value of more than 120 orders of magnitude. Another well accepted theory, called Quintessence, explains the Dark Energy through an evolving scalar field in a self-interaction potential.

1.1.2 The Cosmological Standard Model

I now move to describe the most accepted model that describes the "dark components" of the Universe, the ΛCDM model, also known as the Standard Model of Cosmology, or Concordance Model.

For what concerns the Dark Matter, in this model it is considered:

- cold (see Section 1.1.1)
- dissipationless, *i.e.* it can not emit photons to cool down
- collisionless, *i.e.* : it interacts with other particles only through gravitational or weak interactions

Furthermore, the Dark Matter is thought to consist in only one type of particles, or at least to be composed in such a way that only one type of its particles is important in a cosmological context.

The Dark Energy in this model takes the form of a cosmological constant, *i.e.* a new term in the Einstein's equations (1.3), which now becomes

$$G_{\mu\nu} \equiv R_{\mu\nu} - \frac{1}{2} R g_{\mu\nu} + \Lambda g_{\mu\nu} = 8\pi G T_{\mu\nu} \ . \tag{1.18}$$

Written in this form, the cosmological constant appears as a modified form of the gravitational interaction[3]. The new term can also be moved to the right-hand-side of the above equation and considered as a new contribution to the (total) stress-energy tensor.
The cosmological constant represents a fluid with state parameter $w = -1$, which means that it does not dilutes as the Universe expands, *i.e.* its density remains constant.

The ΛCDM model needs at least six parameters to provide an useful and flexible model that can match the observations. In particular, these parameters are:

- the baryon density $\Omega_b h^2$,
- the Dark Matter density $\Omega_{DM} h^2$,
- the Dark Energy density Ω_Λ ,
- the scalar spectral index n ,
- the curvature fluctuation amplitude Δ^2_R ,
- the re-ionization optical depth τ ,

where h is a parameter that represents the Hubble constant in units of 100 $km/(s \cdot Mpc)$, *i.e.* :

$$H_0 = h \cdot 100 \ \frac{km/s}{Mpc} \ . \tag{1.19}$$

Additionally, some other quantities are fixed to their "natural" value, as *e.g.* the Dark Energy equation of state parameter $w_\Lambda = -1$ and the total density parameter $\Omega_{TOT} = 1$. Furthermore, the neutrinos are considered sufficiently light to discard the contribution due to their mass.

In the ΛCDM model the flatness of the Universe is explained through an initial phase of very rapid expansion of the space-time itself called inflation. In this way, every possible initial curvature of the space would have been stretched by orders of magnitude by the end of inflation, becoming practically indistinguishable from a flat geometry.

[3]This modified General Relativity equation was already proposed, and then retired and labelled as "the biggest blunder in my life" by Einstein himself, who was attempting to find a stationary solution for the Universe evolution, *i.e.* a solution with $\ddot{a} = \dot{a} = 0$.

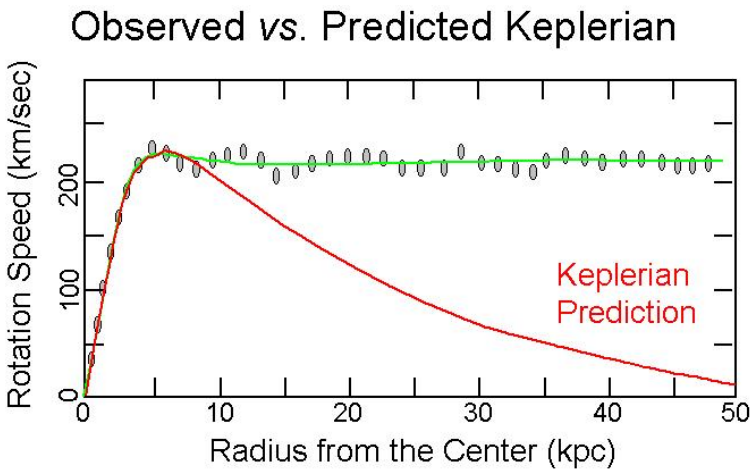

Figure 1.1: The radial velocity profile for a typical galaxy cluster (red curve), compared with the one predicted without the Dark Matter (green curve). This was the first evidence for the presence of the Dark Matter. The Figure is taken from www.astronomy.ohio-state.edu.

1.2 Observational Evidence

The ΛCDM model is supported by a wide range of evidence. In the following, the main proofs regarding the key aspects of the model are briefly reviewed.

1.2.1 Dark Matter Evidence

Historically, the first proof of the presence of Dark Matter was from the rotation curves of galaxies clusters. A computation of such curves can be made using the Newtonian gravity, which predicts a decreasing radial velocity following a square root behaviour: for a galaxy of mass m, orbiting at a distance r from the center of the halo, which has mass M, the equilibrium is given by:

$$G\frac{mM}{r^2} = m\frac{v^2}{r} \,, \tag{1.20}$$

which leads to

$$v(r) \propto r^{-1/2} \,. \tag{1.21}$$

On the other hand, the measurements of the latter quantity provide an almost flat profile for almost all the structures studied, meaning that the velocity of the galaxies is approximatively constant with the radius. This is clearly shown in Figure 1.1, while the first report of this kind of observation can be found in [89]. In the following years it became well-established that most of the galaxy clusters contain Dark Matter. Studying the velocity profile of the galaxies, the amount of matter and its distribution can be determined. It turned out that most of the clusters contain much more Dark Matter than ordinary matter. Moreover, the Dark Matter distribution does not follow the one of the baryonic

matter, but it is less clustered and thus covers a greater portion of space. This is the reason why its presence modifies the velocity profiles: since far from the center the Dark Matter has a grater density with respect to the baryonic component, its gravitational force provides an extra-attraction that accounts for the increased velocity of the outer galaxies.

A further proof of the existence of Dark Matter that comes from galaxy clusters is the direct measurement of the mass of the cluster. As an example, in [60] the analysis of the Coma cluster mass is performed. The contributions to the total mass of the cluster are mainly three: the mass due to the stars in the galaxies, the hot gas between the galaxies inside the cluster and the Dark Matter. The former can be estimated using photometric surveys, including corrections for the light from galaxies behind the ones observed and for the galaxies that are too faint to be detected. Then, the total luminosity estimated in this way is converted to the mass of the cluster's stars using a proxy relation $\langle L/M \rangle = const.$ The mass of the intracluster gas can be determined using its X-ray emission. The brightness profile can be used to reconstruct the amount of matter contained in the hot gas. The total mass of the cluster can be estimated using both optical and X-ray emissions, provided that some strong assumptions on the density profile, the temperature profile or the galaxy distribution are made. Both the methods used give consistent results.
Collecting together these results, a baryon density of $M_{baryon}/M_{tot} \approx 0.1$ is obtained, meaning that the greatest part of the cluster's mass is invisible. However, this procedure is affected by different sources of uncertainty, mainly the assumption that the intra-cluster plasma is in hydrostatic equilibrium within the gravitational potential.

A more direct detection relies on the gravitational lensing effect, which allows a direct measurement of the cluster's mass, without relying on additional assumptions. Although both the strong and the weak gravitational lensing[4] effects can be used in order to determine the properties (in the case of interest, the mass) of the lens, the former is highly model dependent and, additionally, can only provides information about the core of the cluster (see *e.g.* [61]). On the other hand, the latter provides a way to probe the mass of the halo in a model-independent way. As an example, in [62, 63, 64] the values of the gas-to-mass ratio found are bounded between $M_{gas}/M_{tot} = 0.04\ h^{-3/2}$ and $M_{gas}/M_{tot} = 0.07\ h^{-3/2}$, which clearly point out a strong problem of missing matter, which is solved by the ΛCDM model through the assumption of the existence of the Dark Matter.

One of the strongest evidences supporting the ΛCDM model is the existence of Cosmic Microwave Background, *i.e.* the light produced at the last scattering surface, about 480,000 years after the Big Bang, when photons and matter became decoupled. The global spectral shape (which is the one of a black body radiation) is modified by a number of different

[4]Strong gravitational lensing refers to situations where the lens is sufficiently massive and close to the source in order to produce a strongly distorted image (arc) of the source, or even multiple images. Weak gravitational lensing refers to situations where the lensing effect is weaker, thus the image of the source is only slightly distorted (both stretching or magnification of the source can occur).

effects, mainly due to

- gravity: when a photon is produced in a potential well it is subject to a redshift while it travels away; on the contrary, when it is produced in a peak it is subject to a blueshift.

- density: in adiabatic regime, an under-dense region is colder than the average, while an over-dense region is hotter; these different temperatures produce an effect opposite to the previous one.

- Doppler effect: the relative motion between the region where a photon is produced and the region of the observer produces a Doppler shift in the measured frequency of the photon.

Once the measured CMB has been corrected for the effects due to the velocity of our galaxy and from other sources of distortion, residual anisotropies of the order of $\delta T/\langle T\rangle \approx 10^{-5}$ are found. In a Universe without Dark Matter these anisotropies at $z_{CMB} \approx 10^3$ are not sufficient to explain the observed structures, because the baryon growth rate is proportional to the scale factor a and thus would have produced anisotropies of order 10^{-2} today. If the Dark Matter is present, it decouples from the radiation before the baryons (whose growth is frozen between the equivalence time and the decoupling time), and as a result, the growth rate is enhanced thanks to its additional gravity. This allows the Universe to enter in a phase of non-linear evolution, characterised by density fluctuation greater than the unity, and thus it explains the presence of structures, which are deeply-non-linear features.

Moreover, another important effect is related to the so-called Baryonic Acoustic Oscillations (BAO, hereafter). Since the CMB map obtained from the observations is a 2D map, its power spectrum can be decomposed in the Fourier space using the spherical harmonics

$$\delta T(\theta,\phi) = \sum_{l=0}^{\infty} \sum_{m=-l}^{l} a_{l,m} Y_m^l(\theta,\phi) \ , \tag{1.22}$$

where m is related to the direction of the signal while l is related to the angular separation between two points.
In the early Universe, the baryonic matter and the photons were tightly coupled. Both of them were subject to two opposite forces: the potential well due to the gravitational attraction of the overdensities and the pressure, opposite to the former. These forces produced density (acoustic) waves which travelled until the decoupling between baryons and photons occured. After that time, the photons started travelling freely producing the CMB, where the acoustic waves are frozen. The scale of the acoustic oscillation is related to the acoustic horizon, *i.e.* the maximum distance which can be covered by the acoustic waves, at the decoupling time.
Analysing the angular distribution of the CMB spectrum, the first peak corresponds to an acoustic oscillation which had just collapsed when the decoupling occur. For higher multipoles $l > l_H$, *i.e.* smaller distances in the CMB projection on the celestial sphere, other

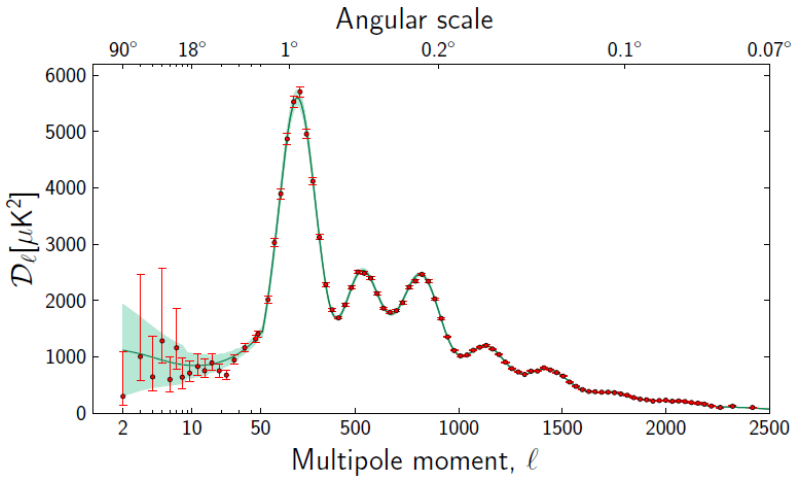

Figure 1.2: The temperature angular power spectrum data from WMAP, CBI and ACBAR compared with the ΛCDM prediction. Figure taken from [65].

peaks are found. They correspond to acoustic waves which underwent many compressions and consequent expansions due to the pressure. These effects combine producing a series of oscillations, as shown in Figure 1.2.

A detailed analysis of the formation of these peaks shows that: the position of the first peak can be trustfully estimated, thus it can be used as a standard ruler, *i.e.* an object with known dimensions, to compute the curvature of the Universe; the relative importance of odd and even peaks is related to the baryon loading, *i.e.* the amount of baryon at the decoupling time; the height of the peaks constrains the Dark Matter density.
Analysing the PLANCK mission data, the matter density is found to be about six times higher than the baryonic one, which points out that the largest fraction of the cosmic matter is non-baryonic.

1.2.2 Dark Energy Evidence

An early reason to introduce a cosmological constant is to reconcile a large Hubble constant (*e.g.* in [66] its value is obtained from the measurement of the velocities of distant galaxies through their surface brightness fluctuation and their distances) with the age of the Universe as determined studying globular clusters (*e.g.* in [67] the analysis of the relation between colours and magnitudes of the light emission of globular clusters is used to bound the possible age of the latter), since the presence of a cosmological constant would produce an accelerating expansion which would mimic a higher Hubble constant, *i.e.* if $\Lambda \neq 0$ the Universe appears older, for the same value of H_0, with respect to the case $\Lambda = 0$. Thus, the measured Hubble constant in the latter scenario would be higher (and the Universe age smaller) if a cosmological constant is present.

Moreover, the counting of faint galaxies is best fitted by a Universe with non-zero cosmological constant, as shown in [68], and the flat Universe predicted by the Inflation model can be achieved only assuming a cosmological constant density Ω_Λ greater than zero, given the amount of matter density discussed above.

As stated earlier, the strongest evidence of the existence of a cosmological constant arises from the observation of high-redshift supernovæ Ia, which are standardizable candles, meaning that starting from their luminosity curve, their highest intrinsic luminosity can be computed. This properties is due to the details of the star collapse that produces the supernova. The type named Ia is the result of a binary system composed by a white dwarf star[5] and another star (usually a red giant[6], but also sub-giant stars and rarely another white dwarf), in which the former steals matter from the other, increasing its mass. When the Chandrasekhar limit is reached, the pressure given by the electron degeneracy can no longer sustain the gravitational pressure and undergoes a collapse. The nuclear reactions that occur produce a fixed amount of ^{56}Ni (approximately 0.6-0.7 solar masses), and the luminosity curve of the supernova is determined by the decay chain of this isotope. Since the events involved in the production of the luminosity profile are all events with similar initial conditions, they all have very similar intrinsic luminosity.
Using the luminosity profile to determine the intrinsic luminosity (L) of the supernova, its distance can be computed through the relation

$$l = \frac{L}{4\pi d_L^2} \tag{1.23}$$

where l is the apparent luminosity and d_L the luminosity distance.
Hence, this type of supernovæ provides a reliable way to measure absolute distances at different times (*i.e.* different reshifts), and consequently to determine if there is an accelerated expansion of the Universe. These are the principles upon which [50] and [51] based their analyses that granted them the Nobel Prize in Physics in 2011. They showed that the apparent magnitude of these candles at a given redshift is fainter than what is expected in the case of a Universe containing only matter. Hence, in order to explain this discrepancy, an accelerated expansion of the Universe must occur.

Other ways of determine whetter the cosmological constant is vanishing or not are based on the gravitational lensing, as shown *e.g.* in [69], although not everyone agrees with the validity of this approach; and through the analysis of the CMB peaks, in particular the position and the height of the first peak are dependent on $\Omega_K h^2$ and $\Omega_b h^2$, respectively.

[5] The stars of this type are what remains of red giant stars that had no longer a sufficiently large mass to generate the pressure needed for sustaining the nuclear fusions in their core. The outer layers were shed and the exposed core is named white dwarf. Hence, these stars are composed in the majority of cases by oxygen and carbon, but sometimes also helium or neon can be present.

[6] The red giants are stars featuring large dimensions and high luminosity. They do not necessarily have a large mass, since their density could be significantly low.

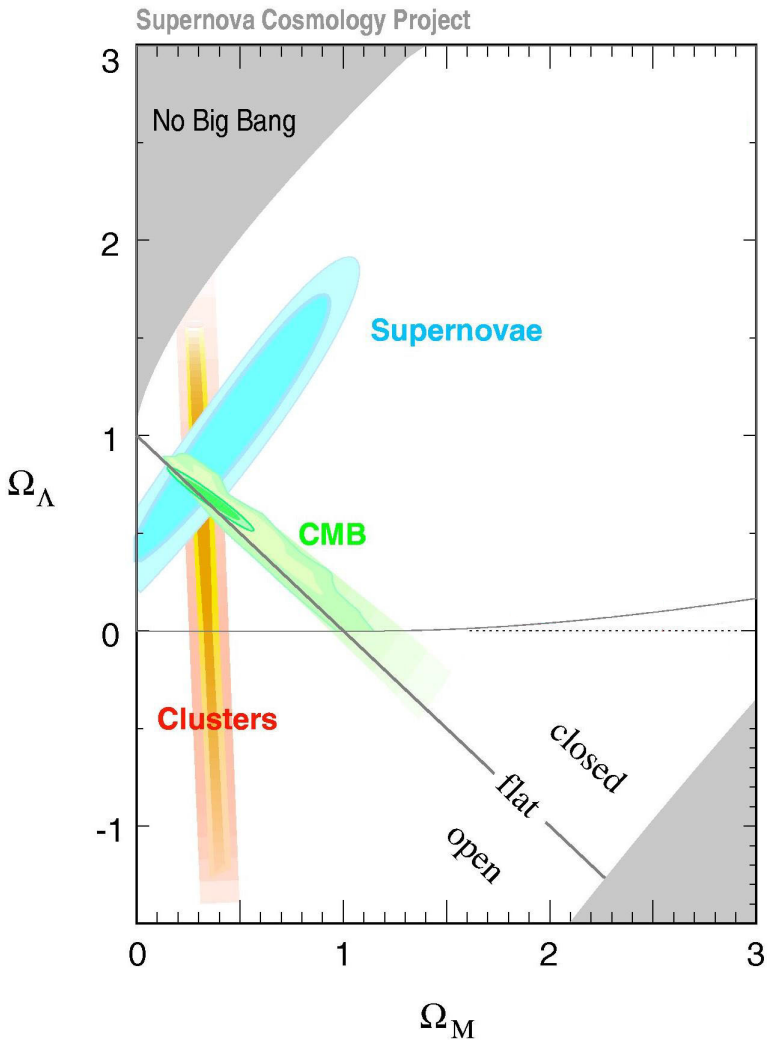

Figure 1.3: The combination of different constraints on the density parameters. This Figure is taken from http://www-supernova.lbl.gov/

In Figure 1.3 a number of independent constraints are reported. Their superposition tightly constrains the possible values of the density parameters.

1.3 Problems of the ΛCDM Model

The ΛCDM model well explains the majority of the observational data about the Universe, but as mentioned before, there are still observations that do not fully coincide with the model's predictions.

1.3.1 The fine tuning problem

The fine tuning problem refers to the previously stated mismatch between the observed value of the cosmological constant and the value computed using the Standard Model of Particle Physics.

The observed value of Λ can be computed in a number of different ways, some of which have been described in Section 1.2. The present measured value of the energy density due to the cosmological constant is

$$\rho_\Lambda \approx 10^{-6}(GeV/c^2)cm^{-3} \ . \tag{1.24}$$

On the other hand, from the point of view of the Particle Physics, we can consider the cosmological constant as a vaccum energy. As an example, let us consider a real scalar field, with zero-point energy given by:

$$cU_0 \equiv V \int \frac{\mathrm{d}\vec{k}}{(2\pi)^3} \frac{1}{2} \hbar \omega_{\vec{k}} \ , \tag{1.25}$$

and turning to the energy density:

$$\langle \rho \rangle_{QFT} = \frac{\hbar}{4\pi c} \int_0^K k^2 \mathrm{d}k \sqrt{k^2 + \frac{m^2 c^2}{\hbar^2}} \ , \tag{1.26}$$

where K is the maximum value of the momentum at which the theory is considered reliable. This is related to the Planck mass[7] $M_P = 10^{19} GeV/c^2$. Thus, setting $K = cM_P/\hbar$ and taking into account that $\hbar K >> mc$ the zero-point energy density becomes

$$\langle \rho \rangle_{QFT} \approx \frac{K^4 \hbar}{16\pi^2 c} \approx 10^{115}(GeV/c^2)cm^{-3} \ . \tag{1.27}$$

1.3.2 The coincidence problem

Another critical problem of the ΛCDM model is related to the need of a fine tuning of the parameters in order to get an evolution of the Universe that is compatible with the present observed Universe. In particular, the value of the cosmological constant must be precisely chosen, otherwise the properties of the Universe would be extremely different from the observed ones. If the value of Λ was slightly smaller, then we would not observe a Λ-dominated era, because at the present time the Universe would be still matter-dominated. On the other hand, if its value was slightly higher, the acceleration of the expansion would be strong enough to prevent the structure formation, because the matter particles would

[7] The Planck mass is the mass scale where the effects of general relativity and quantum mechanics are expected to be both non-negligible. It is also the mass unit in the natural unit system.

be driven away one from the other before they had the possibility to bound together to form structures.
This is obviously in contrast with the widely-accepted idea that a theory which aims at explaining the Universe properties must not rely on the presence of an unlikely situation (*i.e.* parameters values, initial conditions, ...). It is not in the purpose of this Thesis to discuss the validity of this approach, but it must be said that a number of physicists argued that our own existence is a strong evidence supporting the anthropic principle, at least in its weak formulation [49].
Thus, unless accepting that our Universe is "specially suited for life", it would be desirable to have a wide range of initial conditions that determine an evolution of the Universe consistent with the observed situation.
The problem described above is dubbed "coincidence problem" and arises from the observation that in the present Universe the energy density of matter and cosmological constant are comparable. However, this is not the most likely scenario, because it happens only for a short period of time, namely when the matter density (which decreases with the expansion of the Universe) is overcome by the cosmological constant density (which remains constant). This is clearly shown in Figure 1.4.

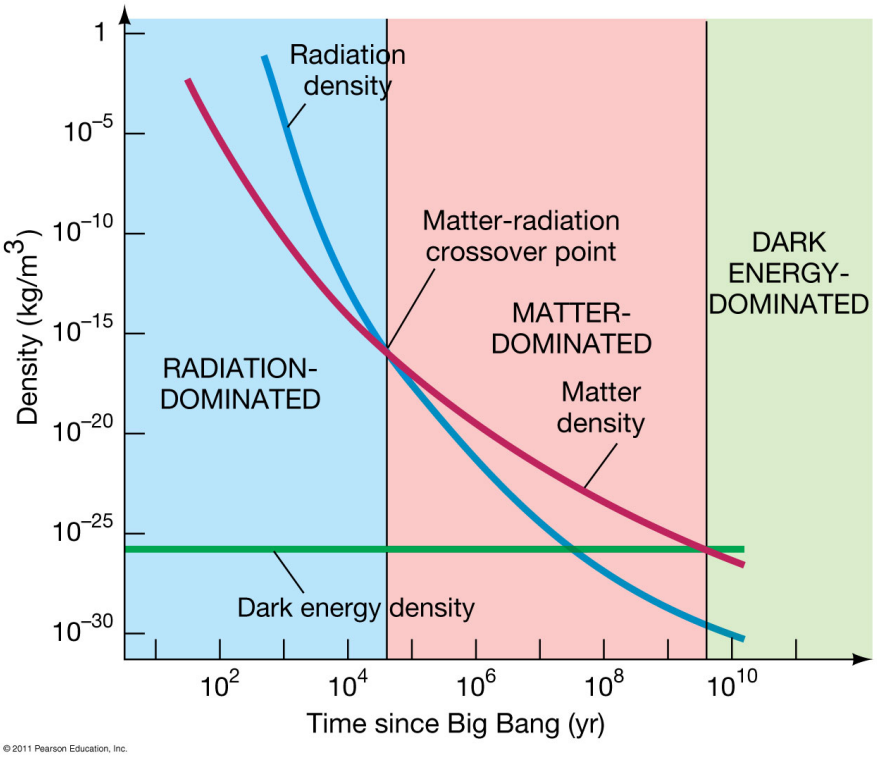

Figure 1.4: Evolution of the densities of matter, radiation and cosmological constant as functions of time. This Figure is taken from http://pages.uoregon.edu.

1.3.3 The cusp-core problem

A further problem arises from the numerical simulations of the evolution of the Universe. These simulations showed that the Cold Dark Matter clusters in halos with a cuspy density profile, *i.e.* halos with a density profile steeply increasing toward the center.
In particular, the density profiles computed from the numerical simulations follow a power law in the inner part of the halo

$$\rho \propto r^{-\alpha} \tag{1.28}$$

with the slope α in good agreement with the value $\alpha = 1$.
As an example, one of the first set of simulations is described in [52], where the $\alpha = 1$ slope was found. In that paper the resolution was not enough high in order to rule out the presence of a core with constant density. However, the development of numerical techniques improved the resolution of the simulations and now it is safe to say that the presence of such a core does not appear in numerical simulations of the ΛCDM model.
Although the presence of cuspy profiles seems to be confirmed by the large amount of simulations performed, its detailed shape is still under discussion. In particular, the value of the slope α is found to be different by different authors: in [54] a value of $\alpha = 1.5$ is found, while in [55] a value of $\alpha = 0.75$ is determined. Also, a number of values between these two boundaries have been found. Furthermore, some authors (like in [56]) proposed that this inner density could not follow a simple power law, keeping getting shallower as the radius decreases.
Moving to the outer profile, the shape is well approximated by a power law with slope $\alpha = 3$.
A more detailed discussion of the density profiles shapes and fitting formulas is postponed to Section 4.1.3.

On the other hand, the observations of the inner density of a significant number of galaxies yield a value $\alpha \approx 0$. Some of the earliest measurements of the density profiles were based on the rotation curves of dwarf-galaxies (see *e.g.* [57]), since their dynamic is mainly governed by the Dark Matter. These studies showed that the observed profile is better described by a core model with constant central density when compared to the predictions of the ΛCDM-based numerical simulations.
A further way to study the Dark Matter distribution is through the HI signal[8]. In [58] the first observations using this line are compared to the predictions of ΛCDM simulations and show that the numerically-predicted profile is too steep to satisfactorily match the observed profiles.
Further on, also the Hα line has been widely studied, in order to increase the resolution level. The results (see *e.g.* [59]) are consistent with the ones obtained using the HI line, and in some cases are even more flat toward the center, increasing the tension between

[8]The light emission of the Hydrogen atoms due to the transition from parallel to anti-parallel spins for the proton and the electron that form the atom. This transition has an extremely slow rate, resulting in a very narrow spectral line at 21.106 cm.

the observations and the numerical predictions.

A review of both the simulations performed and the observations made upon this topic can be found in [53].

1.3.4 Other problems

Some examples of other failures of the ΛCDM model can be found *e.g.* in [19], where is obtained a value of the Hubble parameter that differs from the previous estimation of the same parameter, and in [20, 21] where a significantly lower-than-predicted Sunyaev-Zel'dovich effect has been found. The Sunyaev-Zel'dovich (SZ) effect consists in the gain of energy by the CMB photons when they pass through the hot gas regions of the galaxy clusters, due to their interactions with the free electrons via inverse Compton scattering. As a result, the CMB spectrum is distorted since these electrons gain energy and are shifted to higher frequencies. There are also results[22, 23] opposite to the ones presented above, *i.e.* in agreement with the ΛCDM model.
Other deviations from the ΛCDM model come once again from the large amount of numerical simulations made. In these simulations, the number of galaxies in the voids of the cosmic web is larger than the number of observed galaxies.
Both these problems could be due to the numerical implementation, but the simulations have reached such a high level of resolution, number of particles involved and completeness in taking into account the physical effects that it is not unreasonable to identify these problems as problems of the ΛCDM model itself.

Finally, one of the main problems of the ΛCDM model is the astonishing lack of experimental detection of the Dark Matter particles. After more than half a century from the theorization of the Dark Matter as non-baryonic particles, no experiment managed to detect these particles.

Chapter 2

Elements of Density Perturbation Theory

The ΛCDM model is suitable to describe the main feature of the Universe, but in order to describe the structure formation a number of further effects must be taken into account. In particular, it can be described analytically only at a background level, *i.e.* for an homogeneous cosmological fluid, or linearizing the perturbations, *i.e.* disregarding the higher order perturbation to the homogeneous background.
In the present Chapter, some basic concepts regarding the background and linear perturbations evolution are presented, in order to allowa better understanding of the feature presented in Chapter 3.

2.1 Jeans Scale

In order to take into account the current presence of structures in the Universe, such as galaxies and galaxy clusters, the cosmological fluid cannot be thought as perfectly homogeneous. Some inhomogeneities must have been present right after the Big Bang, in such a way that the denser regions have began to attract the surrounding fluid stronger than the other regions and have led to the growth of the first proto-structures. They are often referred as "the seeds" of the current structures.
The fundamental quantity in the study of the growth of structures is the density contrast, *i.e.*

$$\delta(x) \equiv \frac{\rho(x) - \bar{\rho}}{\bar{\rho}} \ , \tag{2.1}$$

where $\bar{\rho}$ is the mean value of the density. The positivity of the energy constrains the possible values of the density contrast to $\delta > -1$.

The forces acting upon the cosmological fluid are gravity, which attracts the particles towards each other, and pressure, due to the micro-physics (*i.e.* the non-gravitational forces) and thus acting on scales smaller than the former, which has the opposite effect, *i.e.* it tends to avoid the particles' collapse. So, it exists a scale where this two opposite

forces almost balance each other. This is called Jeans scale, and it can be computed in some different ways, *e.g.* comparing the energies related to the opposite acting forces: the gravitational potential energy of a perturbation of mass M and length R, *i.e.*

$$E_P = G\frac{M^2}{R} \ , \tag{2.2}$$

and the kinetic energy of the same perturbation, with mean velocity v, *i.e.*

$$E_K = \frac{1}{2}Mv^2 \ . \tag{2.3}$$

The Jeans scale is defined as the scale where $E_P \approx E_K$, *i.e.* :

$$R_J \propto \frac{v}{\sqrt{G}} \ . \tag{2.4}$$

The constant factor that multiplies the right-hand-side of the above equation has been discarded in order to write a more general equation, since this constant factor changes for different ways used to compute the Jeans scale, but the characteristic form of (2.4) is common to all the derivations and it is the signature of R_J.
The existence of this scale means that not all the overdense regions collapse into a structure, but only the ones that are bigger than the Jeans scale.

A related quantity is the Jeans' mass, *i.e.* the mass contained in a sphere of radius equal to the Jeans' scale

$$M_J \propto \rho_m \lambda_J^3 \ , \tag{2.5}$$

where ρ_m is the total matter density. In this definition only the matter density is considered since it is used in the study of matter perturbations. The Jeans' mass represents the threshold mass above which the perturbations start collapsing and, therefore, growing. On the contrary, below this mass the matter perturbations cannot grow.

2.2 Linear Evolution

In order to determine the Jeans scale in a more precise way, a Newtonian approach can be used to study the evolution of the perturbations, as made in the original paper [24]. The variables of the problem are: the density ρ of the cosmological fluid, the velocity of its particles $\vec{v}$, the gravitational potential ϕ, the pressure p and the entropy S. The equations that determine how the system evolves are the continuity equation:

$$\frac{\partial \rho}{\partial t} + \vec{\nabla} \cdot (\rho \vec{v}) = 0 \ , \tag{2.6}$$

the Euler's equation for a perfect fluid:

$$\frac{\partial \vec{v}}{\partial t} + (\vec{v} \cdot \vec{\nabla})\vec{v} = -\frac{1}{\rho}\vec{\nabla} p - \vec{\nabla}\phi \ , \tag{2.7}$$

the Poisson's equation:

$$\nabla^2\phi = 4\pi G\rho \ , \tag{2.8}$$

the equation of state of the cosmological fluid:

$$p = p(\rho, S) \ , \tag{2.9}$$

and the entropy change rate:

$$\frac{\mathrm{d}S}{\mathrm{d}t} = f(t) \ . \tag{2.10}$$

Following the original work by Jeans, I assume a background homogeneous solution modified by small adiabatic perturbations. The first is provided by constant values of the problem variables[1]

$$\begin{cases} \rho = \rho_{bg} \\ p = p_{bg} \\ \vec{v} = 0 \\ \phi = \phi_{bg} \end{cases} \tag{2.11}$$

while the perturbation is given by

$$\begin{cases} \rho = \rho_{bg} + \delta\rho = \rho_{bg}(1+\delta) \\ p = p_{bg} + \delta p \\ \vec{v} = \delta\vec{v} \\ \phi = \phi_{bg} + \delta\phi \end{cases} \tag{2.12}$$

where δ is the one defined in equation (2.1). The smallness condition for the perturbation is provided by:

$$\frac{\delta x}{x} << 1 \qquad \text{for } x = \rho,\ p,\ \vec{v},\ \phi \ . \tag{2.13}$$

Furthermore, the perturbations are assumed to be plain waves:

$$\delta x(\vec{r}, t) = \delta x_k \exp\{i\vec{k}\cdot\vec{r} + i\omega t\} \qquad \text{for } x = \rho,\ p,\ \vec{v},\ \phi \ . \tag{2.14}$$

Once inserted in equations 2.6-2.8, three relations between the perturbation amplitudes can be obtained. The existence of a solution for the system of equations is granted imposing the vanishing of the system determinant. It provides the dispersion relation $\omega = \omega(k)$, which allows to compute the Jeans wavelength, *i.e.* the Jeans scale:

$$\lambda_J = v_s\sqrt{\frac{\pi}{G\rho_{bg}}} \ , \tag{2.15}$$

[1]Note that this cannot be a real background solution, because it doesn't satisfy Poisson's equation, but here we use it in order to follow the original paper, since the results are not affected, due to the fact that when the Universe expansion is introduced, this turns out to *be* an acceptable background solution.

where v_s is the sound speed in the perturbation mean (*i.e.* in the cosmological fluid).

In order to properly take into account the expansion of the Universe, we define the comoving coordinates x through the relation

$$r \equiv ax \ , \tag{2.16}$$

where r are the proper coordinates. In the comoving coordinates the expanding particles remain at a fixed position in the comoving reference frame.
The physical laws written in the form of (2.6)-(2.8) hold true only in the usual coordinates, while in the comoving framework have to be modified. Taking into account the equation (2.16), the perturbation definition (2.12) and splitting the velocity $\vec{v}$ into its components parallel and perpendicular with respect to $\vec{k}$, the fundamental equation for the evolution of the density perturbations reads[2]:

$$\ddot{\delta_k} + 2H\dot{\delta_k} + \delta_k \left(\frac{k^2 v_s^2}{a^2} - 4\pi G \rho_{bg} \right) = 0 \ , \tag{2.17}$$

where $\delta_k = \delta(k)$ is the generic Fourier space component of $\delta(\vec{x})$.
Note that to obtain the above equation the condition of smallness has been used to discard all the contributions beyond the first order in the perturbations. For this reason this is the *linear* perturbation equation. Taking into account higher orders would lead to much more complications that make the equations not analytically solvable. For this reason the numerical simulations play a fundamental role in the study of the non-linear regime of the perturbations evolution.

Turning back to the proper coordinates, we have

$$k_{proper} = \frac{k_{comoving}}{a} \tag{2.18}$$

and thus, the first term in the parenthesis in equation (2.17) becomes $k^2 v_s^2$.

An equation similar to equation (2.17) holds true for all the components of the cosmological fluid, *i.e.* baryons (b), radiation (r), Dark Matter (DM) and Dark Energy (DE). However, these equations differ from equation (2.17) because the last term in the parenthesis needs to be modified in order to take into account the fact that all the components are sources of the gravity potential. The equation for a generic component i (i =b, r, DM, DE) is:

$$\ddot{\delta}_{k,i} + 2H\dot{\delta}_{k,i} + \delta_{k,i} k^2 v_s^2 - 4\pi G \sum_j \left(\delta_{k,j} \rho_{b,j} \right) = 0 \ . \tag{2.19}$$

At different epochs in the evolution of the Universe, one or more of the components can be ignored because their density is negligible when compared to the other components.

[2]For a more detailed discussion, see *e.g.* [25].

This obviously modifies the solution to equation 2.19.
In Table 2.1 are reported the different behaviours of δ_k for the different components of the cosmological fluid, at different scales and times, obtained solving equation 2.19 with the appropriate approximations.

scale \ *time*	0	t_{eq}	t_{dec}
$\lambda > R_H$	$\delta_r \propto \delta_{DM} \propto \delta_b \propto a^2$	$\delta_r \propto \delta_{DM} \propto \delta_b \propto a$	
$\lambda_J < \lambda < R_H$	$\delta_r \propto \delta_b \approx$ oscill $\delta_{DM} \approx const.$	$\delta_r \propto \delta_b \approx$ oscill $\delta_{DM} \propto a$	$\delta_r \approx$ oscill $\delta_b \propto \delta_{DM}\left(1 - \frac{a_{dec}}{a}\right)$ $\delta_{DM} \propto a$

Table 2.1: Perturbations growth for the different components of the cosmological fluid at different scales and epochs. R_H is the horizon radius, *i.e.* the scale length above which the gravity is the only acting force.

Chapter 3

The Cosmological Model

The Specific model studied in this Thesis through numerical simulations is described in Section 3.3. However, it is a particular example of a wider class of models, whose roots can be identified in the Quintessence model, described in Section 3.1 and in its generalization (the Coupled Quintessence) presented in Section 3.2.

3.1 Quintessence

The evidence of an accelerating expansion of the Universe (a sample of them were presented in Section 1.2) led to ascribe this effect to a cosmological term in the Einstein equations. However, there are many reasons that make this solution unappealing: above all, the inconsistency between the theoretically computed value and the observed one.
Moving to a slightly more complex model, the accelerating expansion could be addressed as an effect of a real scalar field ϕ, named "Quintessence", first proposed in [43] and [44]. This field is supposed to evolve under a potential $V(\phi)$ and to be sufficiently flat to mimic a cosmological constant, *i.e.* its inhomogeneous part can be neglected. Hence, its equations of motion can be determined minimizing the action

$$S[\phi] = \int dx^4 \sqrt{-g}\mathcal{L} = \int dx^4 a^3 \left(\frac{1}{2}\nabla^\mu \phi \nabla_\mu \phi - V(\phi) \right) \ , \tag{3.1}$$

where $g = \det(g_{\mu\nu})$ with $g_{\mu\nu}$ being the FLRW metric 1.1 in the case of a flat Universe ($K = 0$). The Euler-Lagrange equation of motion reads

$$\ddot{\phi} + 3H\dot{\phi} + \frac{\partial V(\phi)}{\partial \phi} = 0 \ , \tag{3.2}$$

and the stress-energy tensor is

$$T_{\mu\nu} = \nabla_\mu \phi \nabla_\nu \phi - g_{\mu\nu}\mathcal{L} \ , \tag{3.3}$$

which leads to the expressions for the energy density and the pressure:

$$\rho_\phi = T_{00} = \frac{1}{2}\dot{\phi} + V(\phi) \ , \tag{3.4}$$

$$p_\phi = -\frac{1}{3}T_i^i = \frac{1}{2}\dot{\phi} - V(\phi) \ . \tag{3.5}$$

The latter shows that it is possible to have negative pressure if $\dot{\phi}$ is sufficiently small, leading to a negative parameter w in the equation of state of the Dark Matter fluid:

$$p = w\rho \ . \tag{3.6}$$

However, the positiveness of energy constrains this parameter to values $w \geq -1$.

It must be said that there are different shapes of the potential $V(Q)$ which fit the observational constraints after a suitable choice of the parameters, the simplest of which is the one describing a massive non-self-interacting field, *i.e.*

$$V(Q) = \frac{1}{2}m_Q Q^2 \ . \tag{3.7}$$

The particle associated with this scalar field Q is called "cosmon" and its mass would be of the order of $10^{-33}eV$. This would also explain why it has not been observed yet: its very small mass would be covered and hence hidden by the noise.

Some Quintessence models could solve the fine-tuning problem discussed in Section 1.3 thanks to the presence of the so-called tracking solutions, *i.e.* solutions which are substantially independent from the initial conditions. An example of such models are the ones characterized by potentials taking the form

$$V(Q) = M^4 \left(\exp\left\{\alpha M_{PL}/Q\right\} - 1\right) \tag{3.8}$$

or

$$V(Q) = M^{4+\alpha}/Q^\alpha \ , \tag{3.9}$$

with M and α being positive parameters and $M_{PL} \approx 1.22 \cdot 10^{19}\ Gev/c^2 \approx 22 \cdot 10^{-6} g$ being the Planck mass. Potentials of these types could easily originate from particle physics and string theory (see *e.g.* [29] or [30]).
These solutions allow the initial density of the Quintessence field ρ_Q to vary by more than 100 orders of magnitude without significantly changing the final state of the cosmon field. Nevertheless, the coincidence problem is not completely solved.

The parameter w for the tracker models behaves differently in the different phases of the cosmic evolution. The most important feature is the fact that the density ρ_Q grows faster than the matter density, thus eventually surpassing the latter, providing the beginning of a Q-dominated era which mimics a Λ-dominated one when $\Omega_Q \to 1$. The measurements which provide $\Omega_m > 0.2$ constrain the w parameter to be $w \geq -0.8$ [45].

An alternative approach in the framework of Quintessence is the so-called "k-essence", where the potential $V(Q)$ is discarded and replaced by a function $F(X, Q)$ which depends

on the cosmon field and its kinetic energy

$$X = \frac{1}{2}\partial_\mu Q \partial^\mu Q = \frac{1}{2}\dot{Q}^2 \tag{3.10}$$

where the last equivalence is due to the spatial homogeneity of Q.
This "k-essence" could, depending of the choice of $F(X, Q)$, exhibit a tracking behaviour in the radiation-dominated epoch and then switch to a behaviour that mimics the effects of a cosmological constant in the matter-dominated epoch. Consequently, the coincidence problem is explained since we can live only during the matter-dominated era, and so it is natural that the dark energy domination began close to the present time.
Furthermore, there are also models with $w < -1$, named "phantom energy". Since they predict all the bounded structures to be ripped apart, the coincidence problem is avoided since the only possible period for our evolution is the period between the beginning of the matter-dominated epoch and the ripping of the bounded structures. However, such models can have strange implications, like traversable wormholes, negative temperature and closed time-like geodesis, all of them as a consequence of the non-positiveness of energy.

Observational constraints for the Quintessence model comes from *e.g.* the nucleosynthesis, which requires the energy density due to the scalar field to be small enough to not perturb the productions of elements in the early Universe. In particular, it requires:

$$\Omega_\phi(t_n s) < 0.1 - 0.2 \ . \tag{3.11}$$

3.2 Interacting Quintessence

A step toward the generalization of the Quintessence model is to allow interactions between the scalar field ϕ and the dark matter through the mass term, which is now ϕ-dependent. The Lagrangian density of such a model is given, for fermion Dark Matter particles χ, by:

$$\mathcal{L} = \frac{1}{2}\partial_\mu Q \partial^\mu Q - V(Q) + m(\phi)\bar{\chi}\chi + \mathcal{L}_{kin}[\chi, \bar{\chi}] \ . \tag{3.12}$$

The dependence of the mass on the field means that, in general, this mass is time-dependent.
One of the most famous examples of such model can be found in [48], where a Yukawa coupling for the dark sector is considered. In such a model the mass term is given by

$$m(\phi) = y(\phi_* - \phi) \ , \tag{3.13}$$

where y is the Yukawa coupling constant and ϕ_* is a constant mass term ascribable only to the χ particle, *i.e.* interaction-independent.

Also, it is possible to consider a coupling that, although conserving the total stress-energy tensor, provides

$$\begin{aligned} T^{\mu\nu}_{(\phi);\mu} &= \ \ CT^{\mu\nu}_{(m)}\phi_{;\mu} \ , \\ T^{\mu\nu}_{(m);\mu} &= -CT^{\mu\nu}_{(m)}\phi_{;\mu} \ , \end{aligned} \tag{3.14}$$

where the subscripts (ϕ) and (m) label the stress-energy tensor part related to the scalar field and to the other matter (*i.e.* baryons plus CDM) respectively. However, constraints coming from observational tests, such as *e.g.* [47], rule out the possibility of a universal coupling between the scalar field and matter. Thus, an interesting possibility is to hypothesise different couplings to the different components of the cosmological fluid. In particular, if the coupling to the ordinary matter is vanishing while the coupling within the Dark Sector is non-vanishing, then the tests that rule out a fifth force as strong as gravity can not be taken into account since they are based on baryon interaction (see *e.g.* [70, 71]). In the latter case, the constraints on the possible values of C become [72]

$$|C| < 5M_{PL}^{-1} \ . \tag{3.15}$$

More complicated and non-linear couplings are also possible.
It is important to note that the constraint above applies only to constant couplings, and can be easily escaped by a time-dependent coupling.

The equations of motion for the latter model read

$$\ddot{\phi} + 3H\dot{\phi} + a^2\frac{\mathrm{d}V(\phi)}{\mathrm{d}\phi} = C\rho_m a^2 \ , \quad \dot{\rho_m} + 3H\rho_m = -C\rho_m\dot{\phi} \ , \dot{\rho_\gamma} + 4H\rho_\gamma = 0 \ , \tag{3.16}$$

for the scalar field, total matter and radiation, respectively.

The equation of motion

$$H^2 = \frac{8\pi}{3M_{PL}^2}\rho_{TOT}(a) \tag{3.17}$$

can be solved introducing the following variables:

$$x = \sqrt{\frac{4\pi}{3}}\frac{\dot{\phi}}{M_{PL}H}, \ y = \sqrt{\frac{8\pi}{3}}\frac{\sqrt{V}}{M_{PL}H}, \ z = \sqrt{\frac{8\pi}{3}}\frac{\rho_\gamma}{M_{PL}H} \ . \tag{3.18}$$

It turns out [46] that the model admits only two solutions (depending on the choice of its parameters' values) which provide an accelerated expansion, *i.e.* $w \in [-1, -0.4]$ as requested by observations.
One of them features a constant value of Ω_m and Ω_ϕ. Although this completely solves the coincidence problem, it requires a large value of the coupling, and thus a fifth interaction much stronger than gravity, in order to match the observed w parameter. Moreover, it lacks of a matter-dominated era, as clearly shown in Figure 3.1. This last feature has two main consequences: the radiation dominates until recent times (redshifts of order 50) and the structure growth is strongly suppressed, leading to a σ_8 parameter much smaller than the observed one, as small as 10^{-4}.
The other solution provides the existence of a period of time in which Ω_ϕ is constant and non-vanishing, called field-matter-dominated-era (ϕMDE), which is responsible for the main differences with respect to the uncoupled quintessence (see Section 3.1) and, moreover, is a typical feature of the coupled model. In Figure 3.2 is reported the evolution

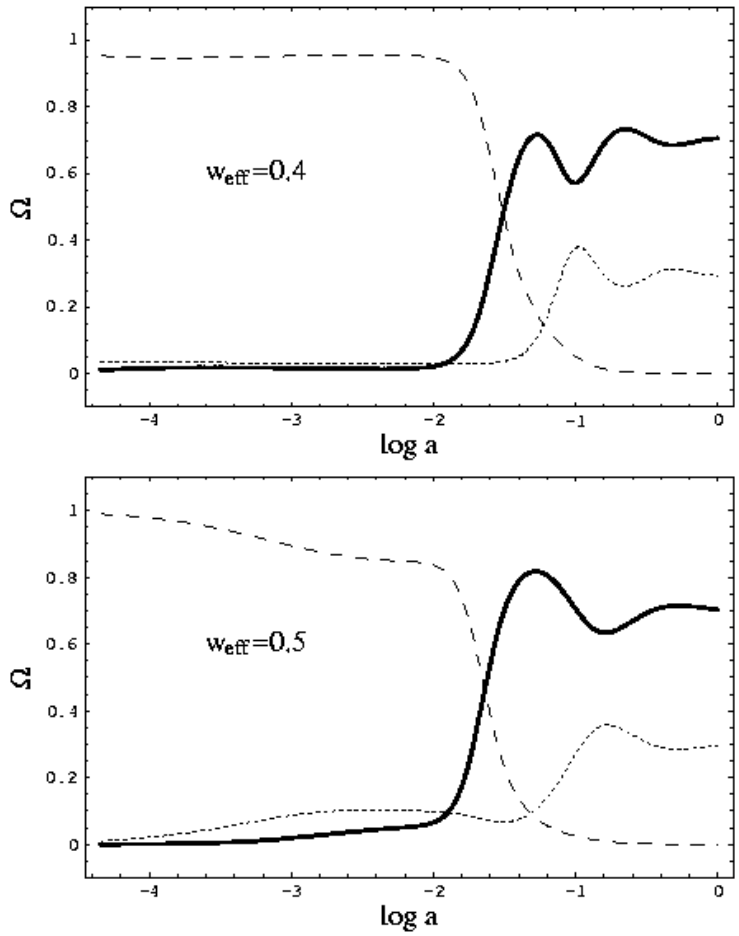

Figure 3.1: The evolution of the density parameters (Ω_m: dotted line, Ω_γ: dashed line, Ω_ϕ: thick line) for two different coupled quintessence model. The Figure is taken from [46].

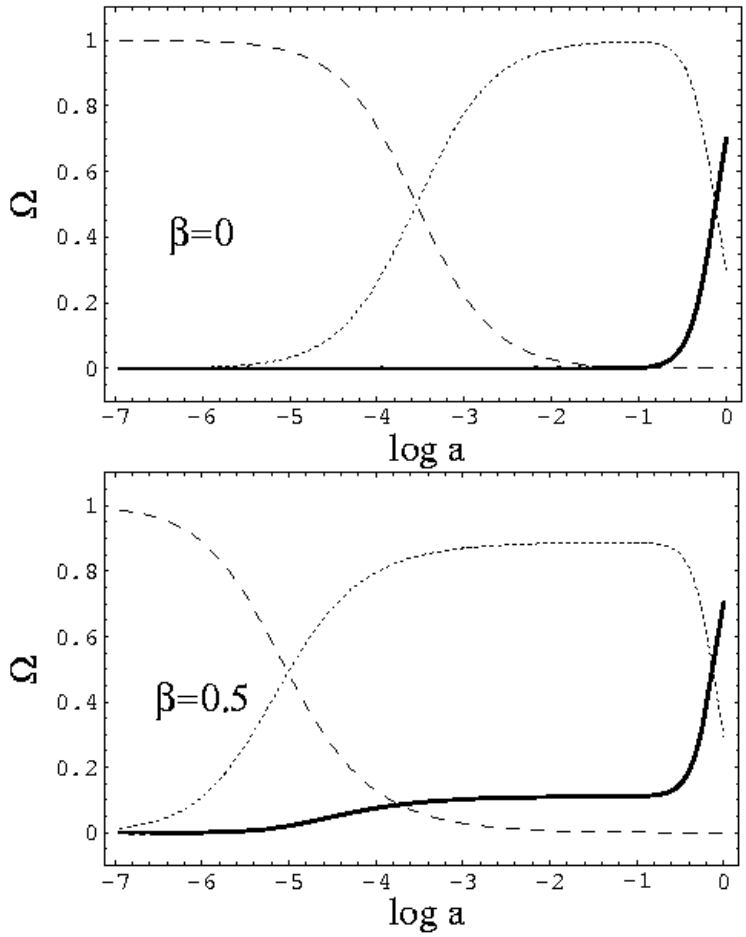

Figure 3.2: The evolution of the density parameters (Ω_m: dotted line, Ω_γ: dashed line, Ω_ϕ: thick line) for the uncoupled ($\beta = 0$) and a coupled ($\beta = 0.5$) quintessence model. The Figure is taken from [46].

of the density parameters as a function of log(a): in the case of a non-vanishing coupling the ϕMDE is clearly visible between log(a) $\in (-3, -1)$.

In general, the equation of motion for the Lagrangian 3.12 reads

$$\Box\phi - \frac{\mathrm{d}V}{\mathrm{d}\phi} - \sum_q n_q \frac{\mathrm{d}m_q}{\mathrm{d}\phi} = 0 \ , \tag{3.19}$$

where q runs over all the Dark Matter particle types.
The last term in the above equation gives rise to a long-range fifth force acting between the Dark Matter particles, as described in detail in Section 3.3.

3.3 Multi coupled Dark Energy

I am now going to describe in detail the model studied in this Thesis. A further generalization of the model presented in the previous Section is to allow the Dark Matter to be composed by multiple species of particles. Such possibility has been proposed in a number of different theoretical frameworks, *e.g.* in [28]. In particular a model with n different types of Dark Matter particles has been studied in [29], where it was shown that, considering only the linear regime, the evolution of the perturbations is the same as in the ΛCDM model. However, when looking at the non-linear evolution, there are differences that can be marked at small scales.
The most remarkable feature of this class of models is the presence of a new (fifth) scalar force between the particles, that can be either repulsive or attractive:

$$F = G\frac{m_1 m_2}{r^2} + \frac{1}{4\pi r^2}\frac{\mathrm{d}m_1}{\mathrm{d}\phi}\frac{\mathrm{d}m_2}{\mathrm{d}\phi} \equiv G\frac{m_1 m_2}{r^2} + \frac{Q_1 Q_2}{4\pi r^2} \ , \tag{3.20}$$

where the scalar "charge" Q_n has been defined in close analogy with the Coulomb force. Note that these are called charges even if they are not conserved. This is a long-range fifth force that has the effect of modifying the total force experienced by a particle, in such a way that it can be seen as a gravitational force modified by a multiplier term

$$\beta_{ab} = 1 + \frac{Q_a Q_b}{4\pi G m_a m_b} \tag{3.21}$$

with a sign that depends on the two particle types involved. For values of the coupling that make the background and linear perturbations match the observed properties of the Universe, this fifth force can have a strength even comparable with the standard gravity.

The McDE model is the simplest model of the family described in [29], since it features only two different types of particles with opposite constant couplings with respect to the scalar field. This can be interpreted as a hint pointing in the direction of a DM-DE coupling that originates from a new fundamental symmetry in the Dark Sector.

As stated before, the role of Dark Energy is played by a classical scalar field ϕ with a self-interaction potential $V(\phi)$ of the form

$$V(\phi) = Ae^{-\frac{\alpha\phi}{M_{PL}}} \ , \tag{3.22}$$

where $M_{PL} = (8\pi G)^{-1}$. The background evolution of this cosmology is ruled by the following equations:

$$\ddot{\phi} + 3H\dot{\phi} + \frac{\mathrm{d}V}{\mathrm{d}\phi} = C\rho_+ - C\rho_- \ , \tag{3.23}$$

$$\dot{\rho}_+ + 3H\rho_+ = -C\dot{\phi}\rho_+ \ , \tag{3.24}$$

$$\dot{\rho}_- + 3H\rho_- = C\dot{\phi}\rho_- \ , \tag{3.25}$$

$$\dot{\rho}_r + 4H\rho_r = 0 \ , \tag{3.26}$$

$$3H^2 = \frac{1}{M_{PL}}(\rho_r + \rho_+ + \rho_- + \rho_\phi) \ , \tag{3.27}$$

where ρ_+ and ρ_- are the densities of the species of Dark Matter with positive and negative coupling, respectively, a dot is, as usual, a derivative with respect to cosmic time and C is the coupling strength, expressed from now on using the dimensionless parameter

$$\beta \equiv \sqrt{3/2}M_{PL}C \ . \tag{3.28}$$

This type of interaction in the Dark Sector produces an interesting feature: a time-dependent evolution of the mass of the two species of Dark Matter particles according to

$$\frac{\mathrm{d}\ \ln(m_\pm/M_{PL})}{\mathrm{d}t} = \mp C\dot{\phi} \ , \tag{3.29}$$

which promotes a time-dependent asymmetry between the two particles types whenever $\dot{\phi} \neq 0$. As shown by [38] the presence of multiple types of Dark Matter particles (MDM models) acts, in the background dynamic, as a single Dark Matter component with time-dependent coupling

$$\beta_{eff} = \frac{\sum_i \beta_i \Omega_i}{\sum_i \Omega_i} \ , \tag{3.30}$$

where Ω_i are the density parameters of the different Dark Matter components. Thanks to this behaviour, the McDE model can reproduce the background evolution of a model with a time-dependent coupling without the need to decide *a priori* a functional form of the coupling functional.
The effective coupling can also be expressed through the asymmetry parameter μ, defined as

$$\mu \equiv \frac{\Omega_+ - \Omega_-}{\Omega_+ + \Omega_-} \ , \tag{3.31}$$

which quantifies how much the relative densities of the two species of Dark Matter particles differ. In fact, since their masses change whenever $\dot{\phi} \neq 0$, there is an asymmetry between them, even in the case of a symmetric initial condition, *i.e.* $\mu_\infty \equiv \mu(z = \infty) = 0$. Taking into account that, for the model described, there are only two types of Dark Matter particles and their couplings β_j are opposite, β_{eff} can be rearranged as

$$\beta_{eff} = \frac{\beta\Omega_+ - \beta\Omega_-}{\Omega_+ + \Omega_-} = \beta\mu \ . \tag{3.32}$$

One of the most interesting features shown by the Equation 3.32 is that in the case of a perfectly symmetric situation (*i.e.* $\mu = 0$), the effective coupling vanishes, thus the model mimics a minimally coupled quintessence model.

Before analysing the background and linear perturbations evolution of the model, it is important to stress that the McDE model needs only two additional parameters with respect to the ΛCDM model: the slope of the self-interaction potential α and the coupling strength β, *i.e.* the same number of parameters as the standard coupled quintessence models, one more than the uncoupled quintessence. The μ_∞ parameter is just a way to parametrise the initial conditions through the asymmetry between the two CDM species.

The baryonic component is discarded throughout the following analysis since its presence has only minor effects on the main characteristics of the model, which can, thus, be satisfactorily described using a simplified CDM-only system. The previous claim is supported by the work [8], where the McDE model was studied in the presence of baryons both at the background and the linear perturbations level.

3.3.1 Background evolution

The background and linear perturbations evolution of this model is widely studied in [2] and I report here the main features. The evolution of the model is described by the set of equations 3.23-3.27, which have been numerically integrated. The reference background cosmology chosen is a quintessence cosmology (*i.e.* $\beta = 0$) with slope $\alpha = 0.08$.
The numerical integration of the background cosmology started with a set of cosmological parameters compatible with the constraints obtained from the data of the WMAP7 satellite [37] and proceeded backward in time deeply into the radiation dominated era ($\Omega_\gamma > 0.999$). The value of μ_∞ is irrelevant since, due to the absence of coupling, the two Dark Matter particle types behave at the same way, indistinguishably from the case of a single Dark Matter component.
Once a very high redshift (order of 10^7) is reached, the final state of the integration is taken as the initial condition for the integration forward in time assuming the different McDE models, *i.e.* the cosmologies with different values of β and μ_∞, while α was kept fixed since changing its value did not show any effect on the main features of the model. Such procedure does not guarantee that the final states of the different cosmologies are compatible with the observed properties of the Universe, but on the other hand it provides

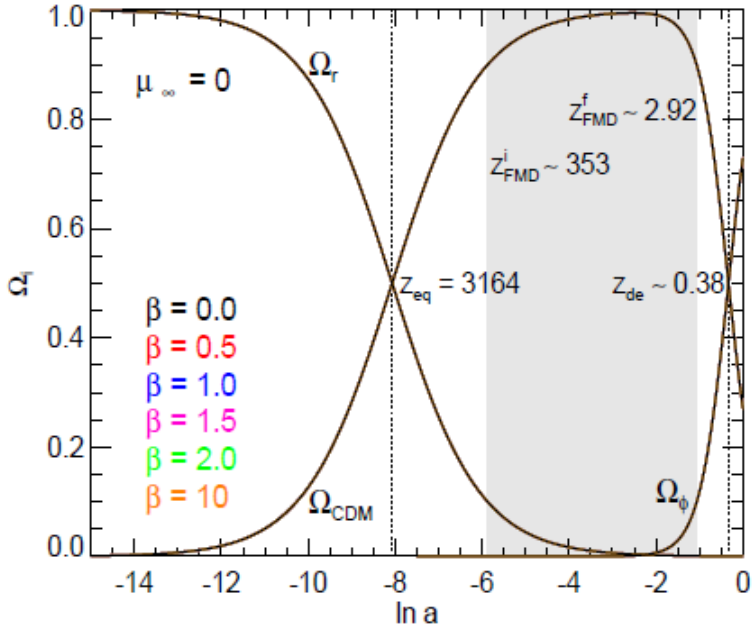

Figure 3.3: The background evolution of an uncoupled cosmology identical to ΛCDM (black curves) and of a series of McDE models with symmetric initial conditions and different coupling values. The greyshaded area represents the FullMatter Dominated phase ($\Omega_{CDM} > 0.9$) and the vertical dotted lines correspond to CDM-radiation and CDM-DE equivalence. As the plot shows, symmetric McDE models with couplings as large as $\beta = 10$ are completely indistinguishable from ΛCDM in the background. The Figure is taken from [2].

a safe way to compare the McDE model to the ΛCDM one.

The most natural model is the one with vanishing primordial asymmetry, since the particles can be thought as degenerate in mass and produced out of thermal equilibrium in the early Universe.
For these models it is reasonable to investigate values of the coupling as large as 10, which would be in strike contrast with observations as Large Scale Structure, Lyman-α and CMB observations (see *e.g.* [31] [33] [34]) for the standard coupled quintessence, since the presence of opposite couplings and the symmetric initial conditions suppress the effect of the fifth force. Even for such large couplings, the effects on the background evolution are insignificant, as clearly shown in Figure 3.3, where the evolution of the density parameters is shown and the McDE model appear indistinguishable from the ΛCDM one even for very high couplings.

A further check of the insensitivity of the background evolution to the coupling value is shown in Figure 3.4, where the ratio between the Hubble function $H(z)$ and the same function for the reference cosmology H_Λ is plotted. It is clearly shown that this ratio departs from 1 only at low redshifts, when the Dark Energy starts to emerge. However,

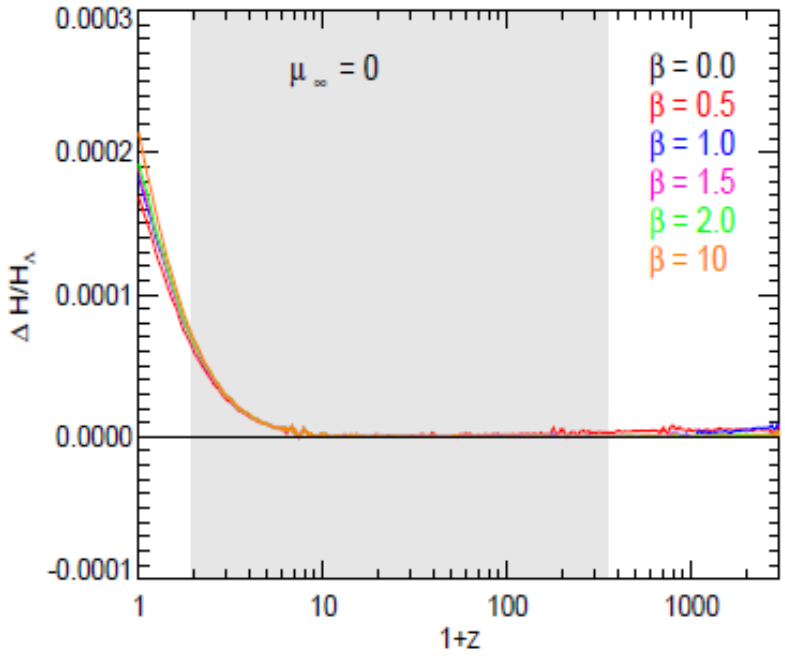

Figure 3.4: The ratio of the Hubble function $H(z)$ over the ΛCDM Hubble function H_Λ for the same symmetric McDE models of Figure 3.3. The expansion histories of all the models are indistinguishable from ΛCDM until the end of matter domination, where some deviations start to appear. However, such deviations never exceed a few hundredths of a percent and are therefore clearly undetectable. Therefore, the expansion histories of symmetric McDE models are completely indistinguishable from ΛCDM even for couplings as large as $\beta = 10$. The Figure is taken from [2].

the difference with respect to the reference cosmology (which is important to stress it is undistinguishable from the ΛCDM model) is less than a few hundredth of a percent.

An interesting feature is reported in Figure 3.5. At high redshifts, during the radiation-dominated era, although the asymmetry parameter is set to zero in the initial conditions, as soon as the scalar field starts to evolve (*i.e.* $\dot{\phi} \neq 0$) the masses of the two particle types are modified in different ways and, therefore, the asymmetry parameter departs from its vanishing value. However, as the Universe approaches the matter-dominated epoch, the value of β_{eff} is driven toward a null value again and it is locked to this null coupling until Dark Energy takes over.
This behaviour is the result of the presence of a critical point in the phase-space of the system of equations 3.23-3.27 defined by the condition

$$\sum_j \beta_j \Omega_j = 0 \tag{3.33}$$

This critical point was first described by [38], while a detailed analysis of the critical points of the McDE phase-space can be found in [7]. This feature can be better understood by

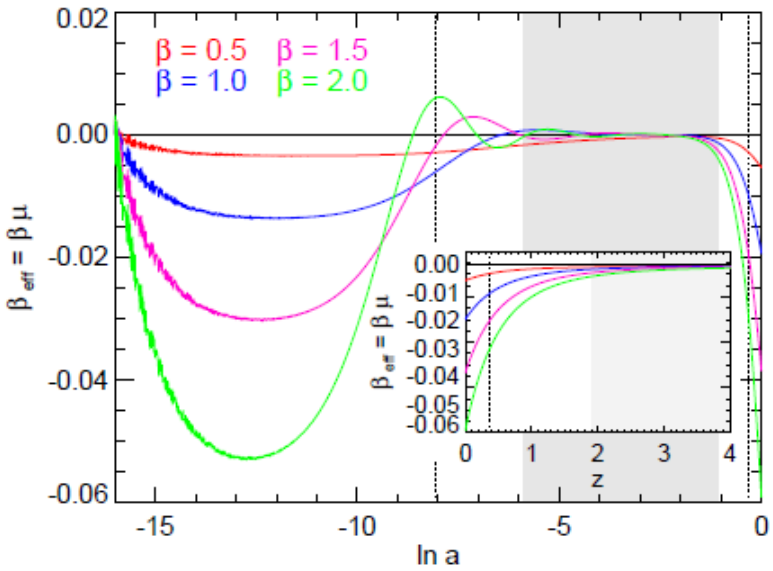

Figure 3.5: The effective coupling of symmetric McDE models as a function of the e-folding time $\ln(a)$. The system is attracted towards the uncoupled critical point $\mu = 0$ during matter domination, despite the deviation from the initial symmetry that develops in radiation domination. After the end of matter domination these cosmologies evolve again to effectively negatively coupled systems due to the onset of DE domination. The small box shows a zoom of the same quantities as a function of redshift for $z < 4$. The Figure is taken from [2].

looking at the evolution of the scalar field ϕ, reported in Figure 3.6. The scalar field settles to a constant value during almost all the matter-domination period. Thus, since the source term in the equations 3.24-3.25 responsible for the coupling through an exchange of energy-momentum is directly dependent on $\dot{\phi}$, the system behaves as uncoupled one whenever the scalar field assumes a constant value.

Turning to the asymmetric models, the asymmetry between the two Dark Matter components weakens the screening effect of the coupling. Due to the presence of the critical point described above, the effective coupling is dragged toward a vanishing value during the matter domination. The evolution of the effective coupling and of the asymmetry parameter for different models are shown in Figure 3.7 and 3.8, respectively. Both the figures show that the efficiency of the dilution of the initial asymmetry is proportional to the inverse of the coupling parameter β. On the other hand, looking at models with the same coupling, the ones with the larger primordial asymmetry take longer to be driven to a symmetrical state in matter domination epoch.

The results listed above show one of the most important features of the McDE model: it provides a self-regulating mechanism for the dark sector interactions. In fact, the effective coupling of the background is pushed toward zero during matter domination, in such a way that the model behaviour mimics the one of the ΛCDM model even in the presence

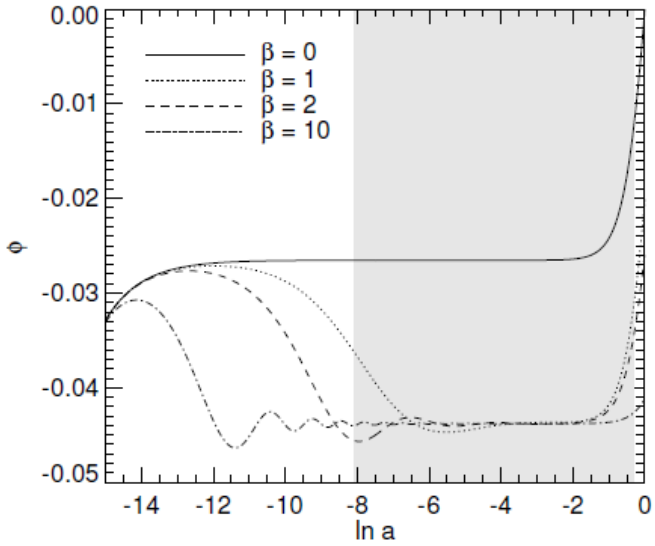

Figure 3.6: The evolution of the DE scalar field ϕ as a function of the e-folding time $\ln a$ in an uncoupled scenario (solid) and in McDE cosmologies with different values of the coupling β (dotted, dashed, and dotdashed). As one can see from the figure, after the initial evolution the scalar field gets trapped in the minimum of its effective self-interaction potential during most of matter domination (represented by the grey-shaded area) and during this period behaves like an uncoupled field. The Figure is taken from [3].

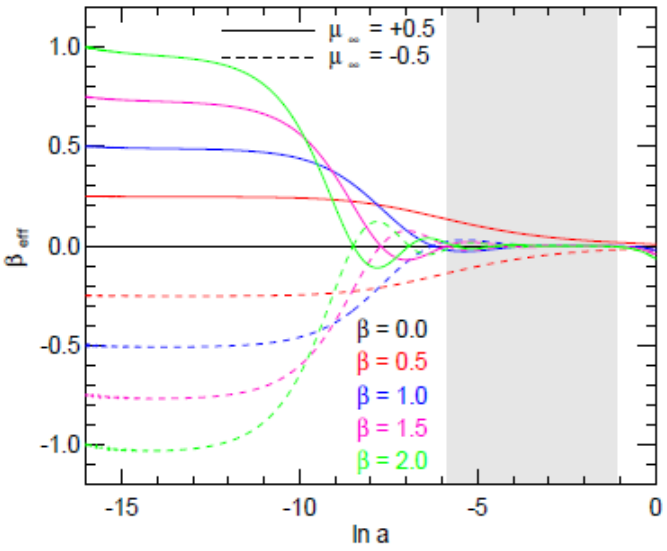

Figure 3.7: The effective coupling for a series of asymmetric McDE models ($\mu_\infty = \pm 0.5$) with different coupling values. All the models, irrespectively of the initial asymmetry, are attracted towards a symmetric state during matter domination, but the dragging appears more efficient for models with a larger coupling β. The Figure is taken from [2].

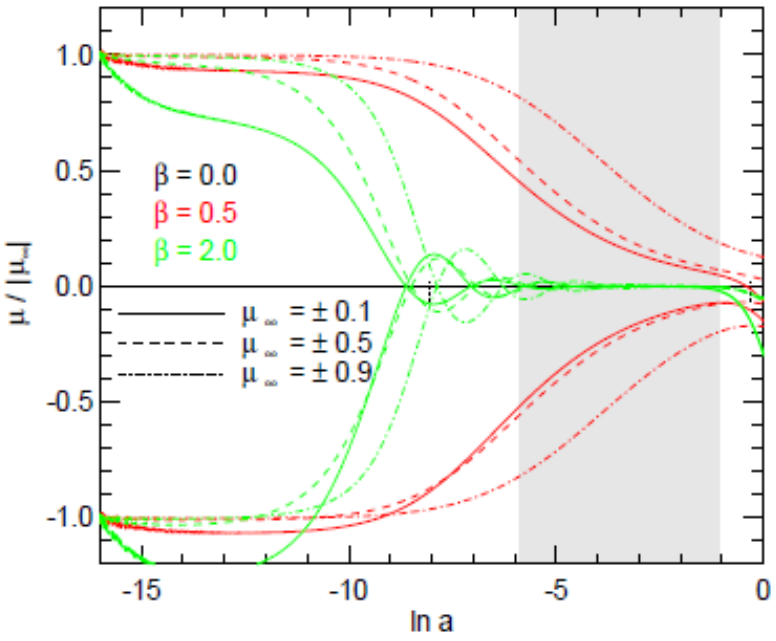

Figure 3.8: The relative suppression of the primordial asymmetry for McDE models with different values of μ_∞ and for two extreme values of the coupling, $\beta = 0.5$ (red) and $\beta = 2$ (green). The larger coupling proves to be much more effective in dragging the system to the symmetric critical point in matter domination. The Figure is taken from [2].

of a strong coupling between Dark Matter and Dark Energy and even in the presence of a relatively high asymmetry parameter.
Figure 3.8 shows that a large primordial asymmetry is ruled out by observational constraints since it significantly differs from the ΛCDM (or reference) cosmology. However, small values of μ_∞ are indistinguishable from the reference model for what concerns the background evolution. Moreover, the fact that a small asymmetry between the two Dark Matter species does not provide any appreciable difference in the background evolution means that the self-regulating mechanism described does not require a fine tuning of the initial conditions for what concerns the Dark Matter particles proportion.

3.3.2 Linear perturbations

In order to study the evolution of the density perturbations, we introduce the density contrast for the two Dark Matter species $\delta_\pm \equiv \delta\rho_\pm/\rho_\pm$. As shown in [5], the evolution equations are:

$$\ddot{\delta}_+ = -2H\left[1 - \beta\frac{\dot{\phi}}{H\sqrt{6}}\right]\dot{\delta}_+ + 4\pi G\left[\rho_-\delta_-\Gamma_R + \rho_+\delta_+\Gamma_A\right] \ , \tag{3.34}$$

$$\ddot{\delta}_- = -2H\left[1+\beta\frac{\dot{\phi}}{H\sqrt{6}}\right]\dot{\delta}_- + 4\pi G\left[\rho_-\delta_-\Gamma_A + \rho_+\delta_+\Gamma_R\right] \ , \tag{3.35}$$

where the two terms

$$\Gamma_A \equiv 1+\frac{4}{3}\beta^2, \ \Gamma_R \equiv 1-\frac{4}{3}\beta^2 \tag{3.36}$$

are the corrections due to the scalar fifth force to the gravity force felt by the Dark Matter particles.
As I will show later, an important feature of equations 3.34-3.35 is the sign in the friction term, which is different for the two Dark Matter species.

Now I focus on the density perturbations in the matter-dominated epoch, when the contribution of the relativistic components can be neglected.
For isocurvature perturbations, *i.e.* perturbations which do not modify the curvature of the Universe, the condition

$$\delta_+\Omega_+ + \delta_-\Omega_- = 0 \tag{3.37}$$

is fulfilled. In this case, the source term in equations 3.34-3.35 is given only by the fifth force, whilst the standard gravity disappears from the equations.
A superposition of density perturbations with opposite contrast in the two Dark Matter species evolves in such a way that the overdense one keeps growing in density while the underdense one becomes progressively more underdense. Thus, in this model the isocurvature perturbations grow with time.

On the contrary, for the adiabatic perturbations (which fulfil $\delta_+\Omega_+ = \delta_-\Omega_-$) the source term corrections due to the scalar fifth force vanish, leaving a source term given only by the standard gravity. The adiabaticity condition is bound to be broken since the friction term has an opposite sign for the two Dark Matter species whenever $\dot{\phi} \neq 0$, thus the evolution is different even if the source term is only gravitational. Therefore, any perturbation of the adiabaticity condition will restore the fifth-force-induced Γ corrections in the source terms, and for couplings $\beta > \sqrt{3}/2$ the two matter species will mutually repel. The overdense species will start growing while the underdense will decay. However, it is important to realize that the overdensities growth will always be faster than the depletion of the other Dark Matter species, since the scalar force term is opposite but the gravitational one is obviously attractive for both the species.
Hence, the adiabatic perturbations are unstable and tend to evolve into isocurvature perturbations. This feature is typical of the McDE model, since it is related to the coupling β and vanishes when the coupling is set to zero. In the latter case, the adiabatic perturbations remain adiabatic. However, this effect is modest for coupling values up to $\beta \approx 1.5$.

For the purpose of this Thesis, the most interesting model turns out to be a symmetric model ($\mu_\infty = 0$), which is also the most "natural", as discussed above. For the same reason, only initially adiabatic fluctuation are considered.

Once we define the total CDM density perturbation as

$$\delta_{CDM} \equiv \frac{\delta_+ \Omega_+}{\Omega_{CDM}} + \frac{\delta_- \Omega_-}{\Omega_{CDM}} \ , \tag{3.38}$$

the total linear growth factor for the Dark Matter can be obtained by numerically integrating equations 3.34-3.35. The results are shown in Figure 3.9 as the ratio of δ_{CDM} to the ΛCDM case, where it clearly appears that for the higher coupling values the growth factor is larger with respect to the ΛCDM case, resulting in an enhanced growth of the perturbations at low redshifts. Thus, the predicted value of σ_8 today is far bigger than the observed one.
However, for coupling values of order unity or less, the growth factor is undistinguishable from the one predicted by the reference model. Hence, this feature allows to rule out part of the parameters space for the McDE model, which would be otherwise perfectly viable at the background level. As an example, I showed above that the background evolution is the same as the ΛCDM cosmology also for couplings as large as $\beta = 10$, while turning to the linear perturbations evolution coupling values above unity are ruled out by the extremely fast growth of the perturbations.

The last feature described is starkly visible in Figure 3.10, where the density contrasts of a Gaussian perturbation in the two species of Dark Matter is shown as a function of redshift and coupling. The plots clearly show that, with the exception of the most extreme case ($\beta = 3/2$), the global CDM perturbation δ_{CDM} is indistinguishable from the prediction of the ΛCDM model. This is due to the fact that, even if the two different components evolve in different ways, the global perturbation still follow the ΛCDM model. Hence, the probes based on the linear perturbations do not allow to distinguish McDE models with coupling as large as $\beta = \sqrt{3/2}$ (*i.e.* with a scalar force twice as strong as gravity) from the ΛCDM model.

3.3.3 Non-linear perturbations

As shown above, when restricting to the background evolution and linear perturbations, the McDE models behave the same as the ΛCDM cosmology if the coupling is below unity (which means a scalar fifth force as strong as gravity). In order to break the degeneracy between these models, the non-linear evolution of the perturbations must be analysed. To this end, a number of cosmological N-body simulations were performed. The detailed discussion of such simulations can be found in [3] and [4]. The code used for the simulations is a modified version [6] of the widely used code GADGET-3 [39, 40]. In Section 4.2.2 the code is extensively described.
These first simulations showed a number of peculiar features of the McDE model which could in principle allow to distinguish this model from the ΛCDM one. The most striking of these features is the fact that, also at a qualitative level, the two types of Dark Matter particles develop the same large-scale structures but shifted one from the other, as can be clearly seen in Figure 3.11. It is interesting to note that for coupling values up to $\sqrt{3}/2$ (which is equivalent to a fifth force as strong as gravity) the situation is almost

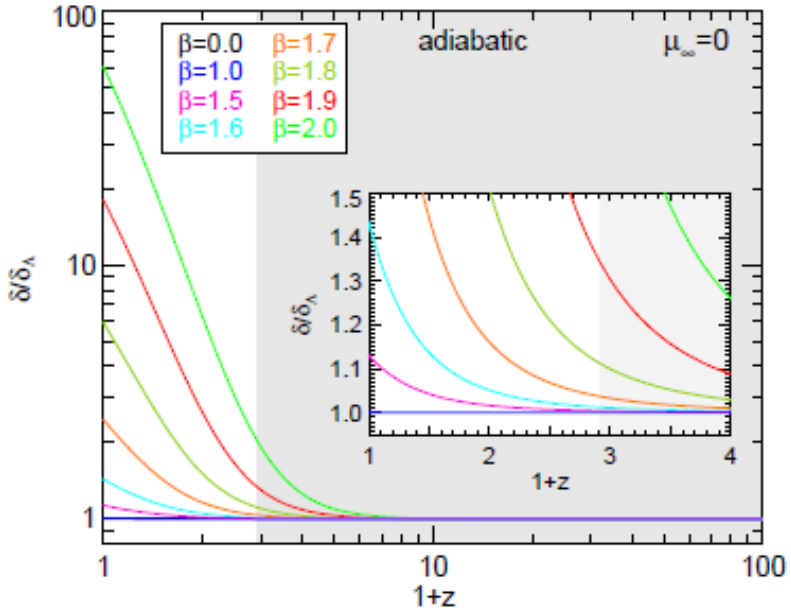

Figure 3.9: The ratio of the growth factor of CDM density perturbations to the ΛCDM case for a series of McDE models with couplings between $\beta = 1$ and $\beta = 2$ and with adiabatic initial conditions. As one can see in the plot, couplings larger than $\beta = 1.6$ (cyan curve) determine an overall enhancement of the amplitude of linear perturbations at $z = 0$ exceeding 40%, while a coupling $\beta = 1.5$ (magenta) would induce an enhancement of just 13% and a coupling $\beta = 1$ does not induce any boost in the growth of perturbations, thereby resulting indistinguishable from ΛCDM. The small box shows a zoom of the same quantities on a linear scale and at low redshifts. The Figure is taken from [2].

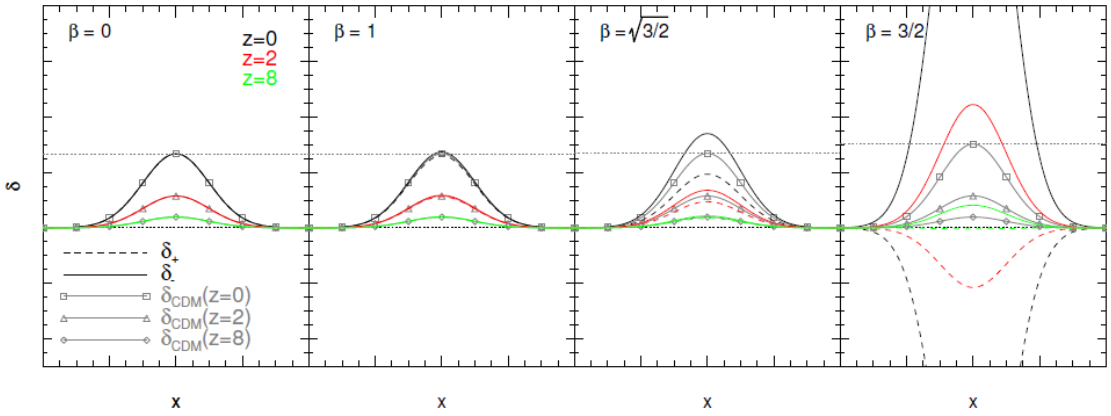

Figure 3.10: The evolution of a Gaussian density profile in real space for the positively- and negatively-coupled CDM species (dashed and solid lines, respectively) and for the total CDM density perturbation (grey solid lines) at redshifts $z = 0,\ 2,\ 8$ (black, red, and green colors, respectively). The plot shows the overdensity profile $\delta(x)$ as a function of a radial comoving coordinate x in arbitrary units. The grey squares, triangles, and diamonds are overplotted to highlight the shape of the total CDM density perturbation in ΛCDM at the three different redshifts considered in the plot. The horizontal dotted grey lines show the total amplitude of the CDM density perturbations at $z = 0$. In the left panel, corresponding to an uncoupled case $\beta = 0$, no difference can be seen in the time evolution of the density profiles of the various components, while when progressively increasing the coupling value, moving to the right panels, one can start noticing a slight difference in the evolution of the positively- and negatively-coupled CDM species at low redshifts already for $\beta = 1$. The effect becomes more evident (and appears at earlier times) for larger values of the coupling, and for the most extreme case of $\beta = 3/2$ the two CDM species develop opposite density profiles by the present time, thereby showing the formation of isocurvature modes. Nevertheless, the total CDM perturbation amplitude is only mildly affected by this strikingly different evolution of the two individual CDM components. The Figure is taken from [3].

indistinguishable from the reference cosmology (upper left panel), confirming the results obtained from the analysis of the background and linear perturbations evolution. Moving to higher couplings, the cosmic web structure starts to segregate, producing a sort of two "mirror" copies, each one composed almost entirely by one type of Dark Matter particles. Furthermore, as the coupling becomes bigger, the structures become more concentrated, as a result of the enhanced total force felt by the particles, which thus form structures more efficiently.

Looking at Figure 3.12, where the power spectra of the two Dark Matter components are shown along with the total CDM power spectrum and the ratio of the power spectrum in the coupled cases to the reference one, it appears clear once again that couplings as large as $\beta = 1/2$ does not produce any difference in the power spectrum with respect to the ΛCDM model. As the coupling is increased, some effects start to appear. In particular, a suppression of the CDM power spectrum with respect to the ΛCDM one appears at small scales. For even larger couplings (*e.g.* $\beta = \sqrt{3/2}$) the suppression is shifted to larger scales, while for smaller scales the power spectra become again similar to the ΛCDM one, although remaining visibly different. Thus, another peculiar feature of the McDE model can be identified in the power spectrum, which shows a dip which moves to larger scales with increasing couplings. This effect can be easily explained through the above described effect of segregation of the cosmic structures: the most massive objects segregate into smaller objects with roughly half the mass of the starting object. This process of segregation is more efficient for large couplings, which are able to segregate also bigger objects, thus shifting the dip in the power spectrum to larger scales.
This is a peculiar feature of the non-linear evolution, since the segregation is triggered by local deviations from the spherical symmetry of the objects, and hence can not be analysed using the linear evolution equations, nor the spherical collapse model.

Now I focus on the halo segregation process, which is the core of this Thesis. As shown in Figure 3.13, for couplings above the threshold given by a scalar force as strong as gravity ($\beta = \sqrt{3}/2$) the segregation process occurs. The objects highlighted by the circles and by a square are the ones for which the segregation is most marked. As in the large-scale structures, a single halo made of particles belonging to both the particle types progressively segregates into two sub-halos, each one composed only by particles of a single type. The analysis performed above is still valid also in this particular process, *i.e.* the segregation is due to the different friction terms for the different Dark Matter particles. Hence, this process is more dramatic where the halos move faster, *e.g.* for halos which are falling toward a more massive halo.
Moreover, those halos show an interesting fact: the halo fragmentation is not triggered by the scalar fifth force, since in the model with coupling $\beta = \sqrt{3}/2$ the particles of different type do not interact at all with each other, since the repulsive scalar force exactly balances the gravitational attraction. Thus, the onset of the fragmentation process cannot be a consequence of the repulsive force acting between the Dark Matter particles of different types but it is instead due to the different friction terms in equations 3.34-3.35. This is confirmed by the fact that the fragmented halos are aligned along the direction of the

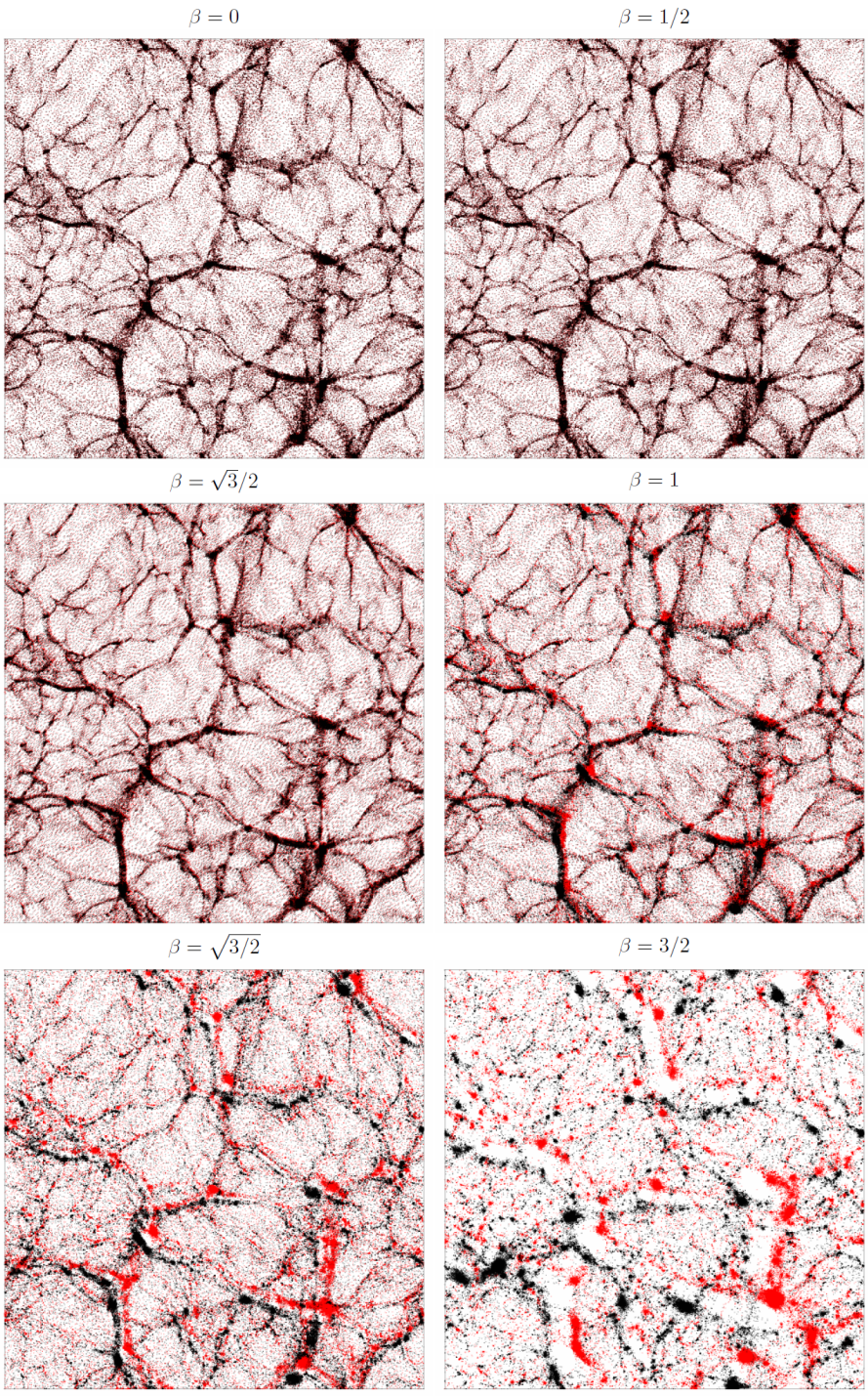

Figure 3.11: The distribution of the positively- and negatively-coupled CDM particles (red and black points, respectively) in a slice of $100 \times 100 \times 2Mpc/h$ for different values of the coupling β. The Figure is taken from [3].

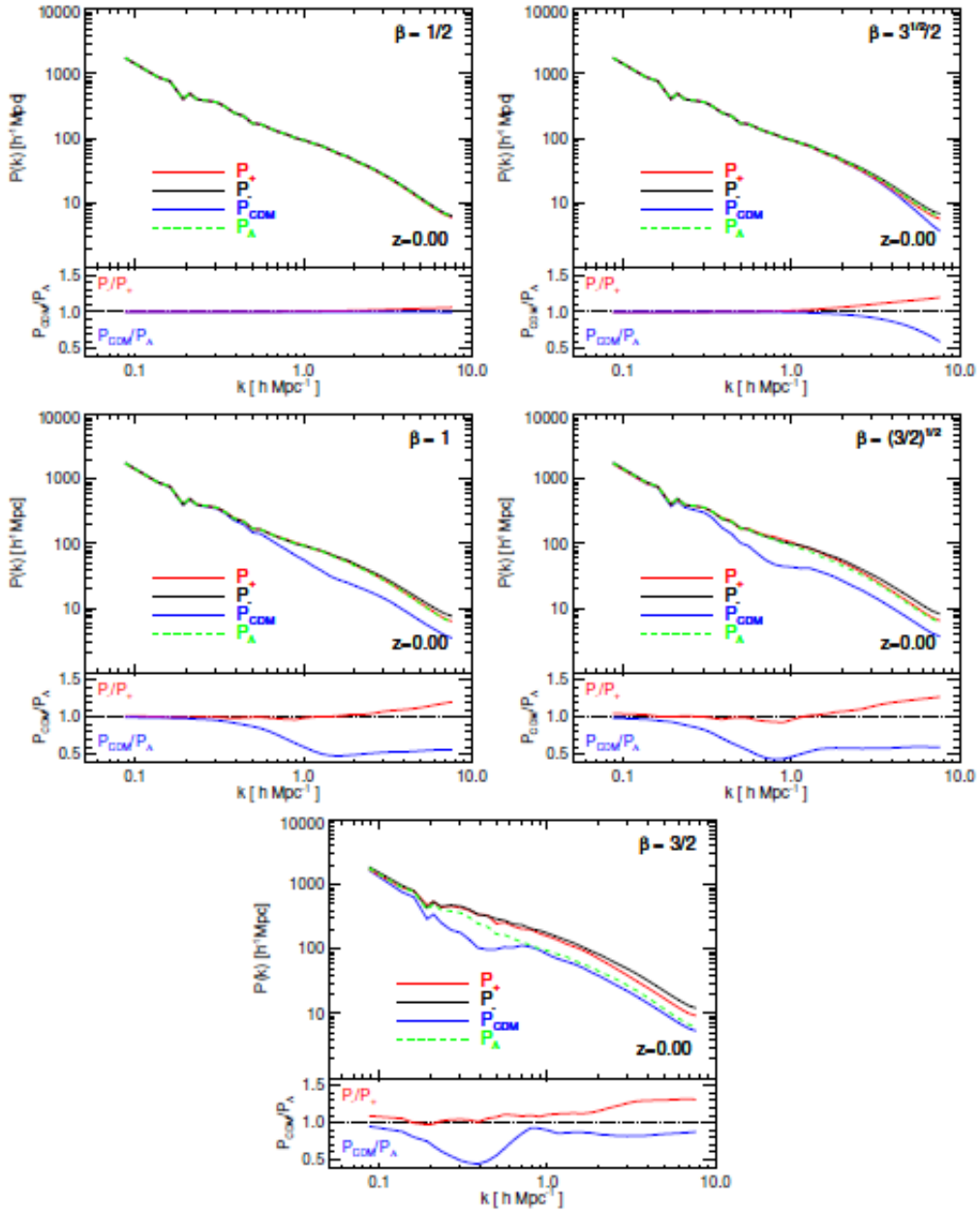

Figure 3.12: The upper plot of each panel displays the matter power spectrum of the positively- and negatively-coupled CDM species $P_+(k)$ and $P_-(k)$ and of the total CDM component $P_{CDM}(k)$, plotted as red, black, and blue solid lines, respectively, and the matter power spectrum of the standard ΛCDM cosmology overplotted for visual reference as a green dashed line, all at $z = 0$. The bottom plots show in red the ratio of the power spectra of the two different CDM components $P_-(k)/P_+(k)$ and in blue the ratio of the total CDM power spectrum to the ΛCDM reference case, P_{CDM}/P_Λ. This Figure is taken from [3].

filaments connected with the central high-density halos, suggesting that while the original un-fragmented halo moves toward the high-density central region, the particles experience a different friction term, resulting in a species that moves slower than the other, hence segregating from each other. This conclusion is supported by the fact that the separation between two halos originated from the same original halo grows in time along the direction of motion.
On the other hand, for coupling strengths below the gravitational threshold, the segregation process does not occur at all, and the presence of a scalar fifth force has the only effect of broadening the density distribution of the halos.

As stated before, the halo segregation process could help solving the cusp-core problem. The basic idea is exemplified in Figure 3.14: starting from a single massive halo with two equal Gaussian distributions of particles of different type, its total density distribution (plotted in red) is also Gaussian, provided the two single-type Gaussian distribution are peaked at the same centre. As the fragmentation of the halo displaces the centres of the two distribution, the total density profile flattens toward the centre, until in the final stage the system ends up with two separated Gaussian-shaped halos. It is well known that the density distribution of the matter in a halo is not Gaussian (see Section 1.3 or Section 4.1.3 for details), but the same idea can be applied to non-Gaussian profiles, which could result in a flat core profile, depending on the details of the segregation process, which can be studied only through numerical simulations, since they are a typical deeply-non-linear feature.

In a more quantitative way, we can analyse the halo mass function, *i.e.* the abundance of halos as a function of their mass, which is shown in Figure 3.15. With respect to the ΛCDM cosmology, it shows an enhancement at small masses and a corresponding suppression at intermediate masses. This transition mass grows with the redshift, as a consequence of the fragmentation process which segregates a halo in two substructures of roughly half the mass of the original one. Thus the Universe progressively loses intermediate-mass halos and correspondingly gains new smaller-mass halos. This process starts at small masses since the smaller objects in average have higher velocities, thus the friction term is more efficient.
Besides this, the halo mass functions show a significant reduction of high-mass halos for strong couplings, a feature that can help alleviate the tension between the latest observations about the abundance of clusters and the data obtained from the PLANCK mission [13] [14]. However, the production of a great number of small-size halos has the effect of worsening the "missing satellites" problem, and therefore could be used to constrain the McDE parameters.

As a final remark, the effects described, and in particular the halo segregation process, experiences a sharp transition between values of the coupling below the gravitational threshold $\beta = \sqrt{3}/2$, where the segregation process does not occur at all, and above, where the process is the most prominent feature of the model.

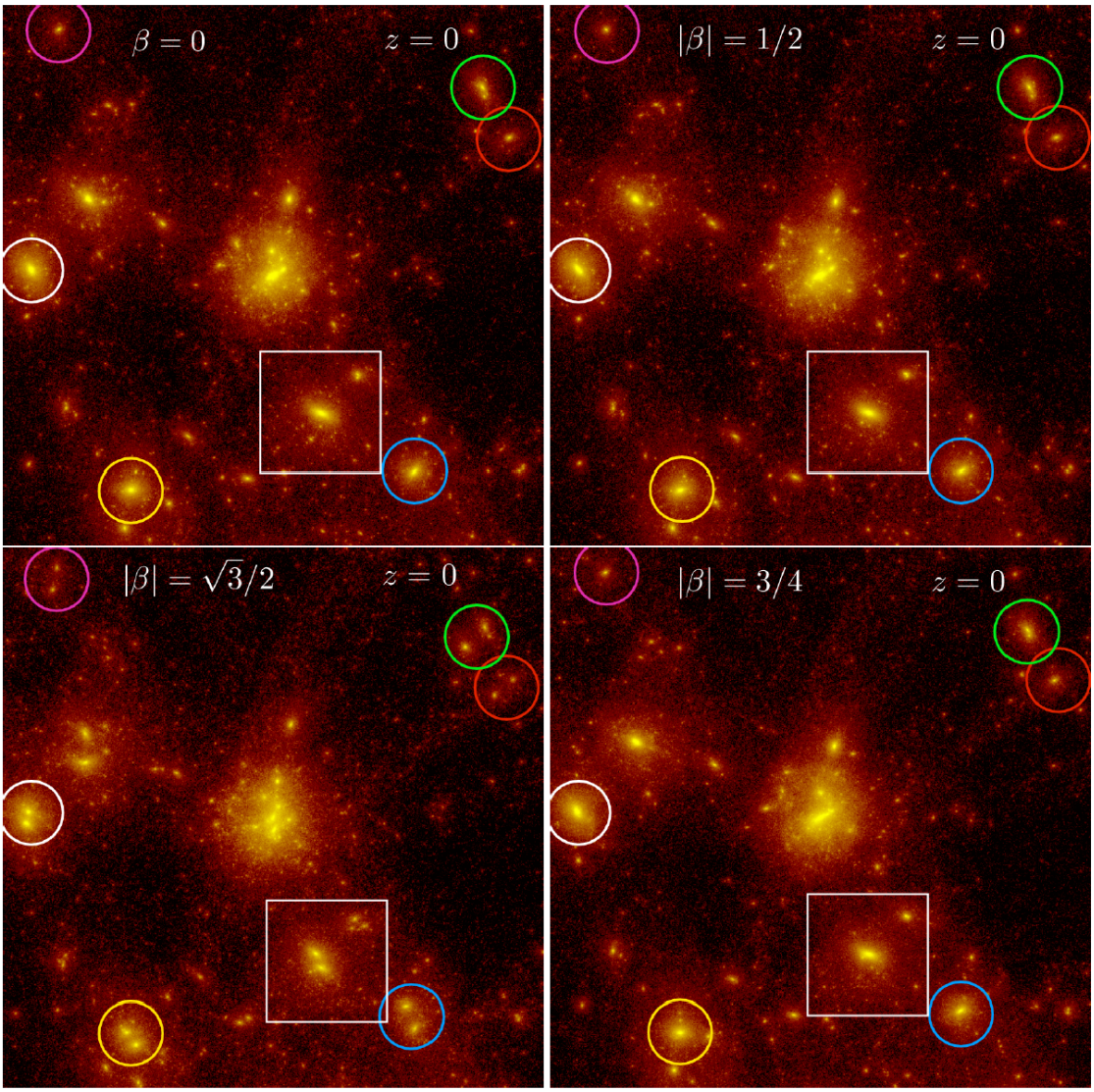

Figure 3.13: Zoom on the most massive halos of the simulation in four different McDE models with clockwise increasing coupling starting from the uncoupled case in the upper left plot. The size of each image is $10 \times 10 Mpc/h$, and the corresponding objects have been highlighted with coloured circles and a large square. The Figure is taken from [4].

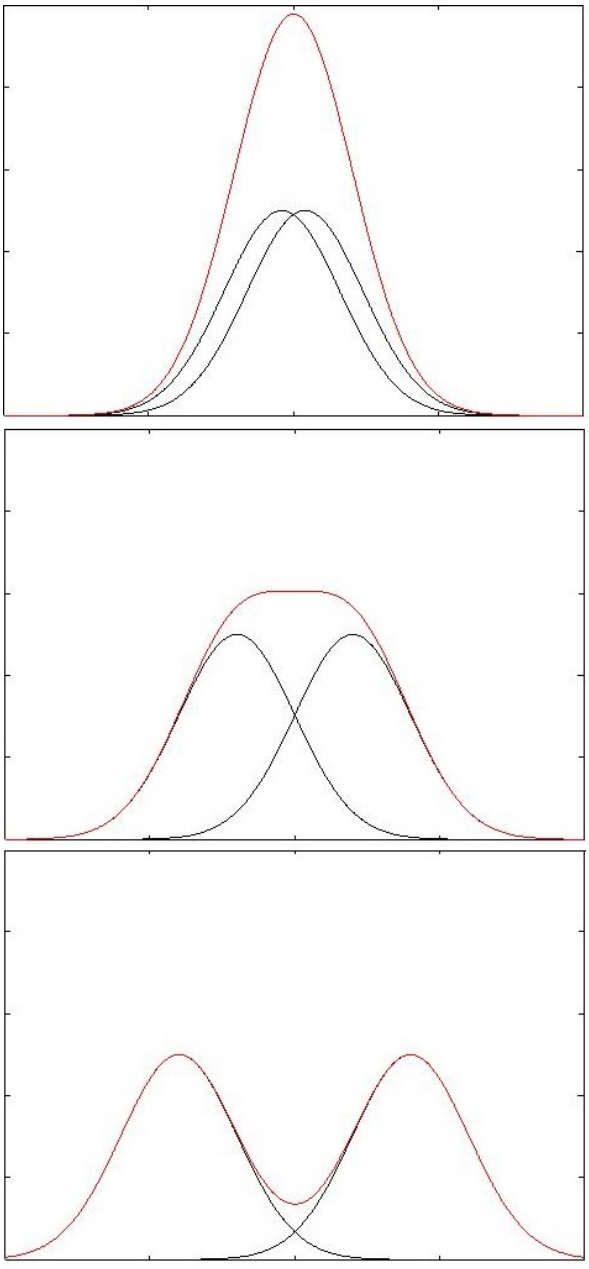

Figure 3.14: 1-D examples of the evolution of two Gaussian density profiles (black curves), one for each particle type, and their superposition (red curve), during the segregation process. The segregation process starts from the top panel and move to the central and bottom ones while time passes.

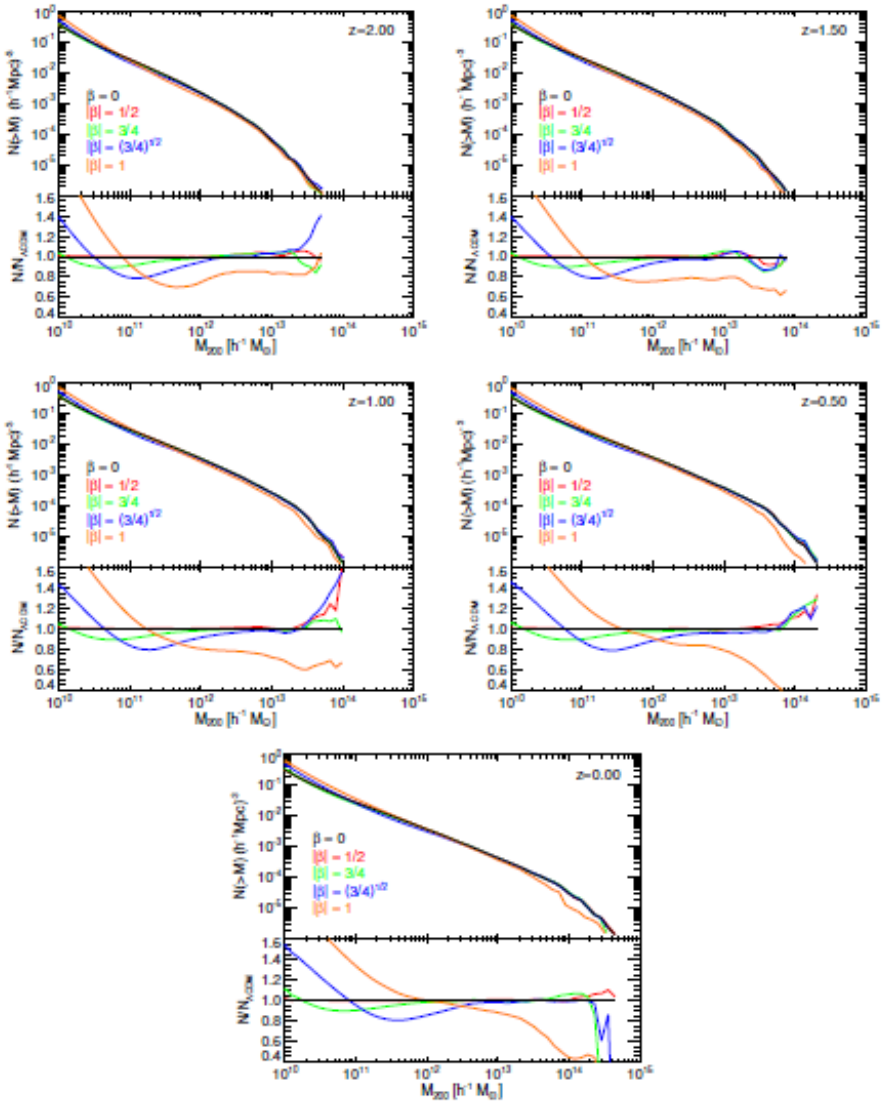

Figure 3.15: The cumulative halo mass function at different redshifts for various McDE scenarios. This Figure is taken from [4].

Chapter 4

Statistical and Numerical Tecniques

4.1 Statistical Tools

An important tool in the study of the Universe is statistics. Here after, we will describe the main tools that are used in the quantitative description of the Universe.

There is a conceptual issue which must be faced primarily: the statistical tools require the concept of average over different realizations of the same system. However, when the system to study is the Universe, its uniqueness prevents from the possibility to perform such average.
A possible way to overcome this problem is to average over different subsystems, distant enough to be considered independent from each other. The problem here is that we do not know how much is "distant enough". Hereafter I will use the *ergodic hypothesis*, *i.e.* I will assume that the subsystem (*sample*) average is a good approximation of the average over different realizations of the system (*ensemble*). This hypothesis is proved for Gaussian distributions.

4.1.1 Power Spectrum

The density fluctuations are produced by the initial inflation with random phases of δ_k. This randomness is encoded in the hypothesis of a Gaussian distribution $\delta(x)$, *i.e.* the distribution of the density contrast, with vanishing mean value.
The correlation function is defined as

$$\xi(r) \equiv \langle \delta(\vec{x})\delta(\vec{x}+\vec{r})\rangle \ , \tag{4.1}$$

where the lack of the vector symbol above the left-hand-side r stresses the fact that ξ is a function only of the modulus of the displacement $\vec{r}$. Inserting in the definition above the

expression of $\delta(\vec{x})$ in Fourier space, we obtain

$$\xi(r) = \int \frac{\mathrm{d}^3k}{(2\pi)^3} \int \frac{\mathrm{d}^3k'}{(2\pi)^3} \langle \delta(\vec{k})\delta(\vec{k'})\rangle e^{i\vec{k}\cdot\vec{x}} e^{i\vec{k'}\cdot(\vec{x}+\vec{r})} \ . \tag{4.2}$$

Furthermore, we define the power spectrum $P(\vec{k})$ as

$$\langle \delta(\vec{k})\delta(\vec{k'})\rangle \equiv (2\pi)^3 P(\vec{k})\delta_D^{(3)}(\vec{k}+\vec{k'}) \ , \tag{4.3}$$

where $\delta_D^{(3)}(\vec{k}+\vec{k'})$ is the Dirac delta distribution in the 3-dimensional space.
The homogeneity and isotropy hypothesis encoded in the cosmological principle ensures that

$$P(\vec{k}) = P(k) \ . \tag{4.4}$$

Therefore, the relation between the correlation function and the power spectrum is provided by

$$\xi(r) = \int \frac{\mathrm{d}^3k}{(2\pi)^3} P(k) e^{i\vec{k}\cdot\vec{r}} \ . \tag{4.5}$$

This relation shows that the power spectrum represents the "importance" of every mode $\delta(\vec{k})$ in the expansion of $\delta(\vec{r})$. It is a power density in Fourier space; the power is given by $\delta(k)\mathrm{d}^3k$.
It is customary to use the dimensionless quantity $\Delta(k)$, defined as

$$\Delta(k) \equiv \frac{1}{2\pi^2} P(k) k^3 \ . \tag{4.6}$$

The usually adopted ansatz for the primordial power spectrum is

$$P(k) \propto k^n \ , \tag{4.7}$$

where n is called spectral index. The prediction of most inflationary theories is: $n \approx 1$ (Zel'dovich spectrum), even though different inflationary models predict different deviations from this unitary value.

As stated before, the $\delta(\vec{x})$ distribution is a Gaussian distribution with vanishing mean value. However, its variance is non-vanishing and reads

$$\sigma^2 \equiv \langle \delta^2(\vec{x})\rangle = \sum_{\vec{k}} \langle |\delta_{\vec{k}}|^2\rangle \approx \frac{1}{2\pi^2} \int_0^\infty P(k) k^2 \mathrm{d}k \ . \tag{4.8}$$

The original power spectrum, *i.e.* the Zel'dovich spectrum predicted by inflation, is modified in many different ways, above all the different evolution of the perturbations at different scales. Here I recall only the main sources of deformation:

- Before the equivalence the Dark Matter perturbations grow independently of k outside the horizon, while inside they are frozen. But the horizon grows in time, so the perturbations that "cross" it are frozen at different times, and so the original power spectrum is modified in such a way that it presents a maximum in correspondence of the size of the cosmic horizon at the equivalence.

- The Dark Matter cancels the perturbations on scales below the scale of free-streaming, *i.e.* the scale under which the "dissipation" processes[1] due to the Dark Matter are stronger than the self-gravity and so the perturbations do not grow but vanishes. The free-streaming scale is extremely different for the Hot Dark Matter and the Cold Dark Matter.

- After the equivalence, the perturbations grow independently from k until they reach the non-linear regime, after which they start growing faster. Due to the identical evolution in the linear regime, the first perturbations which enter the non-linear regime are the perturbations that have started bigger, *i.e.* the perturbations of higher k.

4.1.2 Halo Mass Function

The halo mass function (HMF, hereafter) is defined as the number of halos of mass between M and $M + \mathrm{d}M$ as a function of M. It is used to study the impact of a cosmological model on the formation of structures.
There are several simulation-, experimental- or theorethically-inspired functional forms of $f(\sigma)$. To the latter category belongs *e.g.* the Press-Schechter model, which predicts

$$\frac{\mathrm{d}n(M)}{\mathrm{d}M} = f(\sigma)\frac{\bar{\rho}}{M^2}\frac{\mathrm{d}\log(\sigma^{-1})}{\mathrm{d}\log M} \ , \tag{4.9}$$

where $f(\sigma)$ is a multiplicity function that depends on the collapse model considered and $\sigma(R)$ is the variance associated to the filter function used to compute the HMF[2].
Alternatively, the one proposed by Sheth & Tormen [26]

$$f(\sigma) = A\sqrt{\frac{2a}{\pi}}\left[1 + \left(\frac{\sigma^2}{a\delta_c^2}\right)^p\right]\frac{\delta_c}{\sigma}\exp\left(-\frac{a\delta_c^2}{2\sigma^2}\right) \ , \tag{4.10}$$

where A, a and p are parameters of the model and δ_c is the linear overdensity at the collapse time.

[1] Please note that it is not a real dissipation process. The Dark Matter particles, once decoupled, travel freely through the Universe and thus wash out the density perturbations. The free streaming scale is approximately the length travelled by the Dark Matter particles since the decoupling.

[2] It is necessary a filter (or window) function in order to evaluate the HMF from observations or when analysing the output of a simulation. This is due to the fact that the halos are identified as mass concentrations above the mean density, but in order to evaluate the density contrast we need to average over a finite volume of space

A profile inspired by numerical simulations is the one proposed by Jenkins er al. [27]

$$f(\sigma) = (0.315)\exp\left(-|\log(\sigma^{-1}) + (0.61)|^{(3.8)}\right) \ . \tag{4.11}$$

4.1.3 Radial Density Profile

One of the main and earlier proofs of the existence of Dark Matter is given by the rotational curve of galaxies. Thanks to these profiles and to other observations, based on the satellite galaxies motion or globular clusters properties, it is possible to determine the mass distribution within a halo. The radial density profile is defined as the spherically averaged mass as a function of the radius, *i.e.*

$$\rho(r) \equiv \int_{\Sigma} \rho(\vec{r})\mathrm{d}\Sigma \ , \tag{4.12}$$

where Σ is a spherical shell of radius r and thickness dr.

Analytical studies which tried to derive the radial density profile starting from the analysis of a spherical collapse, both in Einstein-de Sitter Universe ([83], [84]) and in open Universe ([85]), found a power law behaviour in the inner regions of the halo.
The simplest modelization of such a system is through the so-called singular isothermal sphere, *i.e.* a sphere in hydrostatic equilibrium

$$\frac{k_B T}{m}\frac{\mathrm{d}\rho}{\mathrm{d}r} = -\rho G\frac{M(r)}{r^2} \tag{4.13}$$

which produces a density profile

$$\rho(r) = \rho_0(r)\left(\frac{r_0}{r}\right)^{\alpha} \tag{4.14}$$

and a predicted velocity field

$$v(r) \propto r^{1-\frac{\alpha}{2}} \ . \tag{4.15}$$

Thus, for $\alpha = 2$ a flat velocity profile is predicted, similarly to the one observed (see Figure 1.1).
This model features a singularity in $r = 0$ whenever $\alpha > 0$. In order to avoid this clearly unphysical effect, the model has been modified with the aim of maintaining the same behaviour at large radii. The so called isothermal sphere model features a radial density profile described by

$$\rho(r) = \frac{\rho_0}{1 + \left(\frac{r}{r_0}\right)^2} \ , \tag{4.16}$$

where ρ_0 is the halo central density while r_0 is the core radius. The velocity distribution is given by

$$v(r) \propto \left[1 - \frac{r_0}{r}\arctan\left(\frac{r_0}{r}\right)\right]^{1/2} \ , \tag{4.17}$$

which is in good agreement with the observed rotation curves.
This model features a central core which accounts for most of the dark matter and extended almost as the optical disk, in order to account for the linear growth of the velocity profiles in the inner part of the cluster.

However, as explained in Section 1.2, the numerical simulations of the ΛCDM cosmology do not show this core-like behaviour. Instead, they are better described by a power law with a steep profile, the so-called "cusp". The fits derived from the earliest simulations showed a profile that in the most inner part of the halo is well described by $\rho \propto r^{-1}$.
The most used profile derived from numerical simulations is the Navarro-Frank-White profile [86], also called "universal density profile" or simply NFW profile:

$$\rho_{NFW}(r) = \frac{\rho_i}{\frac{r}{R_s}\left(1+\frac{r}{R_s}\right)^2} \,, \tag{4.18}$$

where ρ_i is a parameter related to the density of the Universe at the time of the halo's collapse and R_s is the characteristic radius of the halo.
Some simulations point toward an even steeper inner slope, as the ones in [87], which are well approximated by the profile

$$\rho_{Moore} = \frac{\rho_i}{\left(\frac{r}{R_s}\right)^{1.5}\left(1+\frac{r}{R_s}\right)^{1.5}} \tag{4.19}$$

which, as the NFW profile, provides a slope $\alpha = -3$ in the outer part of the halo.
A further modelization is provided by the Einasto profile

$$\rho_{Ein} = \rho_e \exp\left\{-d_n\left[\left(\frac{r}{r_e}\right)^{1/n} - 1\right]\right\} \,, \tag{4.20}$$

where n is related to the shape of the profile, d_n is a parameter linked to n that allows to use the density ρ_e measured at the effective radius r_e, *i.e.* the radius containing half of the total mass of the halo.

Turning to the measurement of the radial density profile from the results of a numerical simulation, a number of further problems arise, namely how to determine all and only the particles belonging to the halo and how to determine its centre. The former problem can be solved using a friends-of-friends (FoF) algorithm, which relies only on the positions of the particles. The basic idea is to start from a particle and "link" it to every particle distant less than a linking length λ. Then, each one of this "friends" is linked to every particle nearer than λ. The procedure is repeated until no particles that can be linked remain. The global "tree" constructed is the FoF halo. Such an algorithm is embedded in the code used for the simulations (which will be described in Section 4.2.2), then the FoF groups are produced by the code every time a snapshot is produced. The particle types which the code must process can be set in input.

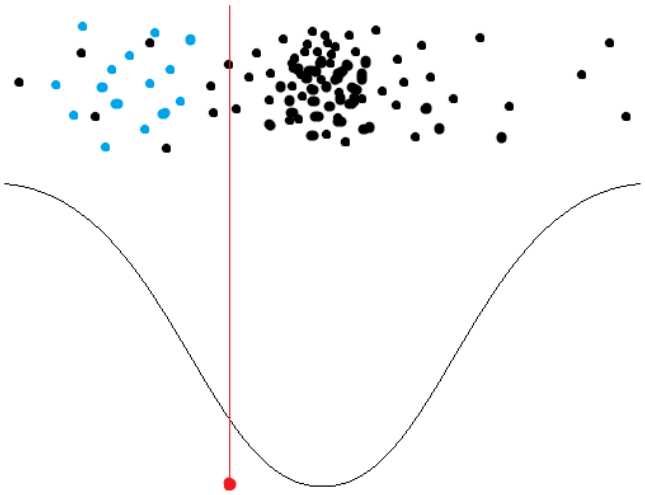

Figure 4.1: Schematic representation of the problems connected to using the centre of mass instead of the minimum of the potential as halo centre. The black dots are particles of the halo at equilibrium, the blue ones are particles moving toward the minimum of the potential (plotted below). The centre of mass (showed in red) does not coincide with the minimum of the potential.

The FoF algorithm's major weakness is the fact that it is not capable to distinguish between a gravitationally-bound structure and a gravitationally-unbound set of near particles (*e.g.* two groups which are passing one near the other), which will be seen as a single halo. For this reason, an algorithm called SUBFIND is also embedded in the simulation code. It considers other properties of the particles and identifies the sub-groups as overdense and self-bound structures (see [88]).

Using as halo centre its centre of mass is not safe, since it can happen that not all the particles of the halo are in their rest positions with respect to the halo. In fact, if the latter are still moving towards the halo centre, it could happen that the centre of mass does not coincide with the minimum of the gravitational potential. As an example, consider the sample situation in Figure 4.1, where there is a set of particles (plotted in black) at rest and a series of particles (plotted in blue) moving toward (or away from) the minimum of the potential, plotted below. As an example, this situation could be the result of two halo merging or segregating, as expected from the McDE model. As shown in red, the centre of mass of the halo does not coincide with the minimum of the potential.

In order to find the minimum of the potential, the SUBFIND algorithm is not suitable for the purpose of this Thesis, since I need to determine the centres of two sub-halos, each of which is composed almost entirely by a single type of particles. Although this can be obtained using the SUBFIND algorithm, the output would be extremely more difficult to analyse. Hence, an alternative approach must be found. The algorithm used relies once

again only on geometrical properties: once provided in input the particles belonging to the group to process and an approximate value of its center, the code computes the total mass within a sphere centred in the coordinates provided. Then, the centre is moved in every direction and the mass is computed again. If the mass computed increases, then it is likely that the centre of the halo is toward the direction of displacement, since the halo have a spherical distribution of the mass with density peaked in their centre. The procedure is repeated until the mass variation is below a certain threshold value.

Once the halo centre is determined in a robust way, the actual computation of the radial density profile can be accomplished. This task is performed by a code I wrote, which takes as input the centre of the halo and the list of the positions of the particles belonging to the halo. The code computes the spherically-averaged density by sampling the particles inside a spherical shell. The thickness of the shell is computed, provided (in input) the minimum and the maximum value of the radius (r_{min} and r_{max} respectively) and the number of bins (*i.e.* the number of spherical shells used to slice the total halo volume), for the i-th slice as

$$\Delta r_i = \exp\left\{\frac{r_{max} - r_{min}}{N_{bins}} \cdot i\right\} \ . \tag{4.21}$$

The need of a minimum value of the radius is justified because the most inner regions of the halo have a very noisy density profile since the radius is comparable with the simulation's resolution (*i.e.* the ratio between the box side and the cubic root of the total particles number).
On one hand, the thinner the slices, the more precise the final profile is. On the other hand, due to the finiteness of the number of sample particles, the thinner the slices, the greater the statistical errors are, and thus the final profile becomes "noisy", since a small number of particles reside inside the shell and thus the deviations from their mean value are greater.
The spherically-averaged density is estimated through a finite number of values computed as

$$\rho_i = \frac{M(r_i) - M(r_{i-1})}{V(r_i) - V(r_{i-1})} = \frac{M(r_i) - M(r_{i-1})}{\frac{4\pi}{3}(r_i^3 - r_{i-1}^3)} \ , \tag{4.22}$$

with $r_i = r_{min} + i\Delta r/2$ and $M(r)$ and $V(r)$ being the mass and the volume within a sphere of radius r centred in the halo centre, respectively.

4.2 N-body simulations

In N-body simulations the system of interest is studied by means of a number of sample particles (this is the so-called "Monte-Carlo" approach), whose properties simulate the ones of the components of the system under study. In the case of cosmological simulations, each sample particle represents a mass element of the cosmological fluid or, more specifically, a mass element of a specific component of the cosmological fluid. However, it is not bound to correspond to a real physical system.
Since there is a gravitational interaction between the particles involved, the simulation of

the system is a N-body problem, thus the computational effort of performing a simulations scales as $O(N^2)$. Therefore, a number of different optimizations have been developed in order to reduce the computational cost for large values of N.

4.2.1 Algorithms for N-body simulations

In order to perform a cosmological simulation two main physical ingredients are needed: the gravitational force computation between particle pairs and the hydrodynamic of the particles, which are mainly a result of the microphysical (*i.e.* non-gravitational) interactions. The former is the most developed and simulations with only gravitational forces can be performed self-consistently with high resolution.
In this Thesis the simulations are performed using Dark Matter particles only, since the baryonic effects can be neglected as explained in Section 3.3. The Dark Matter interacts only via gravitational interactions, thus the hydrodynamics is not required, as it can be shown computing the relaxation time, *i.e.* the time needed to a particle in order to get significantly perturbed by the interaction with another particle, which can be estimated calculating the time after which the particle velocity has changed by a quantity of order itself. It can be shown (*e.g.* in [75]) to be:

$$t_{relax} \approx \frac{N}{8 \ln N} t_{cross} \tag{4.23}$$

where N is the number of objects within the structure under investigation and t_{cross} is the time needed to cross the structure. For a gravitationally-driven particle, the latter can be approximated by

$$t_{cross} \approx \frac{R}{v} = R\sqrt{\frac{R}{GNm}} \tag{4.24}$$

with R is the structure spatial extension, v the velocity of the particle, G the Newtonian gravity constant and m the (mean) mass of the involved objects. Hence, for a typical galaxy the Dark Matter particles (assumed as WIMP particles with mass $m = 100 MeV/c^2$) are $N \approx 10^{77}$, which gives

$$t_{cross} \approx \frac{1}{10 H_0} \tag{4.25}$$

$$\Rightarrow t_{relax} \approx \frac{10^{75}}{H_0} \tag{4.26}$$

showing that the Dark Matter matter can be trustfully treated as a collisionless system, since the simulation time ($t_{sim} \approx {}^1/_{H_0}$) is far smaller than the relaxation time of the system.
Under this assumption, the particles do not scatter each other but only respond to the global gravitational field, and thus in the Monte-Carlo approach this equations reduces to

a particle dynamics described by

$$\ddot{\vec{x}}_i = -\nabla_i \Phi(\vec{x}_i) \tag{4.27}$$

$$\Phi(\vec{x}_i) = -G \sum_{j \neq i} \frac{m_j}{\sqrt{(\vec{x}_i - \vec{x}_j)^2 + \epsilon^2}} \tag{4.28}$$

In the above equation it appears the smoothing length ϵ, which is a parameter introduced in order to accomplish a series of optimization tasks, related to the divergence of the computed gravitational force between two particles which come too close. The latter situation can lead to a fictional hard scattering between particles, which must not occur since they are only trace particles of an underlying density field (see *e.g.* [76]). Furthermore, it allows to use low-order integration schemes[3] when solving the equations of motion of the system. This parameter has to be chosen carefully, in order not to introduce unphysical effects which might affect the simulation, *i.e.* the different behaviour of the particles with respect to a real gravitational interaction should be under the simulation resolution. In particular, a suitable choice is

$$\epsilon = \frac{d}{\eta} \tag{4.29}$$

with d being the mean distance between the particles in the simulation box and η being a number between 30 and 50.

In order to take into account the expansion of the Universe, the cosmological codes use comoving coordinates $\vec{x}_i$. Thus, the Hamiltonian of the system becomes

$$H = \sum_i \frac{\vec{p}_i^2}{2 m_i a(t)^2} + \sum_j \sum_{i>j} \frac{m_i m_j \phi(\vec{x}_i - \vec{x}_j)}{a(t)} \tag{4.30}$$

where $\vec{p}_i = a(t)^2 m_i \dot{\vec{x}}_i$ are the canonical conjugated momenta, $a(t)$ is the scale factor of the expanding background Universe, assumed as a Friedman one, and $\phi(\vec{x})$ is the interaction potential. The latter sum on the right-hand-side of the above equation runs over $i > j$ in order not to count twice times each particles pairs.

During the dynamic evolution of the system it can happen that the particles cross the simulation box boundaries. In order to avoid particle loss due to this fact, an infinite potential barrier could be put at the box boundaries, but this interferes with the particle dynamics since it introduces unphysical barriers. Moreover, even without the potential barriers, the particles near the boundaries would be in a physically unlikely situation, with a very higher concentration of particles on one side and almost any particles on the other. Thus, the commonly adopted solution is to use periodic boundary condition, *i.e.* the

[3] For a given integration scheme, *i.e.* a procedure which allows to solve differential equations in an approximate way, the order of the method is defined by its asymptotic behaviour when the discretization step h of the independent variable goes to zero. In particular, for an algorithm of order p the difference between the analytical solution and the approximated one is $\delta = O(h^{p+1})$. In general, a higher order method requires a more complicated algorithm, which thus requires a higher computational cost.

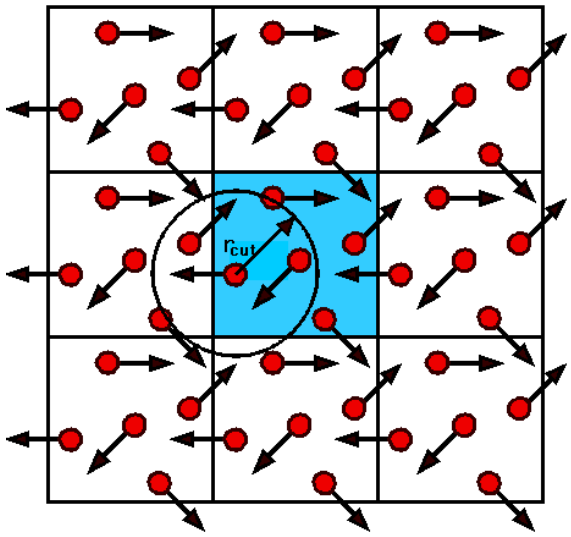

Figure 4.2: A schematic representation of the Periodic Boundary Condition in particles dynamic simulations. The Figure is taken from http://www.ucl.ac.uk/~ucfbasc/Theory/pbc-mi.html.

simulation box is replicated an infinite number of times in every direction (see Figure 4.2). The interactions for a given particle are computed with the nearest copy of every other particle; this is known as the "minimum image convention". As an example, using this approach the distance between a particle i and the nearest image of another particle j is given by:

$$(\vec{r}_{ij})_{nearest} = (\vec{r}_i - \vec{r}_j) - L \cdot Nint[(\vec{r}_i - \vec{r}_j)/L] \tag{4.31}$$

where L is the simulation box size and $Nint$ is the *nearest integer* function.
The net effect of the convention described is that, whenever a particle cross a border of the simulation box, it re-enter the simulation box, *i.e.* one of its copies enter the simulation box, through the opposite side.
It is important to notice that, due to the fact that the force is computed, in some cases, between a particle and an image instead of two particles, the angular momentum is not guaranteed to be conserved.

Numerical Integration

Turning back to the dynamic evolution of the system, the simulation codes need to integrate the differential equation 4.27, which can be written as[4]

$$\dot{y} = f(y) \tag{4.32}$$

This is typically done by approximating the solution with a series of values $\mathrm{y_i}(t_i)$, separated by a time-step Δt_i (in principle different for each step), which can be computed in a number of different ways. As an example, the implicit (explicit) Euler method approximates the y_i values using the first derivative in the last computed (current) point, *i.e.* $\dot{y}(y_{i-1}) = f(y_{i-1})$ ($\dot{y}(y_i) = f(y_i)$); however, this is only first-order accurate, meaning that its error grows rapidly with time. Other methods are the "mid-point rule" method and the Runge-Kutta method.

The most used method is the so-called "Leapfrog". The latter is described in Appendix B.

Gravity Forces Evaluation

Since a direct summation of the forces acting upon a particle requires a computational effort scaling with N^2, an approximate calculation method is usually employed. This is acceptable provided that the errors introduced by the approximate calculation are random and not systematic.
Two main approaches to the approximate forces evaluation exist: the Particle Mesh method and the Tree algorithm, which will be now described.

[4] setting: $y = \begin{pmatrix} \dot{x} \\ -\nabla_i \Phi(\vec{x}_i) \end{pmatrix}$

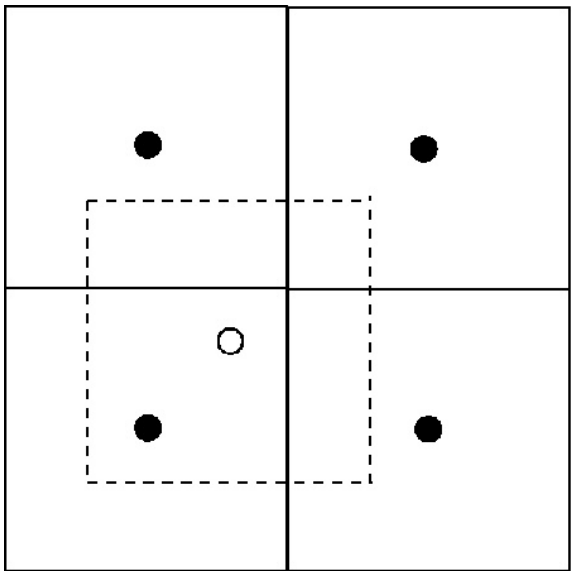

Figure 4.3: A schematic representation of the Cloud-in-Cell assignment scheme. The black circles represent the mesh nodes, while the white one represents a particle. The Figure is taken from http://homepage.univie.ac.at/franz.vesely/simsp/dx/node48.html.

As an example, in the Particle Mesh method the potential is computed on the nodes of a Cartesian grid that covers all the simulation volume. The latter is divided in M^3 cubes and the grid nodes are the centres of each cube. Thus, also the mesh is cubic. To each node a mass that represents the particles inside the cube is assigned. The simplest way to assign the mass of each particle to a mesh node is to assign the total mass to the nearest node. However, more sophisticated method exists, such as the Cloud-in-Cell assignment, where the particle's mass is distributed in a cube of the same size as the mesh cubes but centred on the particle, then its mass is assigned to each cubes in proportion to the superposition between the two cubes. A 2D example is shown in Figure 4.3. Furthermore, the particle mass can be distributed following a certain function, in order to give a greater importance to the nodes that are closer to the particles (*e.g.* spline assignment).
Then, the potential Φ is computed on the mesh nodes, and then the potential for the particles is reconstructed using an interpolation kernel.
Despite of the simplicity and velocity of this approach, it suffers from a serious problem: since the force resolution is limited to the particle mesh size, it is not suitable for simulations with strong clustering as the cosmological ones. In order to use the particle mesh method one should set a mesh size small enough to resolve the internal structure of the clustered objects, but in this way the mesh grid is very fine and thus requires a large computational effort.
A partial solution of this problem is given by the so-called AP^3M (*i.e.* Adaptive Particle-Particle Particle-Mesh) algorithm, where a refined mesh is placed near the clustered regions and the force between near particles is computed by direct summation.

An alternative approach is the one provided by the Tree algorithms. The basic idea is to divide the simulation box in cubic cells so that the gravitational attraction between particles inside the same cell can be computed by direct summation, while the gravitational forces that involve particles in different cells is computed as the force acting between the particle considered (*i.e.* the one I want to compute the force on) and the center of mass of the cell the other particle belongs to. The first improvement to this basic idea is to produce a mesh that has larger cell where the particles density is lower and smaller cubes when the particles are denser.
To be more specific, the code described here build a "tree" by dividing the entire simulation box in eight cubes, each one of side equal to half the simulation box side. Once it has been done, the code repeats the same procedure for every cube obtained in the previous step until every cell contains only one (or zero) particles. When the forces have to be computed, the "tree" is walked down and, at every level, an opening criterion decides if considering the cube as a single particle is a good approximation. This typically happens when the particle on which the force is being computed is sufficiently distant from the cube and the latter is sufficiently small. If this is the case, the force is computed using the center of mass of the cube, if not it is "opened", *i.e.* the smaller sub-cells are considered individually. The opening criterion used is such that the cell is "opened" if

$$\frac{GM}{r^2}\frac{l^2}{r^2} \leq \alpha|\vec{a}| \tag{4.33}$$

where M is the mass of the node, l its extension, r is the distance between the node center and the particle, $\vec{a}$ is the total acceleration computed in the last time step and α a parameter that can be set.
Using the Tree method, the computational effort is reduced to $N \log N$. Moreover, this algorithm is suitable for all the clustering states since its speed depends weakly on the level of clustering. On the other hand, it is more difficult to adapt this algorithm to individual timesteps.

The two methods described above can be combined in what is called the TreePM method, where the potential felt by a single particle is split in a long-range and a short-range part. Then, the former is computed using a PM algorithm, while the latter is computed using a Tree method. To be more precise, the Poisson equation for the potential reads

$$\nabla^2\Phi(\vec{x}) = 4\pi G(\rho(\vec{x} - \bar{\rho}) = 4\pi G\left(\sum_i m_i\delta(\vec{x} - \vec{x}_i) - \frac{M_{TOT}}{L^3}\right) \tag{4.34}$$

where the term in parenthesis represents the deviation from the mean density. Recasting this equation in the Fourier space, it reads

$$\Phi_{\vec{k}} = \frac{4\pi G}{\vec{k}^2}\rho_{\vec{k}} \tag{4.35}$$

Thus, the long range part is given by:

$$\Phi_{\vec{k}}^{long} = \Phi_{\vec{k}}e^{-\vec{k}^2 r_s} \tag{4.36}$$

where r_s is a suitable transition scale. This contribution to the total force is computed through a PM algorithm, using a Cloud-in-Cell mass assignment in real space; then the computation of the potential is done in the Fourier space and after another Fourier transform the force is computed using finite differences as an approximation for the derivative and through an interpolation procedure among the mesh nodes.
The short range part reads:

$$\Phi_{\vec{k}}^{short} = \Phi_{\vec{k}}(1 - e^{-\vec{k}^2 r_s}) \tag{4.37}$$

It is evaluated in real space with a Tree algorithm.

Smooth Particle Hydrodynamics

The SPH is a procedure used to compute the dynamics of a fluid. The fluid is divided in discrete elements and each one of them collects the properties of the portion of fluid assigned to it. The continuous properties of the fluid are reconstructed using an interpolation function. The density of each element is computed using a softening kernel with an *adaptive smoothing length* (h) defined in such a way that it contains a constant mass (*i.e.* obeying the equation $^{4\pi}/_{3}h^3\rho = N_{SPH}\bar{m}$, where N_{SPH} is the typical number of neighbour and $\bar{m}$ is the average particle mass).

As a final note, a significant improvement in the code speed is given by parallelization, *i.e.* distributing the work between a number of different processors. A commonly used approach in cosmological simulation, where the number of sample particles is typically high, is to decompose the simulation box into a number of subdomains and assign each one of them to a different processor.

4.2.2 The GADGET code

The code used in the simulations presented in this Thesis is the widely-used cosmological massively parallel N-body code GADGET. In particular, a modified version (in order to take into account the model studied in this Thesis, described in Section 3.3) of the GADGET-3[39][40] version[5] called C-GADGET has been used.
GADGET is an N-body code created for cosmological and Smooth Particle Hydrodynamics (SPH) simulations. The main structure of the code is a Tree (or TreeSPH, depending on the user's choice) algorithm and a number of further physical processes are implemented, such as effects of photoionization, star formation, ionized gas thermal conduction and supermassive black hole formation.
The GADGET-2 code is available under the GPU General Public Licence (GPL), thus the source code is freely available and every derived product must be redistributed under

[5] which is not public at the moment I'm writing, so [39] and [40] refer to the version GADGET-2 and GADGET, respectively.

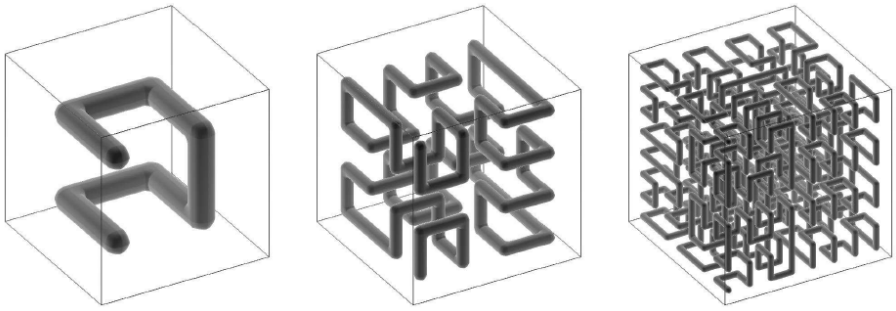

Figure 4.4: The 3D Peano-Hilbert space-filling curve. The Figure is taken from [39].

the same licence. The code was originally developed by Volker Springel (see [79]).

GADGET uses by default a Tree algorithm, but it can be forced to use a TreePM algorithm. The details of such algorithms were described in 4.2.1. However, it is worth to describe the parallelization technique employed. The domain decomposition of the simulation box is performed using the 3D Peano-Hilbert space-filling curve (shown in Figure 4.4). Once the simulation box is filled, *i.e.* each particle is assigned to a point of the curve, it is divided in a number of pieces equal to the number of processor and a each of them is assigned to a different CPU. This procedure is reliable since the Peano-Hilbert curve has the property of mapping near points in near positions along the curve, *i.e.* points close on the 1D Peano-Hilbert curve are also close in 3D space. In addition, each processor constructs also a global top-level tree where all the higher level nodes are stored, in order to supply information whenever the processor needs information about particles assigned to a different CPU (which is in general distant from the particle considered and, then, top-level information is sufficient).
Along with the parallelization of the simulation box, also the Fourier transforms are parallelized using the parallel version of the FFTW library [78]. An alternative approach in which each processor determines the particles needed by the others in order to compute the Fourier transform and send the data to the right processor is also implemented.
Furthermore, the operation of input and output (I/O) are also parallelized, *i.e.* the code offers the possibility to write a simulation snapshot in different files at the same time, and in the same way it offers the possibility to read initial conditions spread among different files.
Finally, GADGET features six different particle types, which can be set to behave differently in order to allow a wider representation of the simulated physical system, which could be composed by different types of particles.

The code has been tested in a number of different scenarios, ranging from pure Dark Matter to pure Hydrodynamical system. An extensive description of them can be found in [39]. Moreover, in Appendix C some informations additional details about the GADGET code are described, *e.g.* the performance analysis and the available input parameters.

4.2.3 Initial Conditions

The first step to run a cosmological numerical simulation is to create a suitable set of initial conditions. The basic idea is to start from a realization through sample particles of an isotropic and homogeneous Universe (sometimes dubbed "pre-initial" conditions), and then modify the obtained realization in order to match its power spectrum with the one corresponding to the desired cosmological model to simulate at high redshifts.
Since the CMB shows temperature fluctuations of order $\delta T/\langle T\rangle \approx 10^{-5}$, the linear theory for the perturbations can be used to reconstruct the "original" particles positions, *i.e.* the particles positions (and other properties) at a given high redshift used as starting point for the simulation.

In order to impose the power spectrum in the particles distribution, each particle must be displaced by a given quantity from its initial position (which corresponds to a homogeneous distribution). The displacement is usually computed relying on the Zel'dovich approximation [42]. Since the redshift of the initial conditions is sufficiently high in order to ensure that all the modes represented in the simulation box are still in the deeply linear regime, the particles positions can be obtained form a homogeneous distribution by solving the linear regime equations. The latter, once solved provide a growing solution, *i.e.* a solution which describes a growing perturbation, and a decaying one, *i.e.* describing the decrease of the perturbation. Since the decaying solution rapidly vanishes, they can be safely ignored when interested in the low-redshift features, and hence the temporal evolution of the power spectrum is driven by the total grow factor $D(t)$, *i.e.* the growing solution to equation 2.19:

$$P(k) = P_0(k)D^2(t) \tag{4.38}$$

As an example, for a ΛCDM cosmology the factor $D(t)$ is given by

$$D(a) = \frac{5}{2}\Omega_m H_0^2 H(a) \int_0^a \frac{\mathrm{d}a'}{\dot{a}'^3} \tag{4.39}$$

with $H(a) = H_0\sqrt{\Omega_m/a^3 + \Omega_\Lambda + \Omega_k/a^2}$.
The particles displacements can be computed considering the growing mode in the real space (which usually involves a Fourier transform, since it is usually computed in the Fourier space through equation 2.19), and numerically integrating in time the equation down to the time of the initial conditions, which gives a finite displacement

$$\delta\vec{x} = D(t)S(\vec{x}) \tag{4.40}$$

The quantity $S(\vec{x})$ can be determined combining the derivative of the ansatz 4.40 with the linear perturbation equation in comoving coordinates 2.17. The result reads

$$S(\vec{x}) = -\nabla\Psi(\vec{x}) \tag{4.41}$$

where Ψ in Fourier space is

$$\Psi(k) = \delta_0(k)\frac{1}{k^2} = \sqrt{P_0(k)}R_{\vec{k}}e^{i\phi_{\vec{k}}} \tag{4.42}$$

The term $R_{\vec{k}}e^{i\phi_{\vec{k}}}$ is due to the fact that $P_0(k) = \langle|\delta(\vec{k})|^2\rangle$ and thus the power spectrum does not provide any information about the phase of $\delta_0(k)$, which has to be added manually by sampling a pair of Gaussian-distributed random numbers R_1 and R_2:

$$R_{\vec{k}}e^{i\phi_{\vec{k}}} = R_1 + iR_2 \tag{4.43}$$

Thus, in order to produce a set of suitable initial conditions, the original homogeneously-distributed particles are displaced following the power spectrum by means of a random number realization. The velocity can be straightforwardly computed as the derivative of equation 4.40.
It is important to note that, since the initial conditions production implies a random number realization, from the same "pre-initial" conditions different results could be obtained. Thus, using of the same seed for the random number production is important in order to obtain comparable initial conditions, and thus comparable simulations, starting from the same "pre-initial" conditions.

The original homogeneous particles distribution has not been specified yet, since there are two different possibilities: the grid and the glass distributions. The former consists in placing the particles in the nodes of a cubic equally-spaced Cartesian grid, while the latter provides a particles distribution homogeneous and isotropic but without a constant distance between the particles (see [80]). The glass file at a given redshift z_{glass} can be obtained placing the particles at random positions into the simulation box and taking them as the $z = 0$ distribution and thus the particles are evolved back in time until z_{glass} is reached. In an analogous way, the glass file can be obtained using the random particles distribution and evolving it forward in time with a gravity force with reversed sign.
Both methods provide "pre-initial" conditions with particles in unstable equilibrium with zero gravitational force acting on each particle. In the simulations run for this Thesis, a glass file was used to produce the initial conditions.
The initial conditions used in this Thesis were produced using the N-GenIC code [41], modified in order to take into account the presence of two types of Dark Matter particles as in the model studied.

4.2.4 Simulations of non-standard Cosmologies

The GADGET code described in Section 4.2.2 is developed for cosmological simulations within the standard ΛCDM cosmology. Thus, in order to investigate other non-standard cosmologies the code must be modified to take into account the new interactions and/or the new hypothesised particles. An extensive description of the modifications necessary can be found in [6]. This new version of the code is called C-GADGET and is not yet publicly available.

The first effect that must be taken into account is the modified expansion history as a consequence of the presence of the ϕMDE (see Section 3.3). In particular, the Hubble function $H(z)$ is modified. Thus, the Hubble function computation performed by GADGET-2 has been substituted with a modified Hubble function for the studied model. In order to easily

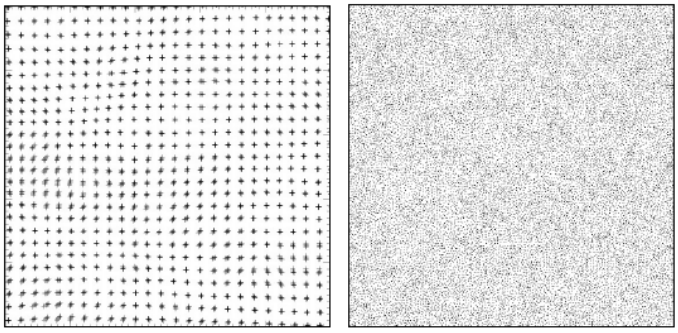

Figure 4.5: Initial conditions obtained for a Cartesian grid distribution (left panel) and a glass distribution (right panel). The apparent different number of particles is due to a projection effect: once the Cartesian grid is projected on a plane, the particles aligned in the projected direction overlap, and thus only one of them is visible, while in a glass file almost all the particles are visible once projected. The Figure is taken from http://popia.ft.uam.es/aknebe/page3/files/ComputationalCosmology/05ICs.pdf.

manage the change in the Hubble function for different models, this is read from tabulated values written in a file that can be set as input. The values needed at each timestep of the simulation are computed using an interpolation technique between the tabulated values. The same file must specify also the values for a number of other relevant quantities: the global variation of the gravitational constant (in order to allow simulations of modified gravity), the coupling functions for baryons and Dark Matter, the mass corrections for baryons and Dark Matter, and the kinetic energy density for the scalar field. In fact, as shown by equation 3.29, as a consequence of the coupling between the Dark Matter particles and the scalar field ϕ, the mass of the particles is expected to change in time. Thus, their density does not scale as a^{-3} but must be corrected with the term arising from their mass variation that takes the form

$$\Delta m_x(a) = e^{-\int_a^1 \beta_x(\phi)\frac{\mathrm{d}\phi}{\mathrm{d}a}\mathrm{d}a} \tag{4.44}$$

Furthermore, the McDE model features an extra velocity-dependent term in the Euler equation, *i.e.* the second term in the parenthesis in the following equation:

$$\frac{\mathrm{d}\vec{v}}{\mathrm{d}\tau} = -H\left[1 - \frac{\beta(\phi)\dot{\phi}}{MH}\right]\vec{v} - \nabla\frac{G[1+2\beta^2(\phi)]M}{r} \tag{4.45}$$

In the standard GADGET implementation the velocity-dependent term in the standard Euler equation (*i.e.* the first term in equation 4.45) is not computed since the variables choice is such that this term vanishes. In fact, GADGET-2 uses the variable

$$\vec{p} \equiv a^2(t)\vec{v} \;\Rightarrow\; \frac{\mathrm{d}\vec{v}}{\mathrm{d}t} = \frac{1}{a(t)}\frac{\mathrm{d}\vec{p}}{\mathrm{d}t} - \frac{H(t)}{a(t)}\vec{p} \tag{4.46}$$

Introducing the above relation in the equation 4.45, the following equation is obtained:

$$\frac{\mathrm{d}\vec{p}_i}{\mathrm{d}t} = \frac{1}{a}\left[\frac{\beta(\phi)\dot{\phi}}{M}a(t)\vec{p}_i + \sum_{i\neq j}\frac{[1+2\beta_i(\phi)\beta_j(\phi)]m_j\vec{x}_{ij}}{|\vec{x}_{ij}|}\right] \tag{4.47}$$

where $\vec{x}_{ij}$ is the relative positions of the particle i and j.
The above equation shows that if no coupling is present there are no $\vec{p}$-dependent terms, while in the case of a non-vanishing coupling at least for one species of particles, an extra term arises and must be included in the code. The additional term represent a purely cosmological drag, since it does not depend on the matter distribution of the other particles.

The main modification that the code needs is obviously the implementation of the fifth force. This can be obtained with a substitution of the Newton gravitational constant:

$$G_N \longrightarrow G_{l,m} \equiv G_N(1+2\beta_l\beta_m) \tag{4.48}$$

where l, m denote a pair of particles. In particular, in the McDE model the coupling values are different for different particle species, thus species-dependent couplings must

be implemented. As explained in Section 4.2.2, the gravitational force calculation is made using a hybrid TreePM algorithm, and hence both the Tree and PM parts must be modified. In particular, in the Tree part of the algorithm it is no longer sufficient that each node carries the information about its total mass and center of mass position, but it must provide also information about the total mass and center of mass position and velocity for each particle type. In the PM part of the algorithm, the force computation in the Fourier space can not be made for all the particles at the same time anymore, but it must be repeated for each particle type, since they have different couplings, and the total force is then computed as a sum of the forces due to the different species.
Furthermore, in order to take into account the presence of two different species of Dark Matter particles also the procedure for the production of the initial conditions must be modified. The procedure described in Section 4.2.3 has been slightly modified. In particular, after the particles are displaced accordingly to the power spectrum of the model with amplitude rescaled through the global growth factor $D(z)$ to the desired redshift, each particle is split into two particles with a mass ratio equal to the desired relative abundance of the two Dark Matter species. Then, the computed displacement for the original particles is applied to the particle pair following the relative amplitude of the perturbations in opposite randomly chosen direction. In such a way, no preferred directions is introduced in the system by the procedure.

4.2.5 Zoomed Simulations

In order to study in detail a single collapsed structure, a high resolution (*i.e.* a high number of particles per volume unit) is required. On the other hand increasing the total number of particles leads to a higher computational cost. A suitable approach is to use the so-called zoomed simulations, *i.e.* simulations with a higher particles density only in the region of interest. In such a way a high precision can be reached for the object under investigation without a sharp increase in the required computational effort.
Obviously the greater precision must not modify the system behaviour. As an example, when increasing the number of particles in a given region, their masses have to be rescaled in order not to modify the total mass within the region.

Although very efficient, this approach suffers from a number of problems, mainly due to the mixing of high-resolution and low-resolution particles which occurs during the system evolution. In particular, the particles of given resolution which enter a region of different resolution are called "intruders". For this reason usually the high-resolution region is encapsulated in a mid-resolution region, which has the task of softening the effect of the heavy low-resolution particles. Despite of its presence some mixing still occurs near the boundaries. Thus the high-resolution region should cover a wider portion of space with respect to the system of interest.

With the aim of performing a series of zoomed numerical simulation, I developed a code which reads in input the output of a numerical simulation and trace back the particles of interest (*i.e.* the ones to be studied with high resolution) in order to produce a set of

zoomed initial conditions suitable to be used in a numerical simulation. The code, called "ZInCo" (contraction of Zoomed Initial Conditions), is widely described in Chapter 5.

4.3 Codes

During the whole work presented in this Thesis, I have developed a number of different codes, mainly small codes for data analysis. They are briefly presented here in order to give a comprehensive, compact and concise illustration of all the codes developed.

The main code, which represents one of the cores of the Thesis, is the code named "ZInCo", which has been developed in order to produce a set of initial conditions compatibles with the GADGET3 simulation code and featuring three regions of different resolution. The code process a snapshot of the low-resolution simulation, compute the different resolution regions, trace back their particles to the initial conditions and produce the zoomed initial conditions. The code is widely described in Chapter 5.

In order to analyse the evolution of a specific structure in the simulation box during the whole simulation, I wrote a simple code which, once given the IDs of the particles it has to follow, reads all the snapshot produced by a simulation (or at least a subset of them given in input) and produce a series of density plot. The code can be set to produce, for every snapshot, a number of plot featuring different zoom (*i.e.* different magnification of the region of interest) and/or resolution (*i.e.* the resolution of the resulting picture).

The density profiles (described in Section 4.1.3 and showed in Section 7.2) has been computed using a code I wrote. The code simply reads in input the snapshot of the simulation and a number of parameters: the centre of the halo, the minimum and maximum radius (R_{min} and R_{max} respectively) of the profile.
The code build a number of spherical shells with radius exponentially increasing from the centre, *i.e.*

$$R_i = R_{min} e^{\Delta R \cdot i}$$

where

$$\Delta R = \frac{R_{max}/R_{min}}{N_{bin}}$$

with N_{bin} being the total number of shells between the minimum and maximum radius. Then, the snapshot is read and the each particle is assigned to the correspondent bin. Finally, the mass of every bin is divided by the volume of the shell and the obtained density is normalized with respect to the global mean density, computed as the ratio between the total mass and the simulation box's volume. The code allows to select only a particular type of particle to process.

Finally, I wrote a code which computes the Halo Mass Function (see 4.9) simply binning the friends-of-friends halo provided by the GADGET code in function of their mass and printing a suitable output.

Chapter 5

The ZInCo code

5.1 Producing the zoomed Initial Conditions

The approach I choose for producing the zoomed initial conditions consists in starting from very high resolution initial conditions and "dilute" them outside the region of interest. This procedure ensures that in the high-resolution region the particle positions are exactly the ones computed from the original high-resolution realisation. Moreover, this approach is somewhat backward compatible, since it can be applied also to already existing initial conditions. On the other hand, producing new initial conditions directly with different resolution regions would have meant that the existing simulations could not be processed unless having a trustful way to exactly reproduce their initial conditions.

The zoomed initial conditions used in this Thesis have been produced by a code I wrote, called ZInCo (a simple acronym which stands for "Zoomed Initial Conditions"). The code's basic principles are straightforward: the entire simulation box is "cut" in smaller cubes and each one of them is processed separately. Whenever the cube considered overlaps with the high resolution region, its particles are copied into the new (zoomed) initial conditions, otherwise the code averages over a number of surrounding cubes, *i.e.* a number of cubes are gathered together in order to produce a bigger cube. The mid- and low-resolution regions differ for the number of cubes which are joined together. When averaging over the particles, the code processes one particle type at a time, in order not to mix different particle types. The resulting particles are then written in a series of files.
Since a common way of proceeding in cosmological zoomed simulations is to run first a simulation with low resolution on the full simulation box, the code provides a function called "dilution" which uniformly reduces the resolution on the entire box. From now on, 'dilution' will refer to this behaviour, while 'zoom' will refer to the procedure described above. The differences between these two behaviours are shown in Figure 5.1, where a slice of the initial conditions box is shown: in the upper panel the original initial conditions are shown, in the middle one the result of their dilution is displayed, while in the bottom one the result of a zoom centred somewhere near the center of the box is plotted.
Once the low-resolution simulation ends, its output is analysed in order to identify one or

more objects of interest and, thus, a new simulation zoomed around it/them is performed. In order to accomplish such a task the code provides the possibility (which is the default behaviour) to specify the different regions directly in the low-resolution output (*i.e.* its snapshot at $z = 0$). The code will take care of tracing back the particles in the different regions to the low-resolution initial conditions, identifying the corresponding region in the high-resolution initial conditions and then produce the new zoomed initial condition files.

The ZInCo code is among the first codes capable to process different particle types producing different levels of resolution for each of them. Although a number of different codes able to produce initial conditions with different levels of resolution are publicly available, it is unusual to find a multi-scale cosmological initial conditions code able to process different particle types.
This unique feature of the code is due to the fact that, instead of producing multi-resolution initial conditions from scratch, the ZInCo code uses already produced initial conditions. The latter can be produced featuring any particle types desired and require no further complication in the zooming procedure.
Thus, the ZInCo code provides both a simple and powerful tool for producing initial conditions which can be used for a large number of conceptually-different cosmological simulations. An example of such applications are the numerical simulations presented in this Thesis, but a series of further applications could be easily imagined, *e.g.* simulations with both cold and warm Dark Matter, or both Dark Matter and neutrinos.

The above summary of the code's behaviour points out that for the low- and mid-resolution regions only one particle (for each type) is produced for every group of cubes joined together. Thus, the number of cubes obtained from the slicing of the simulation box is related with the final resolution of the non-high-resolution regions. This number can be specified in input using the *cubes_per_side* parameter, since the simulation box is cubic.
Also, note that the different regions are ideally spherical, and this property can not be changed by the user. This allows to specify the different regions by means of their centre (which must be the same for every region, as a consequence of the fact that the mid-resolution region is just a buffer between the other two) and their radius.

5.2 Details of the code

The first step of the ZInCo code is to initialize the parallel environment and to read the inputs from a parameter file. For a detailed description of the parameters that must be supplied in input, see Appendix A. Since the code is parallel, in order to work, it requires a Message Passing Interface (MPI) implementation, like the one provided by MPICH [81] or OpenMPI [82].

Following the default behaviour of the code, the regions defined in input for the snapshot file must be "translated" into regions for the initial conditions. To this end the snapshot files are read and the IDs of the particles within the high-resolution region are stored, in

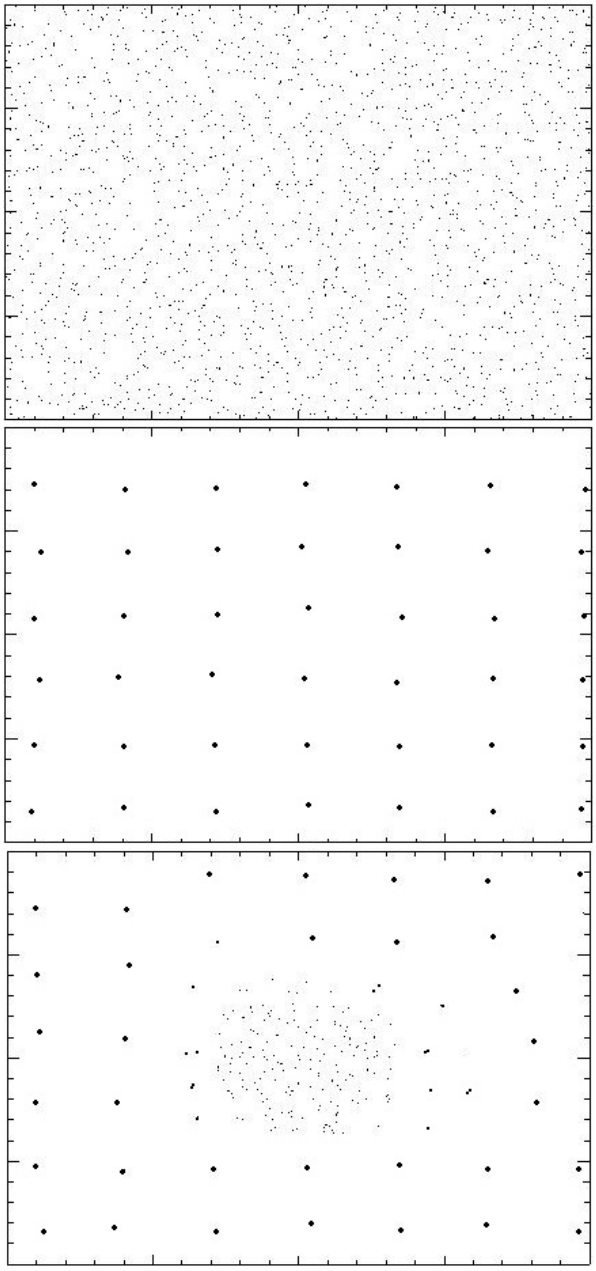

Figure 5.1: Example of the zoom procedure: the first image shows a slice of the original high-resolution ICs, the second one shows the homogeneous dilution of the former and the third shows the different dilution in different zones around the halo's center.

order to trace them back to their original positions in the initial conditions.
Afterwards, the low-resolution initial conditions are read and the IDs compared to the ones previously stored in order to identify the particles of the high-resolution region. Once they have been identified, the centre of the new high-resolution region is computed as

$$x_C = 0.5 \cdot [max_i(x_i^H) - min_i(x_i^H)] \tag{5.1}$$

where the index i runs on all the particles of the high-resolution region, and similarly for the y and z coordinates, whilst the radius of the high-resolution region is computed as

$$r_H = \sqrt{max_i[(x_i^H - x_C)^2 + (y_i^H - y_C)^2 + (z_i^H - z_C)^2]} \tag{5.2}$$

i.e. the sphere of minimum radius that contains all these particles. The mid-resolution region is computed in such a way to achieve the ratio r_M/r_H that is specified by the user in the parameter file.

Once this is done, the high-resolution initial conditions can be produced. The sub-cubes are browsed and each one of them is labeled depending upon which region it belongs to, *i.e.* the so-called *resolution matrix* is created. In such a way, whenever a portion of the code must identify which region a cube belongs to, there is no need to compute again the distance from the centre of the high-resolution region but it is sufficient to read the element associated in the resolution matrix.
Called r the distance between the centre of the considered cube and the centre of the high resolution region, r_H the radius of the high resolution region and r_M the radius of the medium resolution region, the code decides the action to perform as follows:

- if $r < r_H + k$ the particles should be directly copied in the zoomed initial conditions, with no additional operations;
- if $r_H + k < r < r_M + k$ the code averages over a number sm of surrounding cubes, as specified in the parameter file;
- if $r > r_M$ the code averages over a number sl of surrounding cubes (where normally $sl > sm$).

In the above equations, k is half the cube's diagonal. The k term is added in order to ensure that no high-resolution particles could lie outside the high-resolution region. This could lead to treat as high-resolution some cubes that lie completely outside the high-resolution regions, but this helps solving the intruders problem described above. The number of cubes that have to be merged is determined by the two parameters sm (for the medium-resolution zone) and sl (for the low-resolution one), both provided in input. They set the side of a merged cubic region in units of the primary cells produced by the initial slicing process (see Figure 5.2 for a sample situation with sl=3).
The code browses the resolution matrix in order to compute what cubes have to be joined together. Each one of them is re-labeled with a number, which is equal for cubes of the same group and grows progressively for different groups. It also takes care of checking that

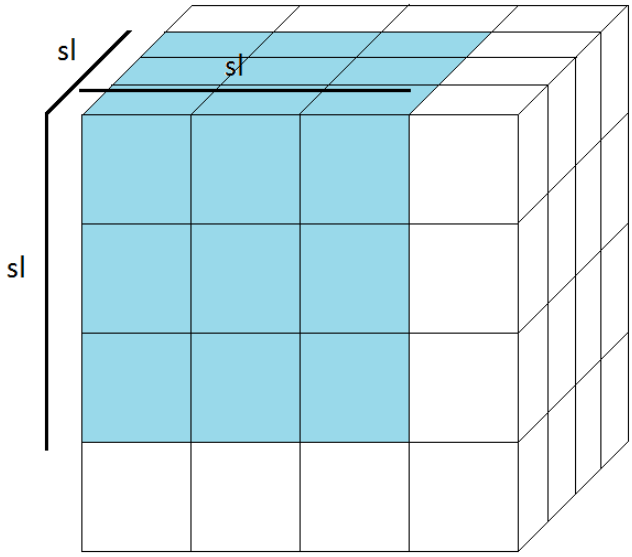

Figure 5.2: Schematic representation of how the parameter *sl* (and similarly *sm*) allows to choose the dilution factor in the low-resolution region.

all the cubes of a given region have been processed. It can happen that after the described procedure, some cubes remain and their geometrical distribution is such that they can not be joined together. In such cases, the code tries to join them in smaller groups, down to $1 \times 1 \times 1$ group, *i.e.* a single cube. This ensures that there are no unprocessed particles.

Afterwards, the code browses again the resolution matrix and copies the particles inside the high-resolution cubes or performs the average over cubes with the same label. As stated before, the average process is performed separately for each different particle types, thus the averaging process, for every group, a particle of each type with:

- position and velocity which are the position and velocity of the center of mass of the particles of the group
- mass which is the sum of the masses of the particles belonging to the group
- a new unique ID

These features underline how the *cubes_per_side* parameter, along with the *sm* and *sl* parameters, determines the final resolutions of the mid- and low-resolution regions. The code has also the option to save in a file the correspondence between the old IDs (*i.e.* the IDs of the particles in the original initial conditions) and the new IDs given to the group.

The new particles are then written in a series of output files, using the same format as the original ones; in such a way they are ready to be used in the simulations. An example of the procedure just described can be found in Figure 5.3.

The code prints the most important information on screen. They are also printed, along with a series of other information, on a log file in the output directory.
The code was developed for the specific task of testing the McDE model in the absence of baryons, and thus is written in order to handle only two types of particles. However, the code has been written such to be easily adjustable in order to handle a larger number of particle types. In particular, the code uses all the six particle types of GADGET: in the zoomed (or diluted) initial conditions type 0 and type 1 are the high-resolution particles, type 2 and type 3 are the mid-resolution particles and type 4 and type 5 are the low-resolution particles. This has been done in order to allow to employ different softening values for particles of different resolution.

Finally, I move to discuss the parallelization strategies adopted in the code. The code features a serial portion, which includes the computation of the high- and medium-resolution regions in the initial conditions starting from the ones in the snapshot provided and the construction of the resolution matrix. Whilst the former is really implemented in a serial way, *i.e.* a single processor computes the quantities and then broadcasts the values computed to the others, the latter is computed separately by each processor, in order to reduce the communication between processors, which turns out to be one of the main bottlenecks when running on a large number of cores. Since the algorithm applied to create

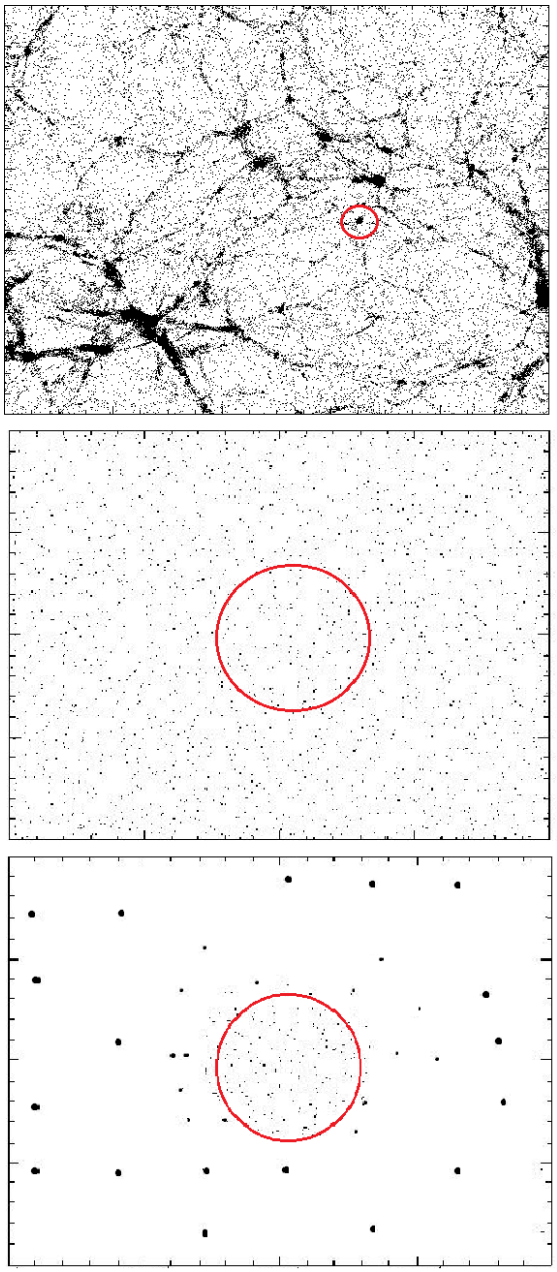

Figure 5.3: Example of the zoom procedure: the first image shows a slice of the snapshot at $z = 0$ obtained from a low-resolution simulation; once a halo of interest is selected (red circle), its particles are traced back to its ICs and the high-resolution region selected is adapted (the second image). Then the code produces the three regions with different resolution around the halo selected in the new (zoomed) ICs (third image).

the resolution matrix is the same and it does not contain any source of randomness, the resulting matrix is the same for each processor, and thus can be faithfully used in the code that follows.
The parallelization is implemented in the simplest way, *i.e.* assigning to each available processor a portion of the cubes to process. In particular, firstly a number of processors np_{high} is assigned to the high-resolution region, whilst the other $np_{mid+low}$ are assigned to the other regions. They are computed as:

$$\frac{np_{high}}{np_{mid+low}} = \frac{N_{high}}{N_{mid+low}} \tag{5.3}$$

where N_{high} and $N_{mid+low}$ are the number of particles in the high- and medium-resolution regions *predicted to be in the final zoomed initial conditions*. The former is simply the number of particles labelled as "to be copied", whilst the latter is equal to number of integer-labelled groups of cubes. Obviously the condition $np_{high} \geq 1$ holds true whenever $N_{high} > 0$, and similarly for $np_{mid+low}$.
Afterwards, within each of these two groups of processors, an equally-divided number of cubes (in the case of np_{high}) or cubes' groups (in the case of $np_{mid+low}$) are assigned to each processor, which proceeds to process them as explained above.
Once each cube has been processed, a single processor writes the output: after computing how many particles must be written in each file in order to match the desired number of output files, this master processor retrieves the needed information from all the other processors and then writes the individual output files.

The code requires a number of parameters that can be set in input, and also provides some compilation options which specify its behaviour. A list of the can be found in Appendix A.

5.3 Testing the zoomed initial conditions

In order to check if the new initial conditions are suitable to be used in the new zoomed simulations, they have to share with the original initial conditions the same power spectrum, since they must represent the same statistical realisation with different resolution. In particular, the power spectra are expected to differ only at small scales, where the shot noise (see below) becomes relevant: less particles in the same box means a greater mean particles separation, resulting in a greater shot noise, that hence modifies the power spectra at slightly larger scales.
An initial set of 2×512^3 particles (512^3 particles for Dark Matter species) was produced and a series of dilutions was performed, obtaining different sets of initial conditions. Their power spectra were computed and the results are shown in Figure 5.4. In particular, the black profile refers to the original set of initial conditions while the red one refers to the diluted one, *i.e.* featuring a halved resolution.
The shot noise, which modifies the profiles at different scales, is due to the granularity of the particles, which becomes relevant at small scales, because the high momenta can't be

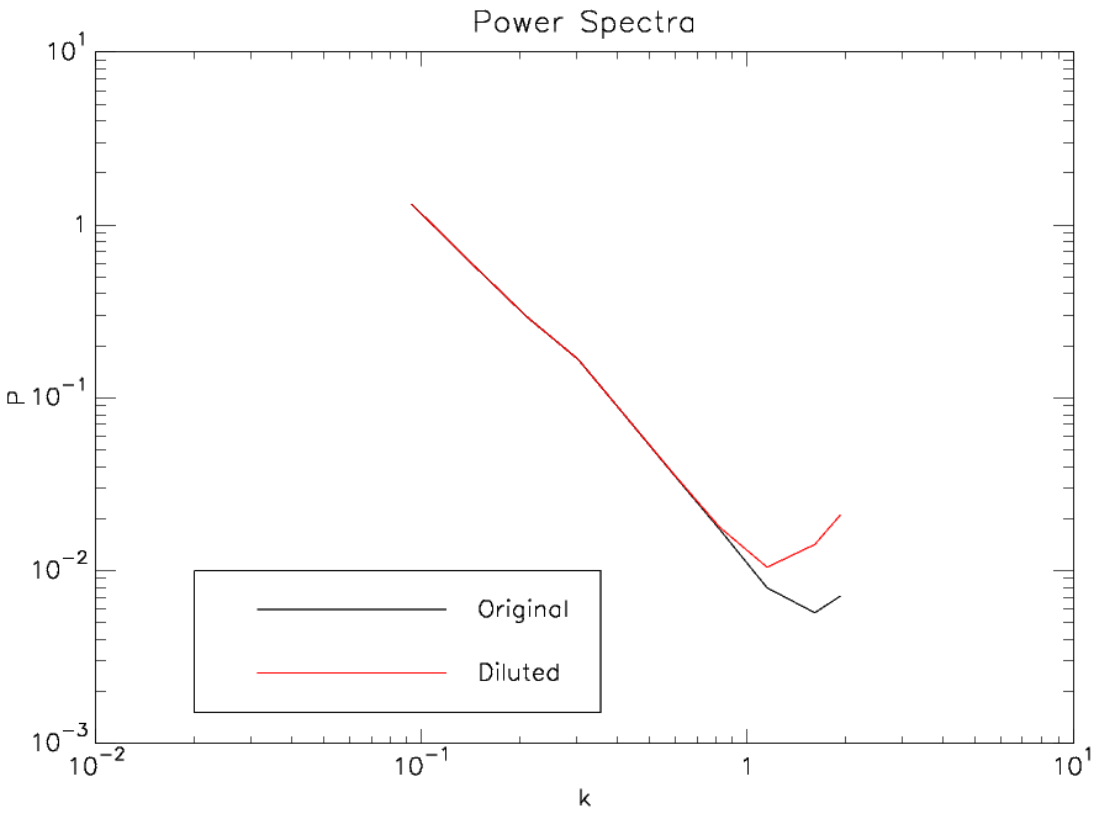

Figure 5.4: Comparison between the power spectrum of the original initial conditions and the one obtained as different dilutions of the former. As expected, they differ only at small scales, where the shot noise becomes relevant at different wavenumbers.

reached due to the Nyquist limit. This type of noise modifies the power spectra adding a term

$$\langle \delta_{SHOT} \rangle = \frac{1}{N} \tag{5.4}$$

where N is the number of particles in the box. Hence, its dimensionless form is

$$\Delta^2_{SHOT} \propto \frac{1}{N} k^3 \tag{5.5}$$

This clearly shows that, as the number of particles decreases, the shot noise becomes more important. Hence, this term is different for the different dilutions of the ICs, while the non-noisy Power Spectra is the same, since the method used for the dilution preserves the original statistical realisation of the glass file, *i.e.* the theoretical Power Spectrum of the initial conditions.
Since the power spectra obtained from the diluted initial conditions and the original ones are fully consistent, after taking into account the noise deviations, the results of the code described above can be trusted and, then, the new initial conditions can be used to perform a numerical simulation with modified resolution (diluted or zoomed).

Although the power spectra show that the code performs the dilution procedure in a consistent way, there is another test that must be made before using the zoomed initial conditions for a fully trustful numerical simulation: the high- and medium-resolution regions must be large enough to avoid the presence of intruders in the region of interest at low redshifts. This must be avoided since their presence could significantly perturb the gravitational dynamics of the high-resolution particles, resulting in modified and unrealistic results.
This check is done by performing a low-resolution simulation zoomed around a single halo of interest and checking that the obtained halo is free from intruders. As an example, in Figure 5.5 the $z = 0$ snapshot of a halo is reported, both in the case of a too small ($r_M = 2r_H$) and a wide enough ($r_M = 5r_H$) mid-resolution region. The black points represent the low-resolution particles, the blue points represent the mid-resolution ones and the red points represent the high-resolutions ones. In the former case the result is a complete mixing of the particles of the three different resolutions, whilst in the latter the regions remain fully separated until $z = 0$ with the exception of the boundaries where a small mixing occurs.

After a trial and error procedure, I found that the a mid-resolution regions with a radius as large as 4-5 time the high-resolution region is sufficient to ensure that the intruders will not interfere with the dynamics of the studied halo, provided that the high-resolution region is 1.5 times larger than the halo of interest.

A final test consists in cheking that the large scale structure is not modified since at large scales the “fine structure”, *i.e.* the fact that there is a heavy particle instead of a number of lighter particles, does not modify the behaviour of the particles.
In Figure 5.6 is plotted the $z = 0$ snapshot for two different simulations, the first one

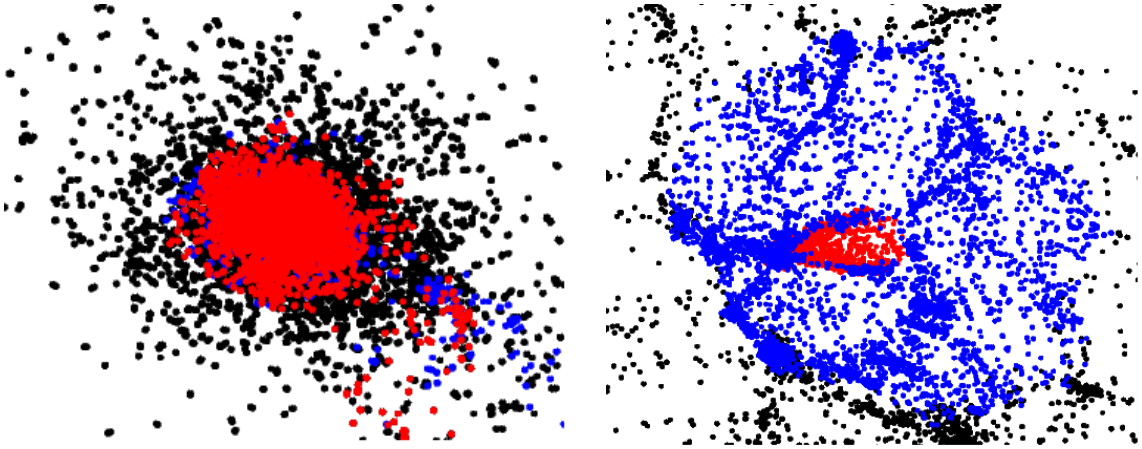

Figure 5.5: The difference between a zoomed simulation with a too small (left panel) and a wide enough (right panel) mid-resolution region. The low-resolution particles are printed in black, the mid-resolution ones in blue and the high-resolution ones in red. In the left panel, the too small medium-resolution region is completely mixed with the high- and low-resolution ones. In the right picture, the regions are clearly separated, with the exception of the boundaries of the regions. The pictures are the $z = 0$ snapshots of a simulation containing 128^3 particles for each type with box side 80 Mpc/h.

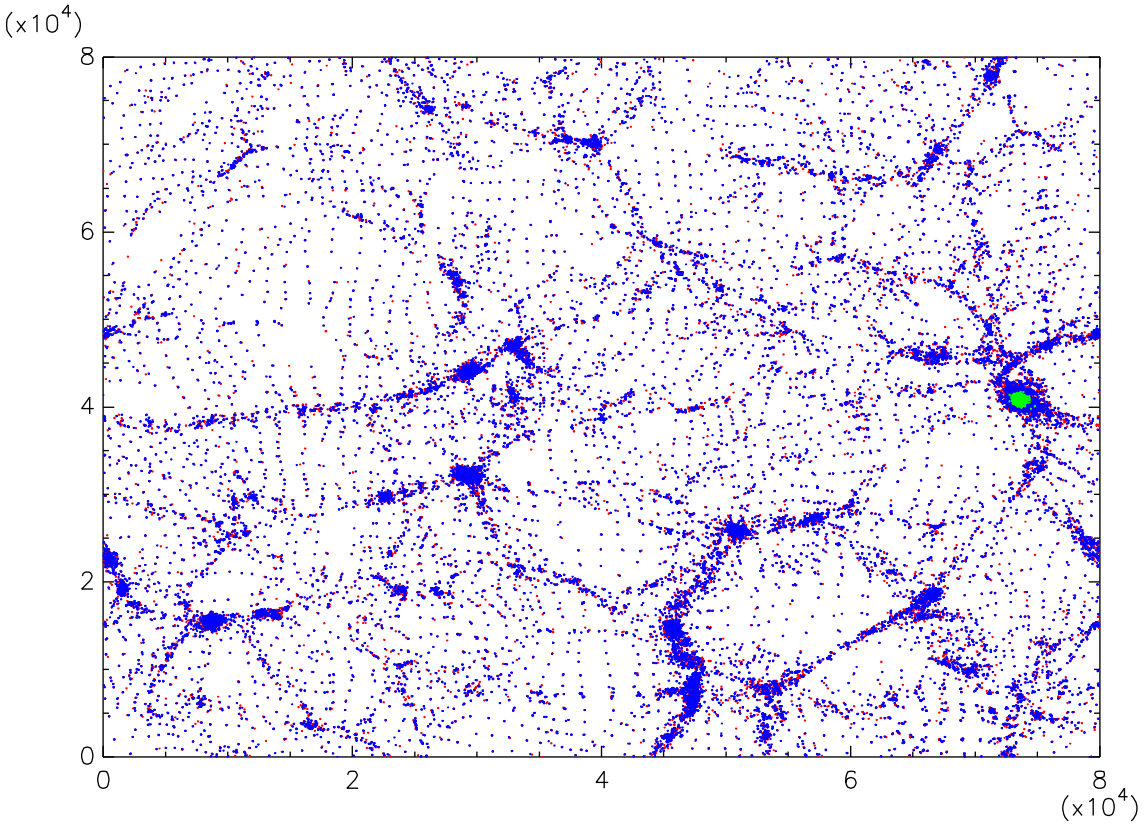

Figure 5.6: Snapshot at $z = 0$ for initial conditions of 512^3 particles per type uniformly diluted to 128^3 particle per type (red dots) and for the same initial conditions zoomed around a single halo of interest with low resolution equal to the diluted one and medium resolution twice as many. In green are printed the particles of the zoomed halo. The simulation box has side 80 Mpc/h, and the thickness of the slice is 1 Mpc/h. The blue dots are plotted after the red ones, which thus are hidden behind them since they coincide almost everywhere. The axis report the position in unit of kpc/h, which are however not necessary for discussing the goodness of the zooming procedure.

(printed with red points) is a uniform dilution of a set of 512^3 particles down to 128^3 particles for each type, while the second (printed in blue) is a zoom around a single halo with a low-resolution equal to the diluted initial conditions, and double in the mid-resolution region. As one can clearly see, the large scale structure is the same for both the simulations, thus ensuring that the dilution procedure is faithful, since the red dots are hidden behind the blue ones, as a result of the almost perfect matching between the two simulation results.

Besides testing the goodness of the produced zoomed initial conditions, some benchmark tests were also performed, in order to test how the time needed by the code varies when changing the input parameters. These tests are shown in Appendix A.

Chapter 6

The Simulations

In order to study the segregation process, I set up a series of numerical simulations aiming at identifying a single halo to be studied in detail and then following its evolution during the whole fragmentation process with the zoomed high-resolution simulations.
Primarily, the high-resolution initial conditions have been produced. Keeping in mind that their resolution would have been the one for the high-resolution region after the zooming procedure, which must be sufficiently high in order to study the radial density profile in detail, they were produced to contain 1024^3 particles for each type in a simulation box of side 80 Mpc/h. The mass resolution, *i.e.* the amount of mass each sample particle represents, at the initial redshift $z_i = 99$ is $m_+ = 1.7 \cdot 10^8\ M_\odot/h$ for the positively coupled particles and $m_- = 1.8 \cdot 10^8\ M_\odot/h$ for the negatively coupled, where $M_\odot = 1.9891 \cdot 10^{30}\ kg$ is the solar mass. These initial conditions have been produced starting from a glass file, produced by the GADGET code itself. Moreover, they were distributed upon 128 different files in order to keep the files' size small enough to be read even in a low memory-per-processor computing cluster.

In order to select a single halo of interest to be studied in detail, a low-resolution simulation must be performed. I performed this simulation using diluted initial conditions, *i.e.* the above-described initial conditions were processed using the code I wrote (see Section 4.2.5) to produce a set of initial conditions with a uniform resolution corresponding to 256^3 particles for each type. Thus, on average a single one of these low-resolution sample particles represents 64 sample particles of the high-resolution initial conditions.
The diluted simulations have been performed both for the coupled and the uncoupled (*i.e.* ΛCDM) model. The coupling strength was chosen in order to have in the final stage of the simulation well-segregated halos, but at the same time a cosmology which features global properties close to the observed one. Thus, the coupling strength must be high enough to trigger the halo segregation but not too high in order to reduce the production of large-scale "mirror" structures: the chosen coupling strength is the gravitational threshold $\beta = \sqrt{3}/2$, *i.e.* the value which produces a scalar fifth force with the same strength as gravity. The slope of the self-interaction potential for the McDE model has been fixed at $\alpha = 0.08$ (see [4]).

Then, the output of the two diluted simulations were analysed with the aim of identifying a halo which has undergone the fragmentation process. Among the large number of these halos, the one selected must balance two opposite needs: the more massive the halo, the more precise will be the analysis performed upon it, since it contains a greater number of particles, and thus a greater statistical significance can be achieved; on the other hand, as the mass of the halo increases, also the number of particles within the high-resolution region increases, along with the number in the medium-resolution one since it is computed as five time the radius of the high-resolution one. Thus the total number of particles in the zoomed initial conditions increases dramatically, leading to a more time-consuming simulation.
After selecting the halo to study, the initial conditions zoomed on it were produced as explained in Section 5.1. These were used to perform two simulations with the same parameters as the former, with the exception of the number of multiple gravitational domains of the GADAGET3 code, which has to be increased in order to allow a better load-balance. In fact, the increased number of particles in a given region results in a more difficult balance between the different processors, *i.e.* the code tends to assign very different number of particles to different processors. This could lead to an increase of the computational time needed by the code, or even to a crash of the code due to the extremely large amount of memory requested by a single processor.

The outcomes of the simulations consist, besides the snapshots, in a series of halo catalogs computed on-the-fly by the GADGET3 code using a Friends-of-Friends (FoF) algorithm (see section 4.1.3), with linking length equal to 0.2 times the mean inter-particle separation. With the chosen setup, the code does not distinguish between particles of different types when identifying the halos, meaning that the fragmented halos will be considered by the code as a single FoF group, with the exception of halos in an extremely advanced state of segregation, where the two mirror structures are too far from each other. The lack of distinction between the Dark Matter particles types reflects what could be the observational situation, as no distinction between these types is observationally accessible at the moment. In order to select well-defined halos, the FoF algorithm is forced to consider only groups of 32 or more particles. This limit corresponds to groups of mass higher than approximately $5.4 \cdot 10^9\ M_\odot/h$ for the high-resolution initial conditions and $3.6 \cdot 10^{11}\ M_\odot/h$ for the diluted ones.

Moreover, in the following the outcomes of the simulations will be presented using a density plot, *i.e.* a figure where the single particles are not plotted but only their density is shown. In order to produce such a plot, the particles in a slice centred on the region of interest are projected on a 2D plane. The latter is then divided in a grid of 2048×2048 or 1024×1024 cells and the particles density is assigned to each cell with a cloud-in-cell algorithm. Then the nodes are plotted in a color scale reflecting their density. In order to highlight the density contrast, the plot shows the logarithm of the density contrast. All the figures which refers to the same physical situation (*i.e.* the same portion of the simulation, the same halo, and so on) in different simulations have color scales calibrated on the basis of

the ΛCDM model simulation, *i.e.* the brightest color is associated with the same value for all the plots and simulations, which is the maximum value of the density field in the outcomes of the ΛCDM simulation. The latter feature allows a direct comparison between the densities of structures in different figures, even in the case they come from simulations of different cosmologies.

6.1 Hardware

The simulations described in this Thesis were performed relying on two different supercomputing clusters: the PLX supercomputer belonging to CINECA (located in Bologna, Italy) [90], and the Hydra cluster located at the Rechenzentrum Garching centre [91] in Germany. A brief description of both of them is provided in the following.
The access to the former was obtained through a "C2 class application", *i.e.* requesting computational time directly to CINECA. The project containing the description of the simulations to be done and their scientific purpose was sent to CINECA, which chose to assign 72000 cpu hours[1] to the project.

6.1.1 PLX

The PLX cluster hosted by CINECA provides 274 nodes, each one equipped with two six-core Intel Westmere processors working at 2.40 GHz and 48 GB of memory.
The internal network is made by Infiniband. The system can rely on a storage space of more than 3 PetaByte.

6.1.2 Hydra

The Hydra cluster is hosted by the Rechenzentrum Garching centre for computational physics. It is composed by about 3500 nodes equipped with Intel Ivy Bridge processors (20 cores with frequency 2.8 GHz each nodes) plus 610 nodes equipped each one with 16 Intel Sandy Bridge-EP working at 2.6 GHz. Each core features a memory of 64 GB, except for 220 of them which are equipped with 128 GB of memory, for a total of 280 TB of memory.
The cores are interconnected using an InfiniBand FDR14 network. The disk storage is of 5 PetaByte.

6.2 Diluted simulations

The preparatory simulations were performed using initial conditions featuring 256^3 particles for each type of Dark Matter particles. Thus, the smoothing length was set to

[1]The expression "cpu hours" is used to identify the total time spent by the supercomputing cluster, *i.e.* adding up the elapsed time for every processor.

(recalling equation 4.29)

$$\epsilon = \frac{1}{40}\frac{80\ Mpc/h}{256} \approx 8\ kpc/h \tag{6.1}$$

The mass resolution is approximately 64 times the one for the original initial conditions, *i.e.* $m_{\pm} \approx 1.1 \cdot 10^{10}\ M_{\odot}$

In Figure 6.1 a slice of thickness 8 Mpc/h covering the whole simulation box for the uncoupled case is shown, whilst the coupled case is shown in Figure 6.2. Both of them refer to the situation at present time, *i.e.* at redshift $z = 0$.
The comparison between the two slices shows clearly that the large-scale structure of the two simulations is very similar. The overdense regions and the voids appear in the same locations and also their geometry is extremely close, the only visible difference being the halo fragmentation that reduces the peak-to-void contrast and increases the number of structures visible in the plot. These features agree with the scenario described in Section 3.3.

I have selected from the full halo catalogs a few suitable halos for the analysis of the fragmentation process. In order to select the halo to study, the list provided by GADGET3 has been reduced on the basis of the halo mass. In particular, the more massive halos were discarded since they are conglomerates of a large number of massive halos, since they correspond to the most massive regions of the whole simulation box. Moreover, the most massive halos contains a relatively large number of particles, which means a greater amount of particles in the zoomed initial conditions, which in turn means a too large increase in the computational time needed. Additionally, the earlier low-resolution simulations of the McDE model showed that the fragmentation process is triggered by the peculiar velocity of the halo. Since the smaller halos are more likely to feature a higher peculiar velocity, as a consequence of their are fall toward a more massive structure, they should be preferred on the most massive ones. Thus, the first 200 halos were discarded. The remaining halos were analysed individually in order to identify the ones clearly showing the fragmentation process, *i.e.* a mirror structure. A sample of the halos individually analysed for the coupled simulation can be found in Figure 6.3.
Among the selected halos, the final choice is governed by the necessity of having a statistical significant analysis, and thus the more massive halos are preferred. Furthermore, the isolated halo should be preferred, since they are more "relaxed", *i.e.* they are less affected by the forces of the surrounding halos which could modify the density profile.

The halo selected for the zoomed simulation is the one in the upper right panel of Figure 6.3. It has a mass of approximatively 10^{13} solar masses. It was compared with the equivalent halo in the uncoupled simulation in order to ensure that the mirror structure is not due to a coincidence, *i.e.* two halos which are close at $z = 0$ but coming from two different regions, *i.e.* not produced by a fragmentation. This last check, however, is not strictly necessary since, analysing the particle distribution type-by-type it can clearly be seen that each one of the two mirror structures is composed by only one type of particles, and thus must be produced by a fragmentation process. Such a plot can be found in Figure

6.4, where the positive-coupled species is displayed in red while the negative-coupled in blue. The two species are clearly separated.

The selected halo (halo 204, hereafter, named after its position in the mass-ordered catalog of halos at $z = 0$ in the coupled diluted simulation) and its position in the simulation box are shown in Figure 6.5.

Once selected, the halo has been followed back in time through the snapshots produced by the code during the simulation in order to determine the range of reshifts where the fragmentation process occurs. This is necessary not only in order to improve our knowledge of the process, but also more pragmatically to determine the redshifts at which the zoomed simulations have to produce a high number of snapshots. They are necessary to follow closely all the phases of the fragmentation process, in order to understand how the radial density profile and the other properties of the halo are modified during the fragmentation. The snapshots of the halo 204 at different redshifts ($z = 0,\ 0.5,\ 1$ respectively starting from the top left in clockwise rotation) in the coupled simulation are shown in Figure 6.6. The results of the simulations described above and of the other simulations described in [4] seem to indicate that the fragmentation process occurs at redshifts between $z = 2$ and $z = 0$. However, as we will see later on, this estimate turns out to be strongly affected by the low resolution of the simulations, and the true segregation redshifts is found to be much higher in the zoomed runs.

6.3 Zoomed simulations

In order to efficiently use the code GADGET3, it is necessary to have regions of different resolution which do not cross the simulation box's borders. Hence, the ZInCo code was set to center the zoomed initial conditions on the centre of the high-resolution region. This, however, does not modify at all the results or the features of the simulations, since they assume periodic boundary conditions.
In order to allow a close study of the halo during the segregation process, I set up the code (C-GADGET) in such a way to produce a high number of snapshot in the redshifts range where the fragmentation is expected to occur, *i.e.* between $z = 2$ and $z = 0.3$. Hence, the snapshots have been produced at redshifts $z = 90,\ 60,\ 30,\ 10,\ 5,\ 4,\ 3,\ 2,\ 1.5$ and from $z = 1.2$ a snapshot every $\Delta z = 0.05$ down to $z = 0$, *i.e.* $z = 1.2,\ 1.15,\ 1.10, \ldots$.

First, it is important to check that the particles of different resolution do not mix in the region of interest, *i.e.* check that there are no intruders (see Section 4.2.5). In order to perform this check, in Figure 6.7 is reported a slice of thickness 1 Mpc/h of the snapshot at $z = 0$ with particles of different resolution plotted using different colors (red for the high-resolution particles, blue for the medium-resolution and green for the low-resolution ones) for the coupled simulation. The results, however, is indistinguishable from the one

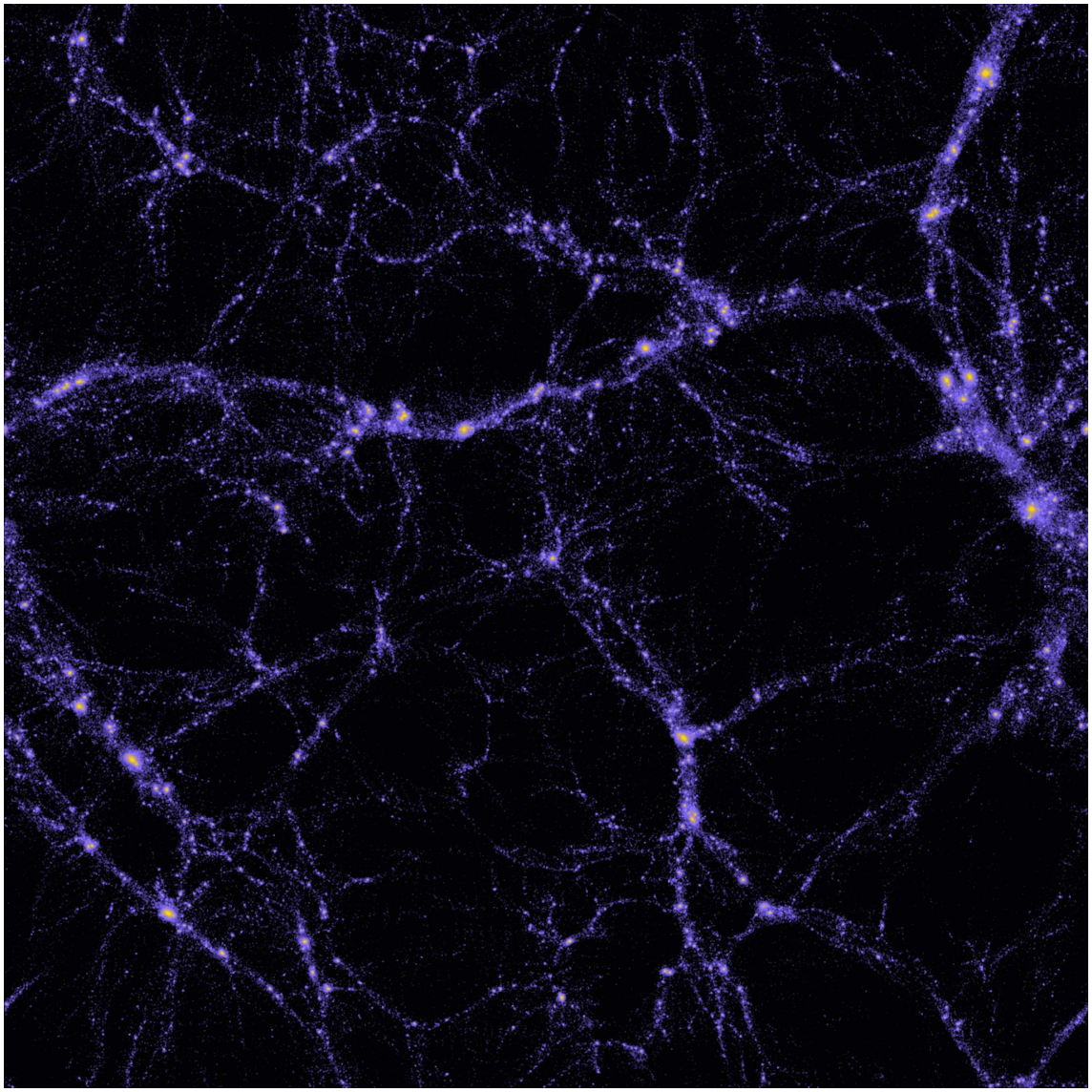

Figure 6.1: Slice of thickness 8 Mpc/h of the entire simulation box at $z = 0$ for the diluted simulation of the *uncoupled* model. The denser regions are plotted in yellow. The color scale is the same used in Figure 6.1, *i.e.* the same color represents the same density contrast.

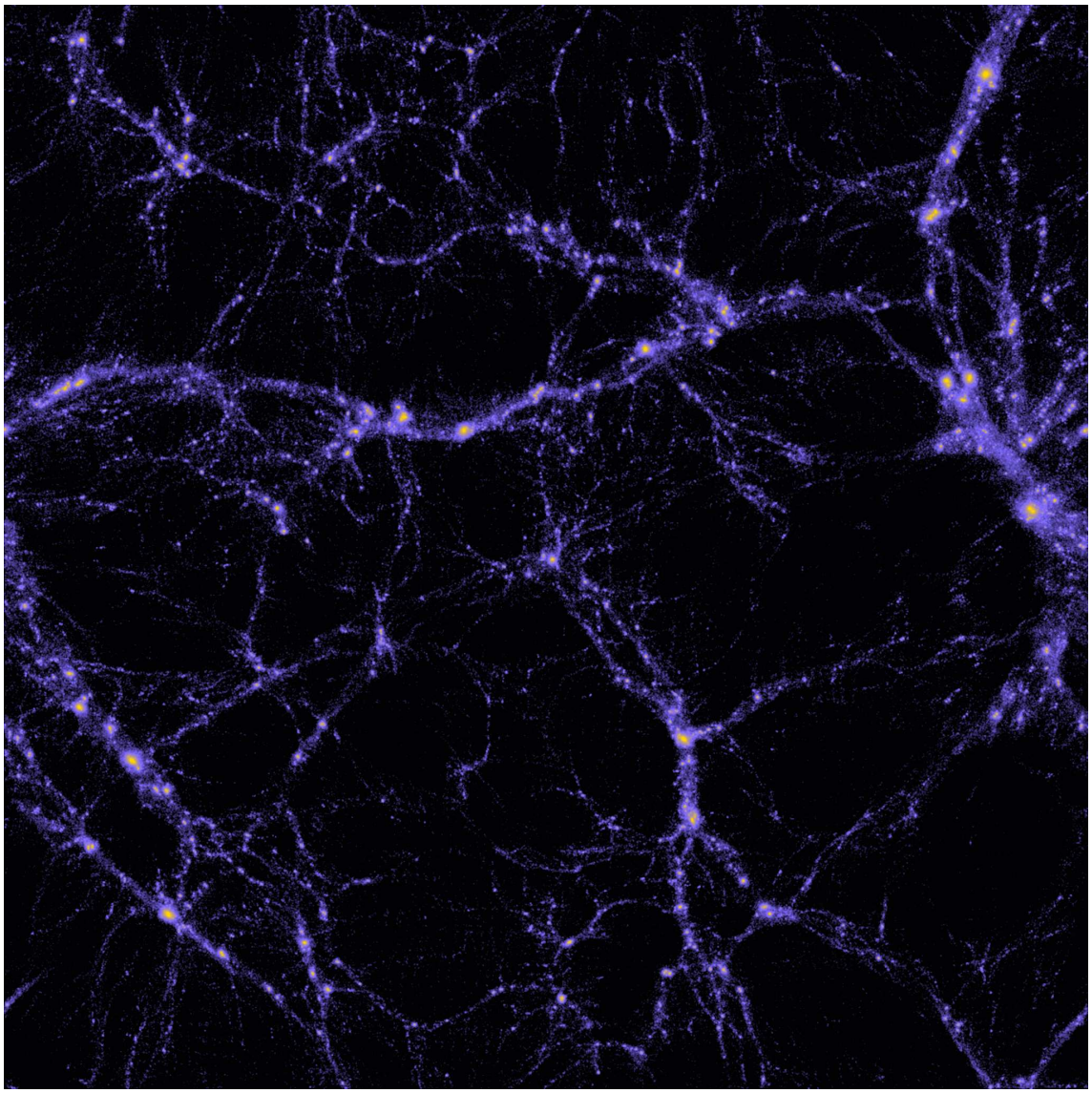

Figure 6.2: As Figure 6.1 but for the *coupled* model.

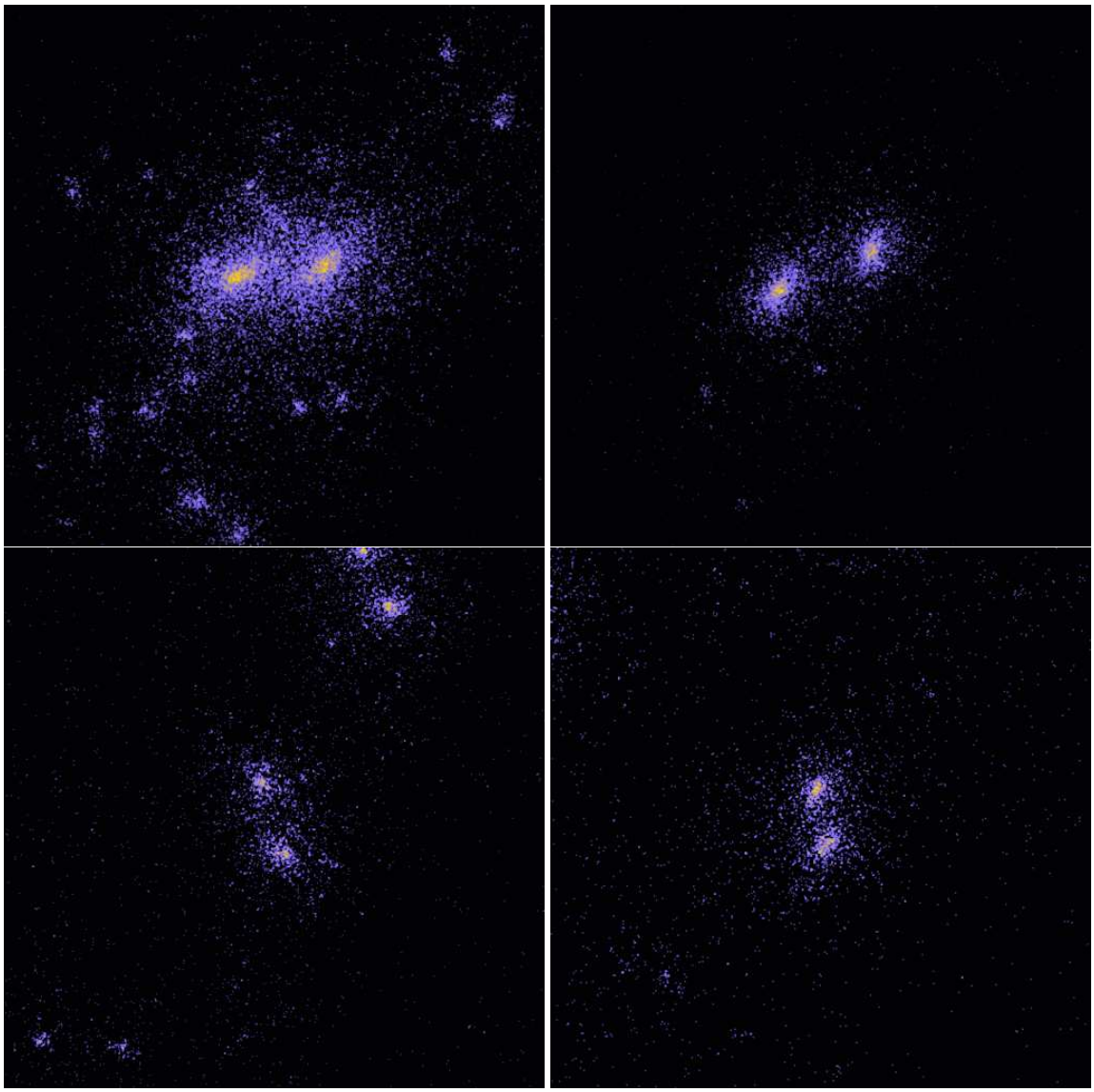

Figure 6.3: Some examples of halos analysed in order to identify the one to be processed with the zooming procedure. All the figures above have been taken with the same zoom, *i.e.* the side of each square is the same and corresponds to 1.6 Mpc/h, the same thickness (8 Mpc/h) and the same colours scale, *i.e.* equal colours in different images represent the same density contrasts, in order to allow comparison between the different candidates.

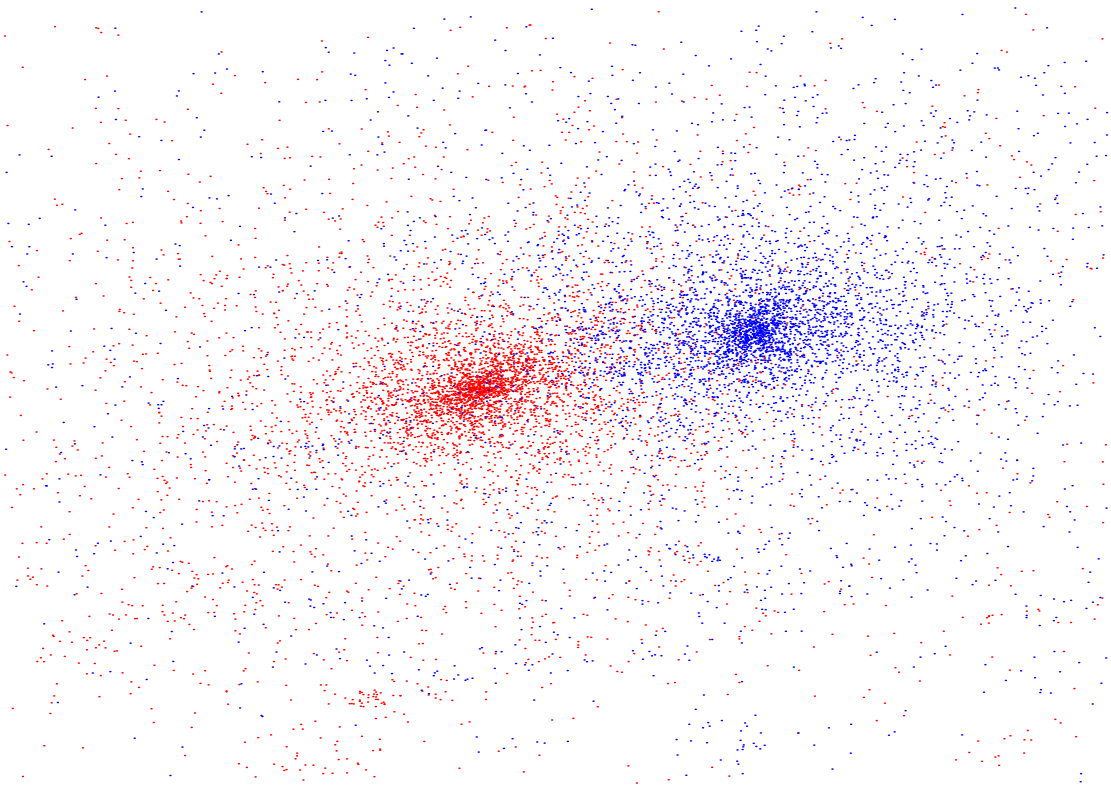

Figure 6.4: Plot of the halo chosen for the zooming procedure. Different colors are used for the two particles types: red for the positively-coupled and blue for the negatively-coupled. The two structures are clearly dominated by different types of particles, as expected for segregating structures.

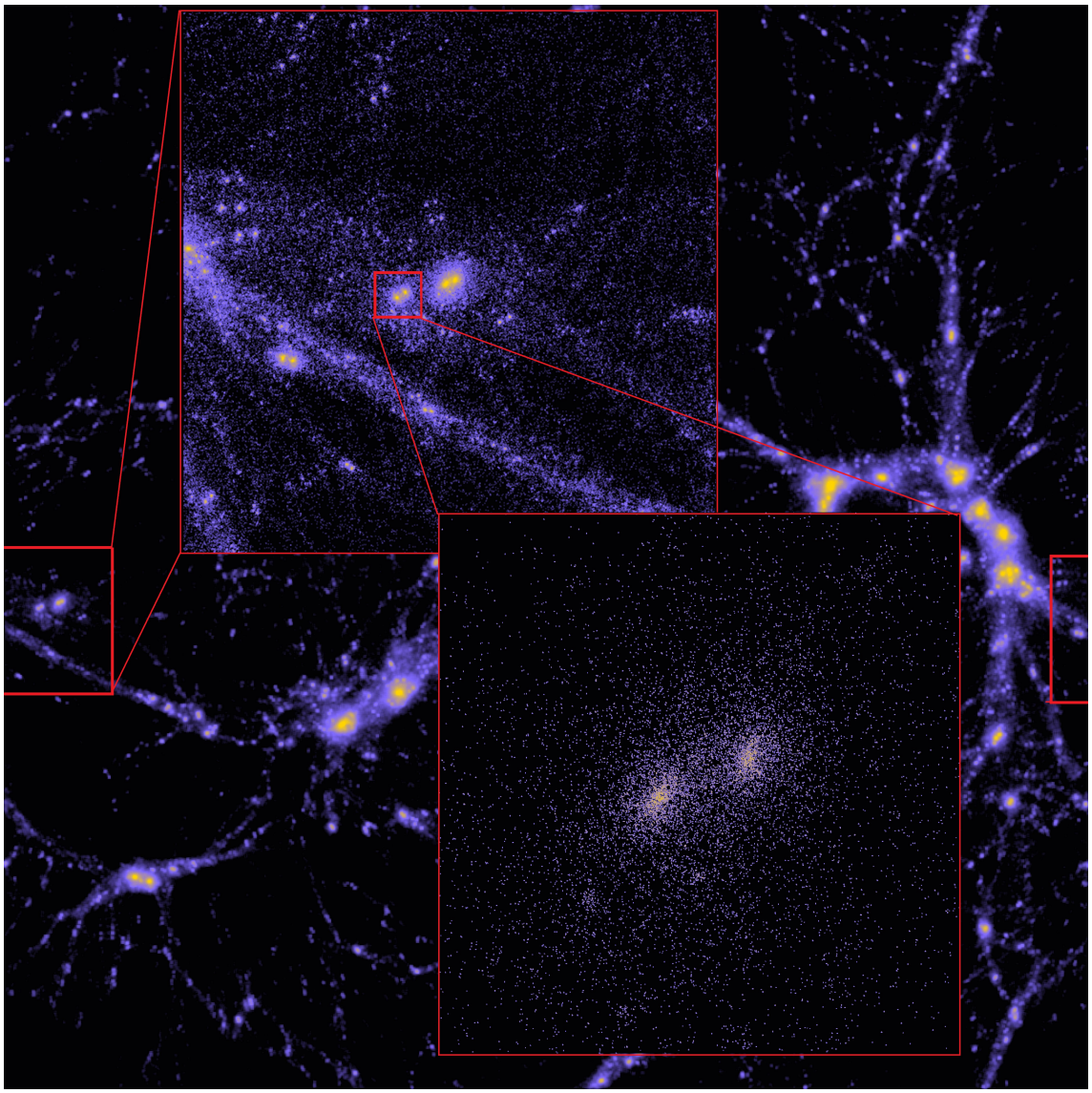

Figure 6.5: The entire simulation box (slice of thickness 8 Mpc/h) and different zooms on the chosen halo (halo 204).

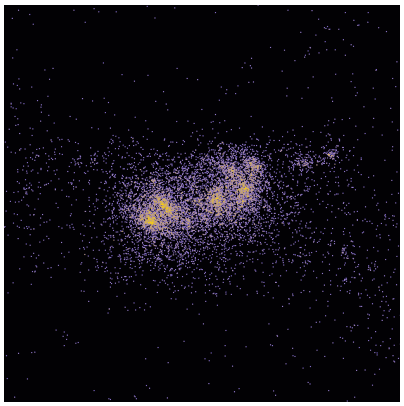

$z = 1$

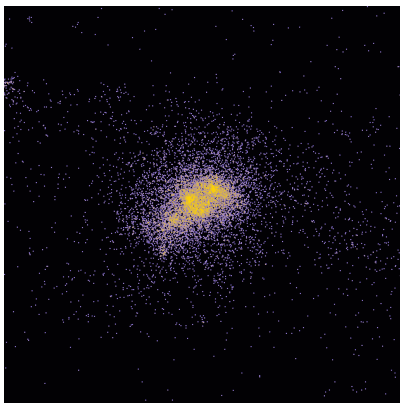

$z = 0.5$

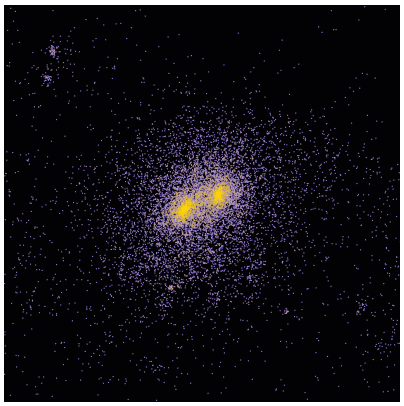

$z = 0$

Figure 6.6: Density plots of halo 204 at different redshifts.

of the uncoupled simulation. The low resolution particles slightly mix with the medium-resolution ones, whilst the latter mix more than expected with the high-resolution particles. This last feature can be addressed to the presence near the considered halo of a very high concentration of mass, *i.e.* a very massive halo, which produces a strong attraction that perturbs also distant particles, attracting them toward its center. Thus, also particles outside the high-resolution region are attracted and then enter the region of interest. The latter effects can be better appreciated by looking at Figure 6.8, where are plotted only the particles near the high-resolution region.
This effect is expected not to modify the qualitative results of the simulation, since the medium-resolution particles are sub-dominant with respect to the high-resolution ones in the region of interest, as it will be shown below. However, their presence must be taken into account when the results are analysed, since they could modify the quantitative results.
These mixing effect can be solved simply by tuning the ratio between the radii of the high- and medium-resolution regions. Unfortunately, further simulations with modified ratios could not be performed due to time constraints on the present Thesis. However, they are planned for the next months in order to remove every source of uncertainty which affects the results.

It is also important to check that, while crossing the boundaries between regions of different resolution, the large scale structures must remain the same, *i.e.* there must be continuity between the cosmic web in the different resolution regions. The continuity can be appreciated by looking once again at Figure 6.7.

Figures 6.9 and 6.10 show density plots of the whole simulation box for the uncoupled and coupled case respectively. The thickness of the slice is 8 Mpc/h. The same colour scale is used in both the Figures in order to allow a direct comparison. The large-scale structures are the same, as expected, supporting the goodness of the zooming procedure. Moreover, the coupled simulation (Figure 6.10) presents structures which appear blurred and more diffuse with respect to the uncoupled one (Figure 6.9), as a result of the segregation process which produces close mirror copies of the structures and smears the matter density peaks.

Turning to the halo under investigation (*i.e.* the one named "halo 204"), the outcomes of the coupled simulation shows clearly that the segregation process occurred as expected. Figure 6.11 shows the particles distribution around the halo 204: the positively-coupled Dark Matter particles are plotted in red, while the negatively-coupled are shown in blue. As expected, there is a clear separation between particles of different types, which form two mirror structures.

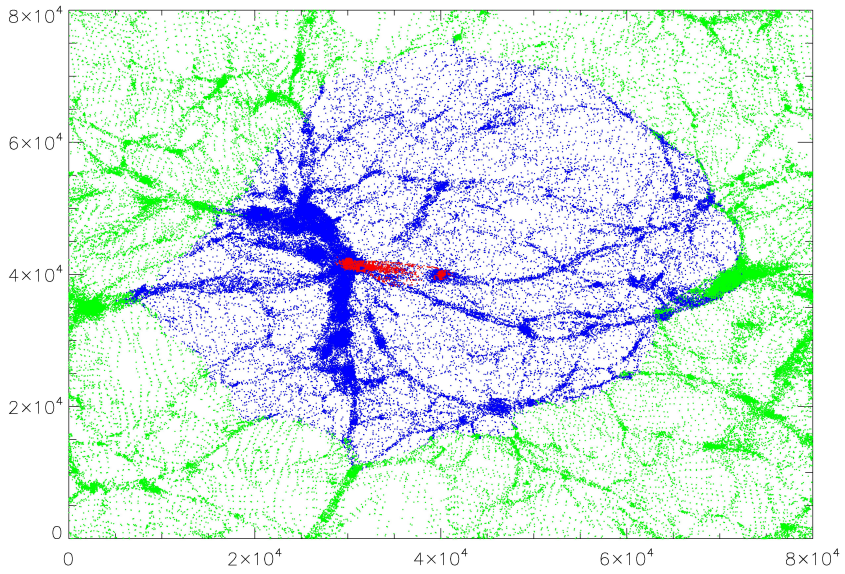

Figure 6.7: Slice of thickness 1 Mpc/h of the entire simulation box at $z = 0$ for the zoomed coupled simulation with particles of different resolution plotted using different colors: red for the high-resolution particles, blue for the medium-resolution ones and green for the low-resolution ones.

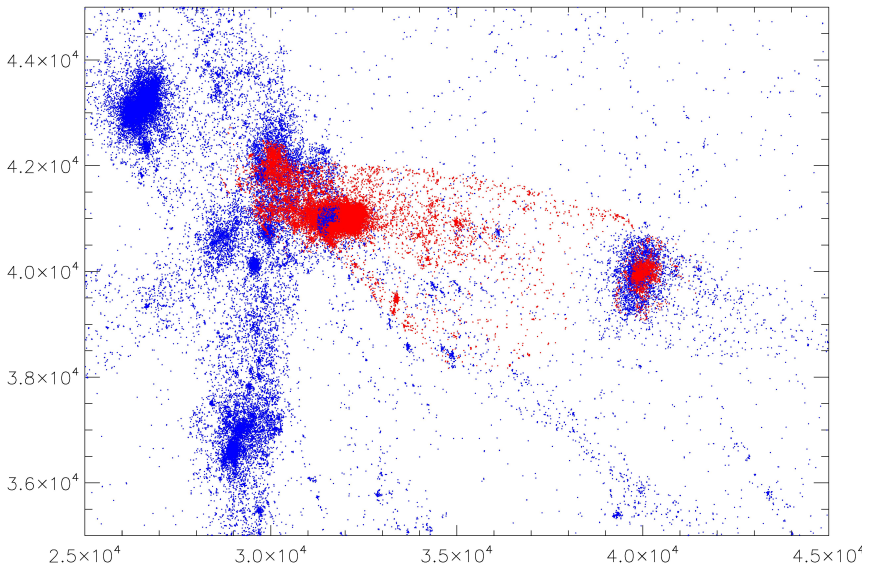

Figure 6.8: Slice of thickness 1 Mpc/h of a portion of the simulation box at $z = 0$ for the zoomed coupled simulation with particles of different resolution plotted using different colors: red for the high-resolution particles, blue for the medium-resolution ones and green for the low-resolution ones (not visible).

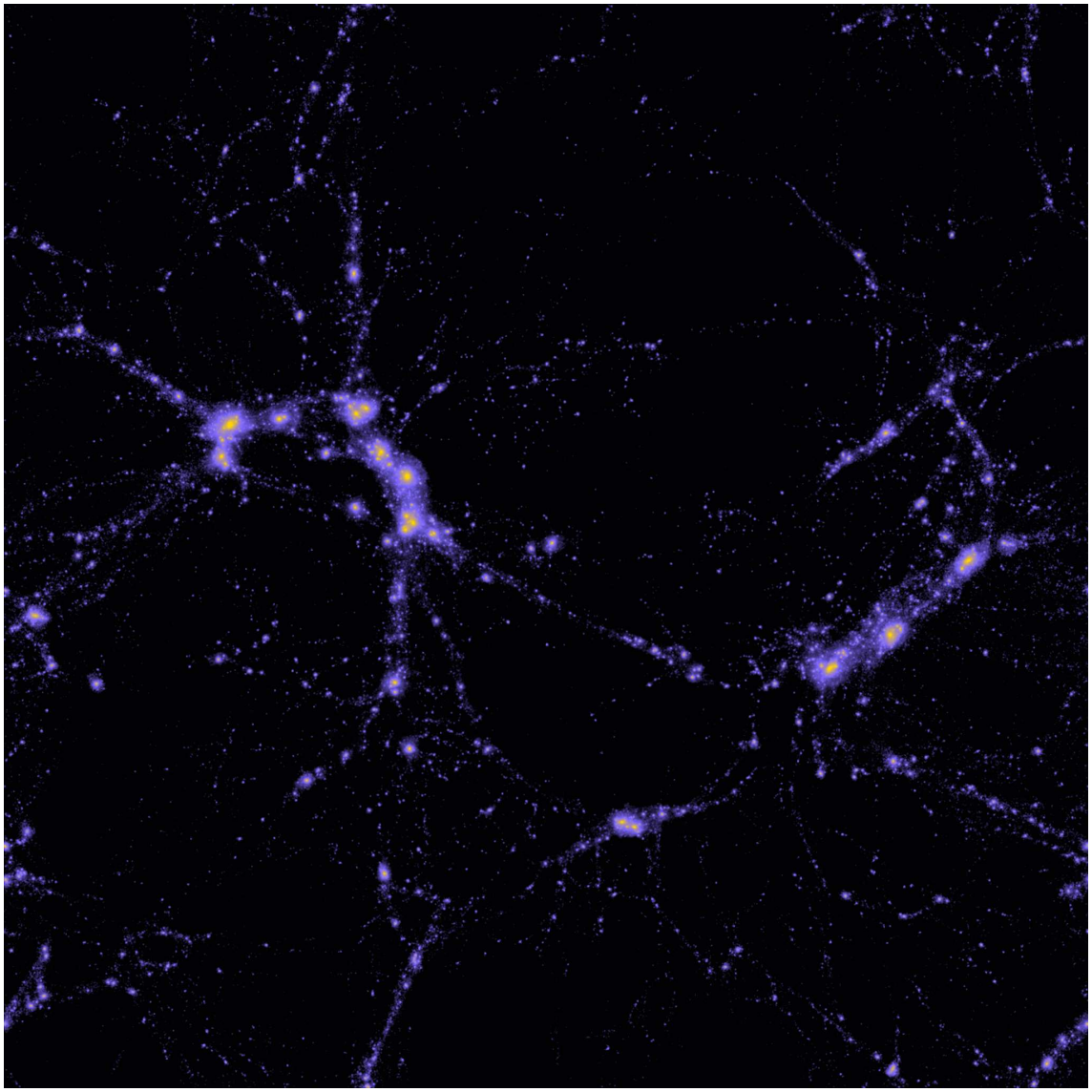

Figure 6.9: Density plot of a slice of thickness 8 Mpc/h of the entire simulation box at $z = 0$ for the zoomed *uncoupled* simulation. The color scale is the same used in Figure 6.10, *i.e.* the same color represents the same density contrast.

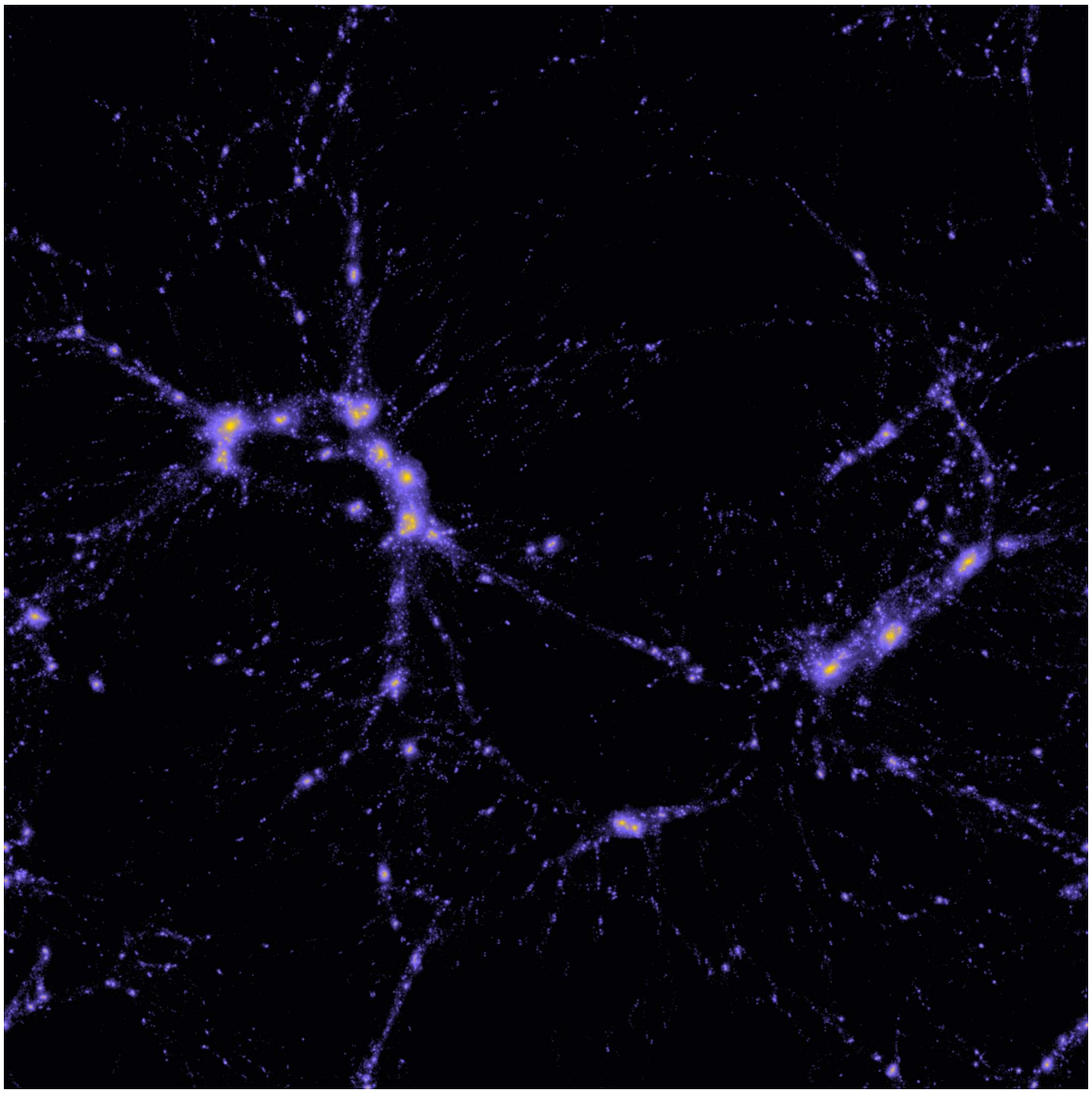

Figure 6.10: As Figure 6.9 but for the zoomed *coupled* simulation.

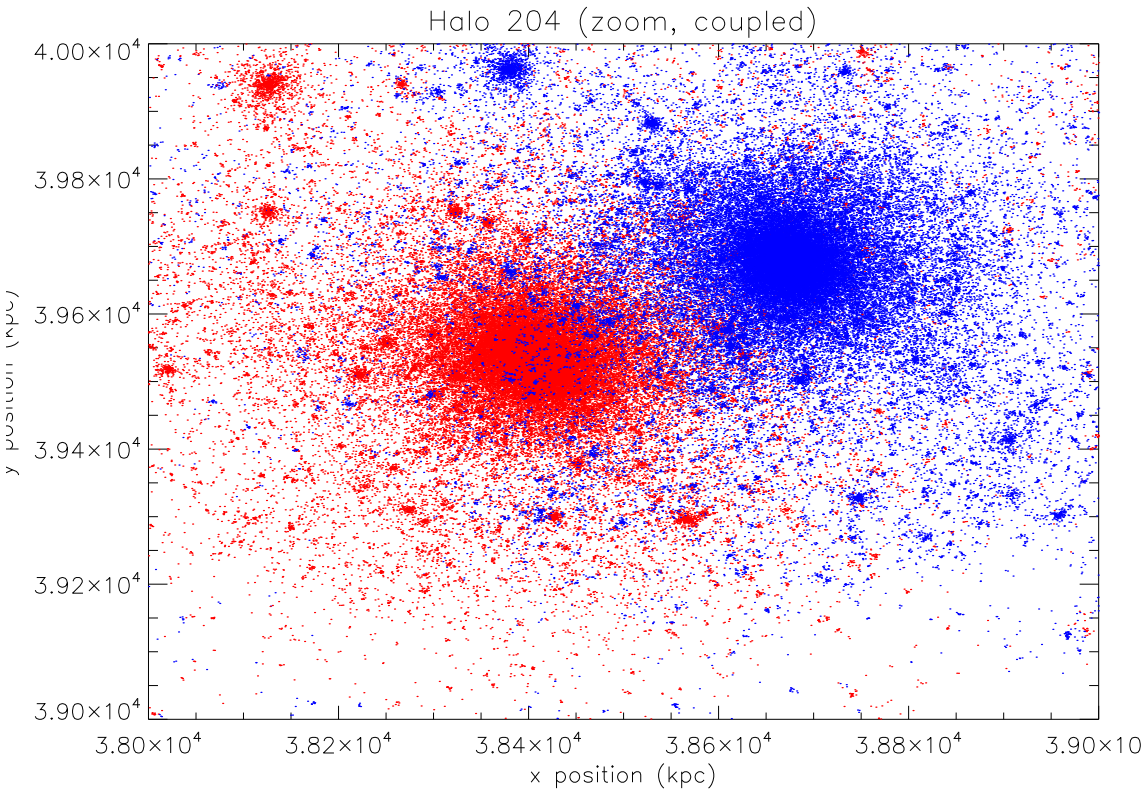

Figure 6.11: Particles distribution of the positively- (red) and negatively-coupled (blue) particles which form the halo 204.

Chapter 7

Results

7.1 Early Segregation

The evolution of the density distribution of the halo which undergoes the segregation process can be qualitatively appreciated by looking at Figure 7.1, where a series of density plots of the halo 204 at different redshifts are shown. Although the two mirror structures appear clearly segregated only at low redshifts, particularly between $z = 1.5$ and $z = 0.5$, in the top left plot the "seeds" of the mirror structures are already present at $z = 5$, where the core of the halo clearly shows two distinct density peaks, which are still close but clearly separated, next to its centre of mass.
The simulations presented in this Thesis allow the discovery that the segregation process starts at significantly higher redshift than previously thought. The previous simulations of the McDE model did not show such early segregation because their resolution was not enough in order to distinguish such a fine detail. Thus, conversely to what previously argued on the basis of the low-resolution simulations, the starting redshift of the halo segregation is significantly higher.

On the one hand, the discovery of an early segregation time in such a model represents a problem for the simulations I set up, since the main objective of the simulations was to study in detail the process of fragmentation. Hence, as explained in Chapter 6, the simulation snapshots were produced at low redshifts, where the fragmentation was thought to occur. The early appearance of a splitted core, however, shifts the "target" redshifts, *i.e.* the period of time where the fragmentation process occurs for the first time, at higher redshifts. Thus, the high number of snapshots produced between $z = 1.2$ and $z = 0$ do not catch the exact moment of the fragmentation, but only the later growth of the two mirror halos. Thus, the segregation process can not be studied in detail with the outcomes of the simulations here performed.
A new set of simulations with higher resolution and a very fine shapshot binning around $z = 5$ will then be the natural extension of this work, and could not be included in this Thesis only due to time constraints, but will be performed in the next weeks.

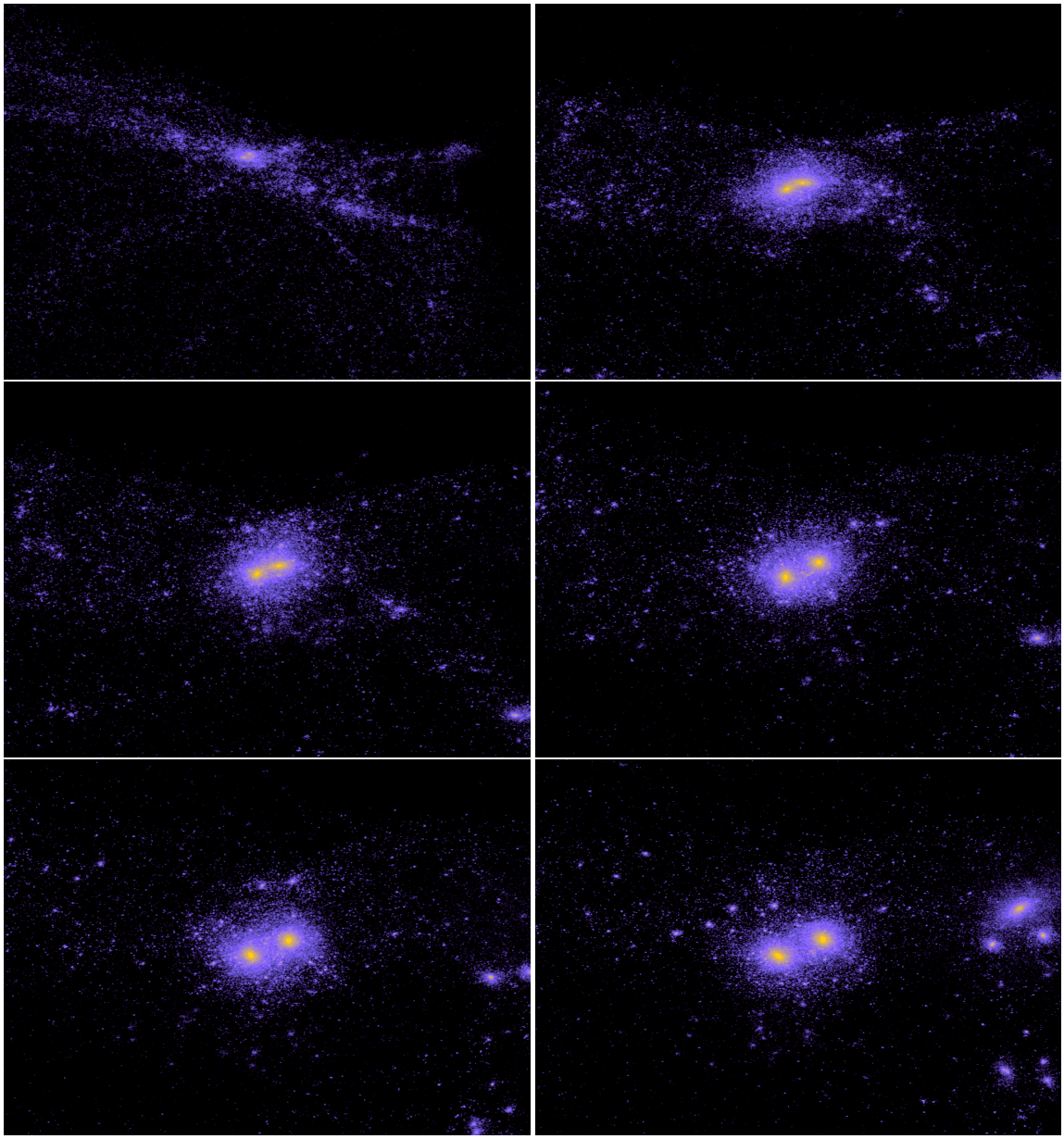

Figure 7.1: Density plots centred on halo 204 in the coupled simulation for different redshifts. All the plots have the same dimensions (1.6 Mpc/h and 1.0 Mpc/h for the major and minor side, respectively) and share the same colour scale, in order to allow comparisons. The redshifts for the different images are (from the top left to the bottom right): $z = 5,\ 1.5,\ 1.0,\ 0.5,\ 0.25,\ 0$.

On the other hand, the early fragmentation represents a new feature of the model, for the first time observed in these simulations. It pushes at higher redshift the appearance of the first differences between the uncoupled, *i.e.* ΛCDM, and the coupled models.

As a result of the uniqueness of the halo studied, it is important to check that it does not present unlikely features with respect to the other halos of the simulation and, if it is the case, suitably consider their effects on the analysis. In particular, since the fragmentation effect is triggered by a different frictional term in the equation of motion (equations 3.34-3.34) for the two different coupled species, the effect is stronger for structures with a higher peculiar velocity. However, the halo 204 appears to be sufficiently isolated and massive, as clearly shown in Figure 6.5, and thus its peculiar velocity, *i.e.* the velocity with respect to the background, is expected to be quite low with respect to the rest of the halos in the simulation box. However, the near presence of one of the most massive structures of the whole simulation box, as shown in Figure 6.5, could provide a significant source of velocity. The latter feature is confirmed by the catalog produced by the GADGET code, which lists also the velocity of the centre of mass of each halo. Considering only the halos with mass $M > 10^{11}\ M_{\odot}$, halo 204 is in the high band of velocities (1887^{th} of 11823 halos). Hence, the early segregation described could be partially due to the high peculiar velocity of the halo. However, it is important to underline that this is not a feature artificially introduced by the simulation, but conversely it represents a possible physical situation, although not the most likely one. As a result the segregation of halo 204 is expected to be one of the most prominent one in the simulation box, although more accentuated fragmentation is expected to occur. This conclusion is supported by Figure 7.2, which shows the halo under discussion (top left) along with a number of other halos in the simulation box (composed only by high- or medium-resolution particles) at the same redshift and using the same length scale, with their peculiar velocities. It clearly shows that the segregation can be more pronounced for halos with higher peculiar velocities.

Moreover, the trajectory of the center of mass of the particles that, at $z = 0$, belong to the halo is shown in Figure 7.3. The latter has evidently just an illustrative meaning, since the center of mass does not represent the center of any distribution of mass, as a result of the fragmentation of the halo. Despite this limitation, the results are expected to be qualitatively reasonable, since also the plots in Figure 7.1 are centred in such centres of mass and still follow the halo pair. Figure 7.3 shows that the halo moves in a precise direction, which correspond to one of the most massive halos in the whole simulation box (see Figure 6.5 for reference), as necessary to trigger the segregation mechanism.

The above analysis shows how the early segregation effect, detected for the first time in the simulations under discussion, appears to be an important feature of the McDE model that involves not only halos with highest peculiar velocities but also halos with smaller velocities. Moreover, a visual inspection of the halos produced by the simulations points out that this effect involves almost every mass concentration at redshift $z = 0$, *i.e.* it is not a special condition. However, how early this effect is for halos with smaller peculiar velocities can not be determined using the simulations described in this Thesis, but new

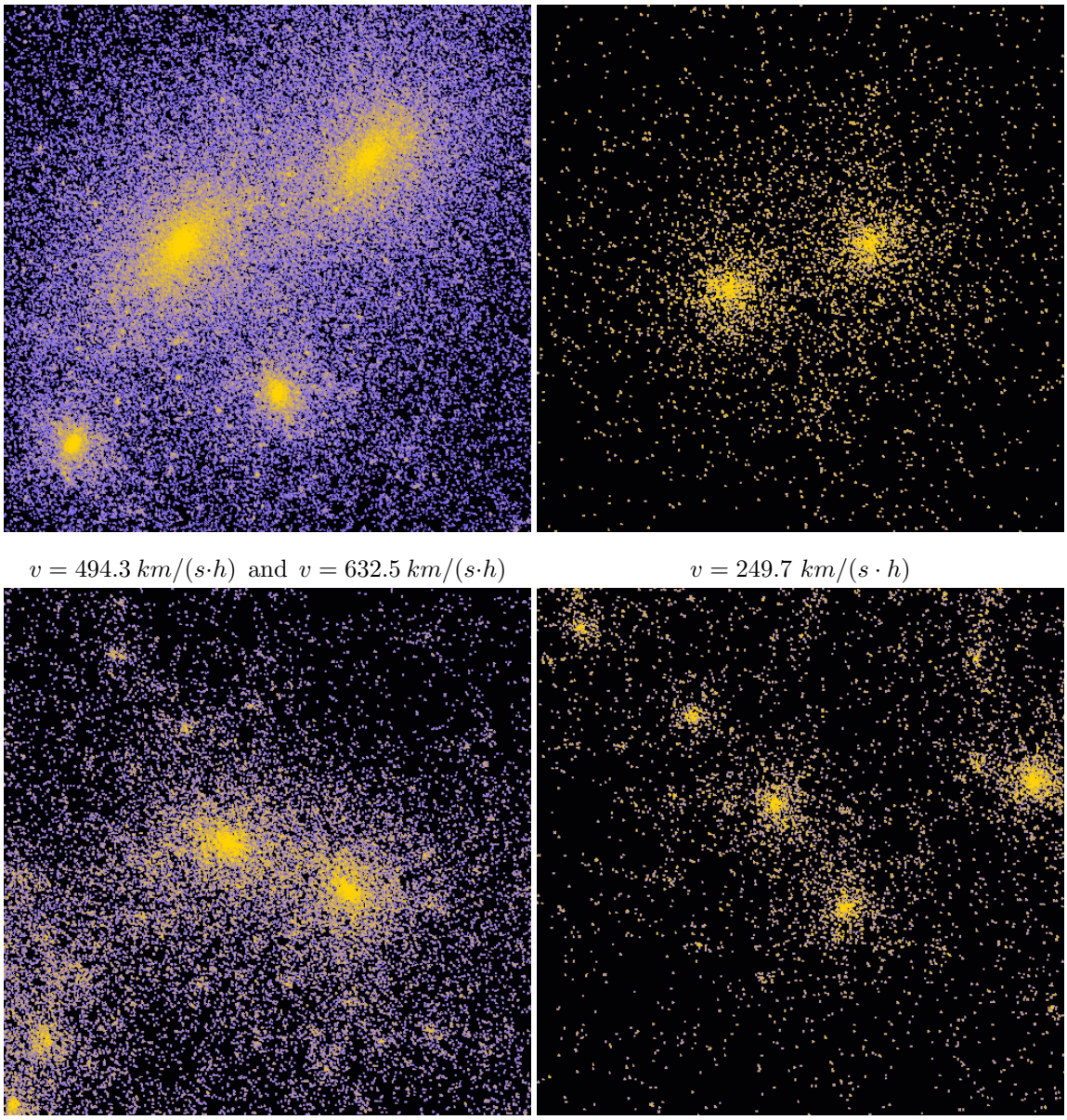

$v = 494.3\ km/(s{\cdot}h)$ and $v = 632.5\ km/(s{\cdot}h)$ | $v = 249.7\ km/(s \cdot h)$

$v = 178.9\ km/(s \cdot h)$ | $v = 475.1\ km/(s{\cdot}h)$ and $v = 512.6\ km/(s{\cdot}h)$

Figure 7.2: A sample of the segregating halos in the coupled simulation. All the pictures have the same side length. The halo 204 is the most massive one in the top left panel. The peculiar velocities v are also reported; where more velocities are printed, they refer to the different couples of segregated halos in the picture, starting from the most massive one. The fact that some fragmented halos appear in the pictures around the ones of interest is a further proof of the fact that the segregation is not a special condition in the McDE cosmology.

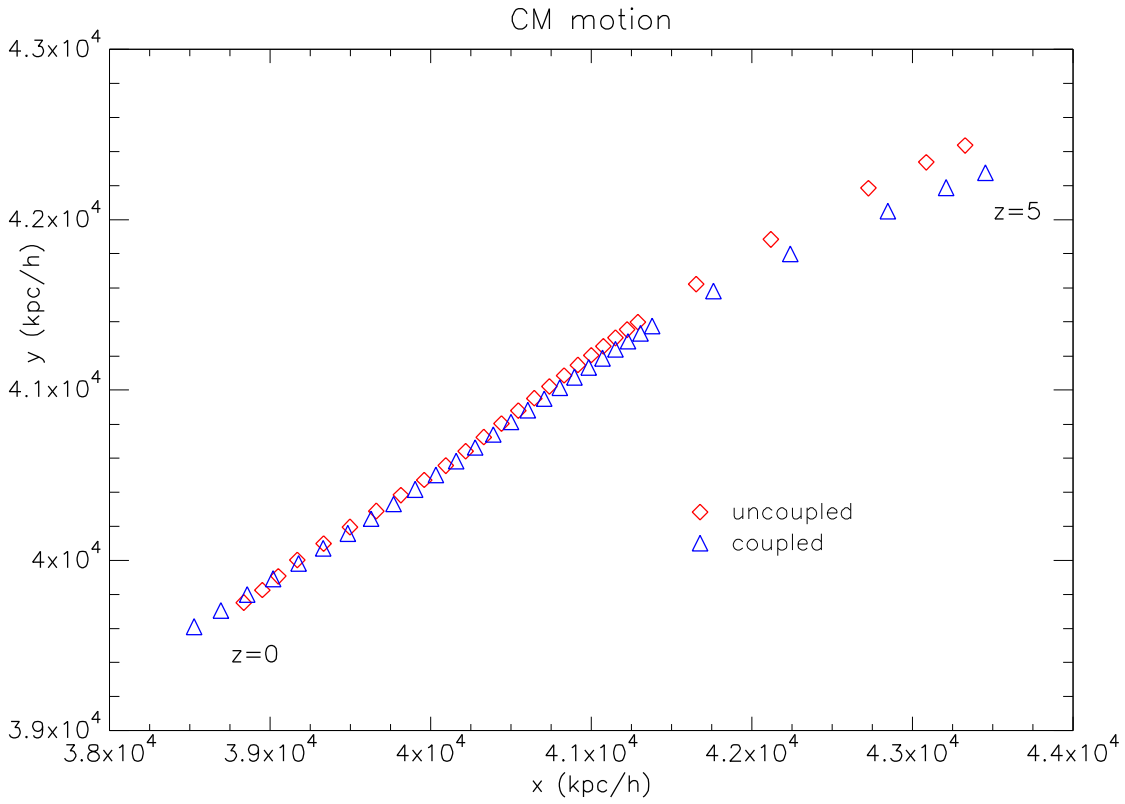

Figure 7.3: The motion, projected on the xy plane, of the centre of mass of the particles which, at $z = 0$ are contained in the halo 204. The motion is approximatively of $5Mpc/h$ from redshift $z = 5$ down to $z = 0$. Starting from the top right, the points correspond to all the redshift available, *i.e.* $z = 5,\ 4,\ 3,\ 2,\ 1.5,\ 1.2,\ 1.15,\ 1.10,\ 1.05, \ldots$,0.05, 0.

simulations zoomed on different halos must be performed.

In order to compare the outcomes of the simulations with real observations, it is important to underline that the present observations do not show any hint of the existence of mirror structures. Thus, in a McDE framework, the coupling strength must be sufficiently small in order to not produce a complete fragmentation at $z = 0$, *i.e.* the coupling must be significantly lower than the one used in the simulation presented in this Thesis, which is the gravitational threshold.

It would be helpful to constrain the redshift range where the early segregation takes place. Unfortunately, as widely described in the present Section, as a result of the fragmentation at unexpectedly high redshifts, the number of available snapshots in the range is low. In particular, the only constraint which can be placed comes from the visual inspection of the density plots at different redshift. The most interesting are shown in Figure 7.4, where in the upper panel is reported the density plot at redshift $z = 10$, while in the bottom one is plotted the density plot at $z = 5$. The visual comparison shows that the fragmentation process begins at redshifts between the two extreme ones presented in Figure 7.4. This constrains the redshift to be studied in order to closely follow the segregation process, and thus can be useful for future simulations aiming at studying in detail the early segregation shown in this Thesis for the first time.
However, also in the upper panel (*i.e.* at $z = 10$) the Dark Matter distribution shows a split profile in the centre of the plot, where the halo 204 is starting to segregate. Although the presence of such a split profile seems to point toward an even earlier segregation, the lack of snapshots at redshifts between the two shown in Figure 7.4 does not allow to deduce a such early segregation.

For low but not vanishing couplings, the McDE model could help explain the flat density profiles observed in dwarf galaxies (as it will be shown in Section 7.2). The early fragmentation discussed above pushes to even lower values the coupling strength. In fact, for couplings of gravitational strength the fragmentation process occurs at least at redshift $z = 5$. But in order to "shift" the fragmentation to redshifts near $z = 0$, the coupling strength must be significantly lower. Thus, the discovery of the early fragmentation puts a significant constraint on the realistic values of the coupling in the cosmological model studied. These are the tightest constraints to date on this class of cosmologies. On the other hand, the high peculiar velocity of the studied halo enhances the segregation effect. Thus, using the segregation of halo 204 presented in this Thesis in order to estimate the constraints on the possible couplings is not completely safe and further simulations are needed in order to confirm this result.
Moreover, the presence of two centres of accretion at high redshifts for the halo not only is still compatible with the core profile found at redshift $z = 5$, but could relax the constraints on the coupling parameter of the McDE model. The latter feature is due to the fact that, if the halo grows around two accretion points from very high redshifts without that the two mirror structures significantly depart each other until low redshifts, the coupling values compatible with the observed Universe are not tightly reduced by the early

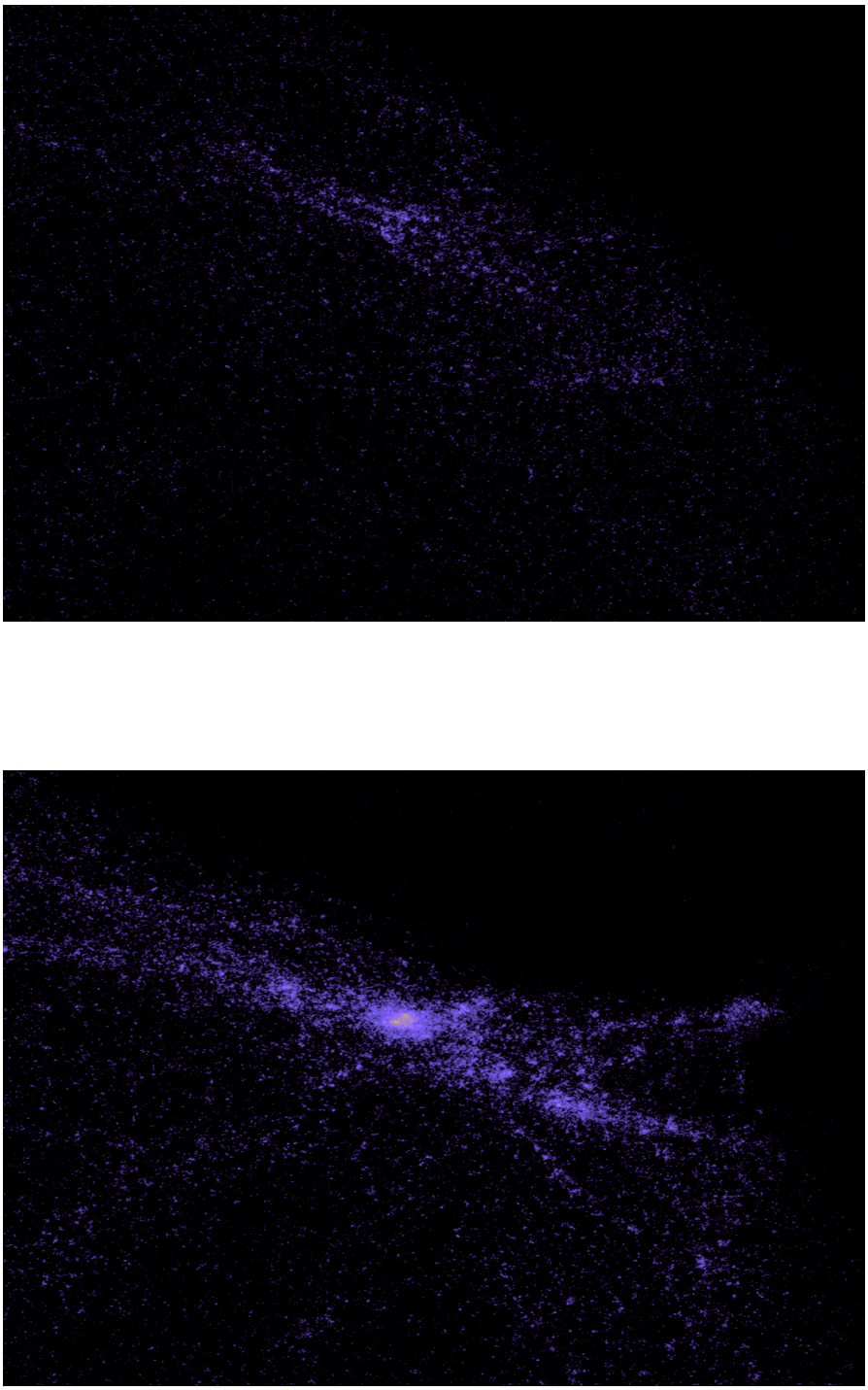

Figure 7.4: Density plots centred at the centre of mass of the particles belonging to halo 204. The upper panel refers to redshift $z = 10$, whilst the lower one refers to redshift $z = 5$. Both the plots have side equal to 3.2 Mpc/h, thickness 8 Mpc/h and the same color scale (which is also the same as in Figure 7.1).

segregation. This is a result of the fact that the observed Universe would not be in a specific stage of the segregation process, *i.e.* when the two mirror halos start to depart each other but before the bimodal density distribution is visible, but a large range of redshift would feature a flattened profile at the centre of Dark Matter halos, which in turn would mean a larger range of coupling values compatible with a flattened profile at redshift $z = 0$. The latter analysis, however, is highly speculative and must be confirmed or proved wrong by further simulations, possibly featuring an even higher resolution in the region of interest and a greater number of snapshots at redshifts between $z = 5$ and $z = 10$.

7.2 Radial Density Profiles

One of the main objectives of this Thesis is the analysis of the radial density profile of the segregating halo, in order to understand if the McDE model could help solving the "cusp-core" problem, described in Section 1.3. However, the discovery of the early fragmentation described in Section 7.1 shifts the redshift where the segregation starts at higher values with respect to what could be expected based on previous low-resolution analysis and thus the simulations, which were calibrated in order to study low redshift, must be performed again using a different set up. As mentioned above, this will be done in the near future. Despite of that, it is still possible to perform the analysis of the radial density profile on the halo although with a low time resolution due to the scarcity of snapshots at such high redshifts. They will suffer of a number of problems, due to the fact that the simulations were set up to study low redshifts, while the interesting effect (explained in Section 3.3) for the "cusp-core" problem are found to happen at higher redshifts. One of the main problem is due to the fact that, at redshift $z = 5$, the halo has a small number of particles when compared to the number of particles at $z = 0$, approximatively one fifth. Thus, the resulting density profile suffers from larger incidence of statistical errors, *i.e.* the smaller number of particles produces a greater statistical noise in the resulting profile.

7.2.1 Profiles in the uncoupled model

Firstly, the radial density profiles are analysed for the uncoupled simulation. In this case, the centre of the halo could be easily computed relying on the SUBFIND algorithm incorporated in the GADGET3 code, which identifies all the bound structures and it can distinguish between particles that are near but not gravitationally bound together and real collapsed structures. However, as explained in Section 4.1.3, this can not be done for the coupled case. Thus, for the sake of uniformity, also in the uncoupled case an alternative approach has been used, relying on a geometrical algorithm which does not consider the force acting upon the particles and, thus, can be used also for different species of particles. The code has proven to be reliable, providing results close to the estimations obtained both with a visual inspection and considering the centre of mass of halos.

In Figure 7.5 the profile for halo 204 in the uncoupled simulation is shown. The profile closely follows a broken power law profile, with inner slope $\alpha = -2$ and outer slope $\alpha = -1$,

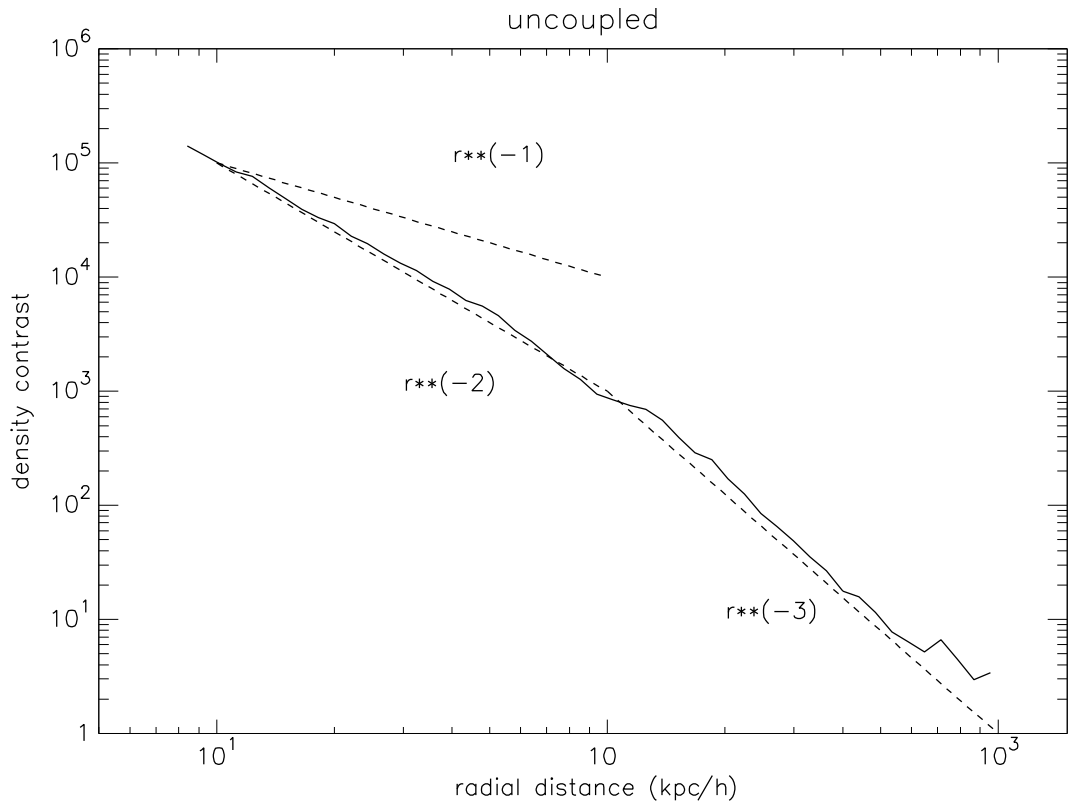

Figure 7.5: Spherically-averaged radial density profile of halo 204 in the uncoupled simulation. The profile closely follows a broken power law profile, with inner slope $\alpha = -2$ and outer slope $\alpha = -3$. For comparison, the slope $\alpha = -1$, *i.e.* the one predicted by the ΛCDM model, is plotted.

which are plotted for comparison. Also the inner slope of the NFW profile $\alpha = -3$ (see Section 4.1.3) is shown.
The profile shows the data only for values of the radial distance greater than 8 kpc/h because, as a result of the softening approximation used in the evaluation of the gravitational force (see Section 4.2), the data are trustful only starting from a radial distance equals to few times the softening length, which is of 2 kpc/h for the high resolution particles involved in the profile.
The profile of Figure 7.5 has been fitted with a broken power law profile

$$\frac{\rho(r)}{\rho_0} = \frac{\delta_0}{\left(\frac{r}{r_s}\right)^{\alpha}\left(1+\frac{r}{r_s}\right)^{\beta-\alpha}} \tag{7.1}$$

with free parameters δ_0, r_s, α, β. The former is a dimensionless parameter which represent the central density contrast, while r_s is the core radius, *i.e.* the radius where the profile passes from the inner to the outer slope. However, the profile turns out to be difficult to fit, providing very weak results, *i.e.* results which are difficult to reproduce and with high incidence of the errors. Thus, a different approach was used, in order to obtain more robust results. Since the broken power law profile has the following asymptotic behaviours:

$$\lim_{r/r_s \to 0} \rho(r) = \delta_0 \left(\frac{r}{r_s}\right)^{-\alpha} \equiv k_1 r^{-\alpha} \tag{7.2}$$

$$\lim_{r/r_s \to \infty} \rho(r) = \delta_0 \left(\frac{r}{r_s}\right)^{-\beta} \equiv k_2 r^{-\beta} \tag{7.3}$$

it is possible to perform a fitting procedure separately at small and large radii, in order to obtain the two slopes α and β. The fitting procedure gives the following results:

- $\alpha = 1.84 \pm 0.02$
- $\beta = 2.98 \pm 0.09$

The core radius r_s has been estimated as the crossing point of two power law profiles with slopes equal to the inner and the outer slopes computed before, *i.e.*

$$k_1 r^{-\alpha}|_{r_s} = k_2 r^{-\beta}|_{r_s}$$

$$\Rightarrow r_s = \left(\frac{k_2}{k_1}\right)^{\frac{1}{\beta-\alpha}} = 95.0234 \ kpc/h \tag{7.4}$$

Imposing the obtained value of r_s, the core density contrast results

$$\delta_0 = 847 \pm 6$$

The resulting profile is plotted in red in Figure 7.6, whilst in blue are plotted the two different power law profiles obtained fitting only the inner or outer points.

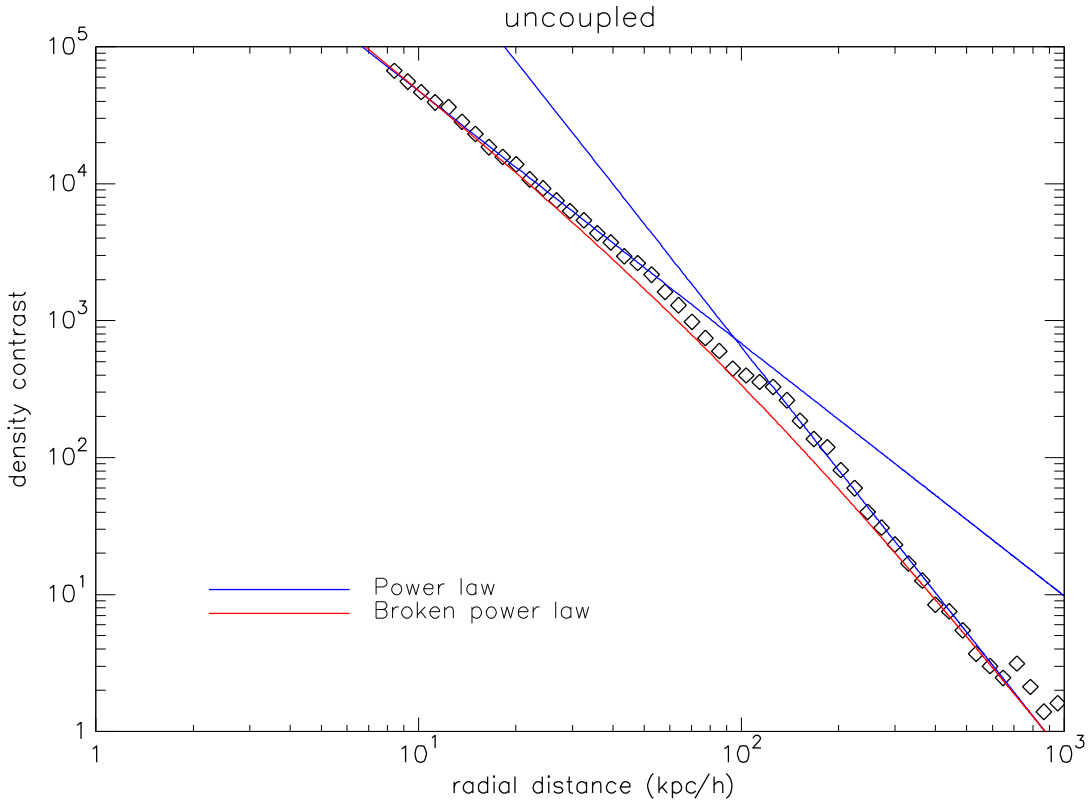

Figure 7.6: The radial density profile of Figure 7.5, the power law profiles obtained fitting the inner and outer points (blue) and the broken power law profile obtained from the fitting procedure described (red).

These profiles are similar to other profiles obtained in a wide number of numerical simulations of the ΛCDM model. Although sensibly steeper than the most used profile, *i.e.* the NFW profile, it is close to the Moore profile, which features a inner slope of $\alpha = 1.5$.
The source of the steepness is not clear. A possible source of errors is the presence of medium-resolution particles within the halo of interest. As reported in Section 6, the final zoomed simulations show a higher degree of mixing with respect to the preparatory simulation performed with a reduced number of particles in the unprocessed initial conditions, *i.e.* a significant number of medium-resolution particles were among the high-resolution ones at redshift $z = 0$, whilst this should be avoided. In order to check the possible influence of these intruders, in Figure 7.7 the contributions to the radial density profile of particles of different resolution are shown. In the profile it is possible to distinguish two different regions: at large radii the contribution of the medium-resolution particles (green profile) is approximately equal to the one of the high-resolution particles (purple profile). At smaller radii, the medium-resolution particles are sub-dominant with respect to the high-resolution ones, with a weight that decreases when the radial distance becomes small.
Despite being sub-dominant, the medium-resolution component is not negligible. Thus, its presence could be addressed as one possible reason for the deviation of the profiles obtained from the widely-used NFW profile. On the other hand, the good agreement between the slopes obtained in the coupled and uncoupled case, which can be appreciated comparing the results presented here and the ones which will be presented in the following Subsection, leaves spaces for questioning the role of the intruders in modifying the profile. However, a series of simulations with high- and medium-resolution regions tuned in order to avoid the intruders problem are planned for the next months and can not be included in the present Thesis only for time constraints.

7.2.2 Profiles in the coupled model

Turning to the profiles in the coupled simulations, some additional considerations are necessary. First, as widely described in the previous Section, the presence of a segregation effect between particles of different species of Dark Matter leads to a difficulty in the computation of the centre of the two halos. Secondly, each of these "mirror" structures contains roughly half of the original halo's mass, and thus roughly half of the original number of particles. Hence, an increased incidence of statistical noise is expected to occur.

In Figure 7.8 the radial density profiles of the two "mirror" halos resulting from the segregation of halo 204 are shown. The upper one refers to the halo mainly composed by positively-coupled particles, while the one in the bottom panel refers to the one mainly composed by negatively-coupled particles. In both of them the contribution due to the different particle types (both due to different couplings or different resolutions) are presented using different colors.
As expected, the main contribution to the profiles comes from the high-resolution particles of only one species (blue and red line). Moreover, the importance of the contribution

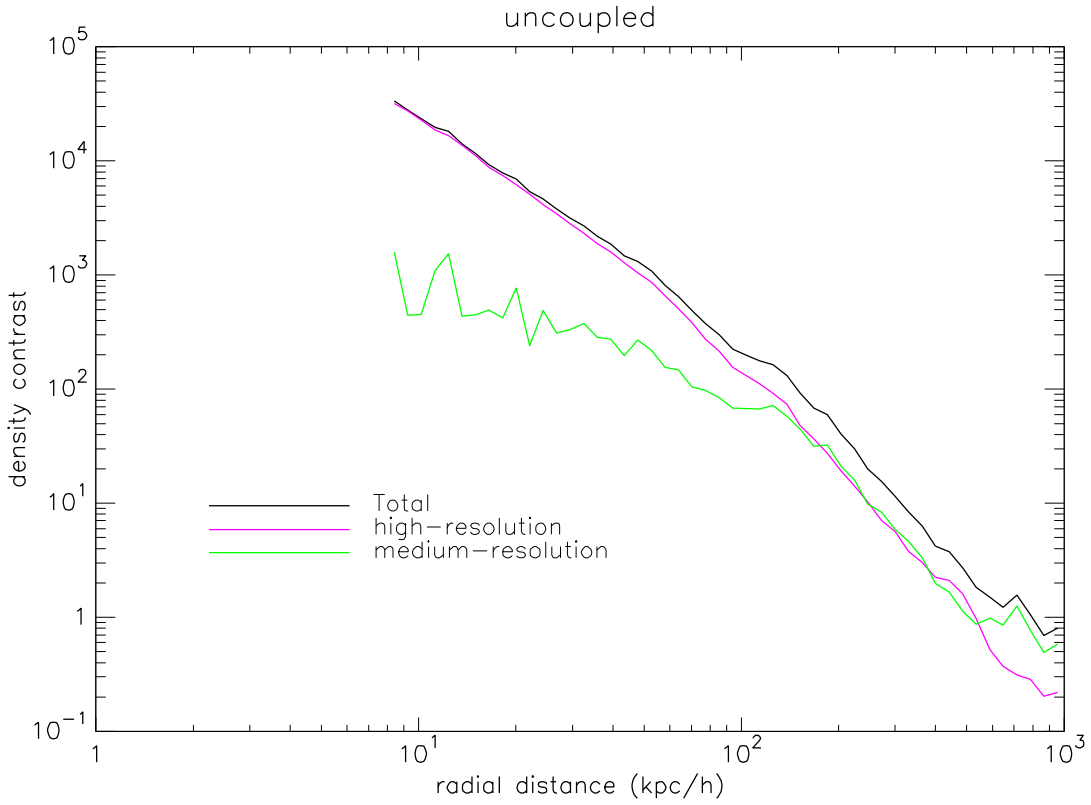

Figure 7.7: The contributions to the radial density profile of Figure 7.5 due to the high-resolution particles (purple line) and from the medium-resolution particles (green line).

increases toward the centre.

Focusing on the contributions of the medium-resolution particles (green profile), it follows the same trend found in the analysis of the uncoupled results, *i.e.* a profile largely sub-dominant near the centre of the halo with increasing importance moving toward the outer region. The strict correspondence between the profiles in the coupled and uncoupled cases is source of confidence in the goodness of the coupled simulation, since no differences beyond the expected ones are found. As explained for the uncoupled case, further simulations aiming to avoid the intruders problem are planned for the next months.
In both the profiles is clearly visible a peak in the spherically-averaged density at approximately 300 kpc/h. This feature is due to the fact that the profile reaches radial distances that correspond to the mirror halo, as confirmed by the fact that the peak is produced by the stark increase in the contribution of the particles with coupling opposite to the one of the particles composing the halo under study. Obviously, then, the profile of the single halos can not be trusted farther than 200 kpc/h.

Both the profiles have been fitted with a broken power law function (equation 7.1) using the procedure used for the uncoupled profile. However, a significant problem occurs when fitting the total density profile in the coupled case: the presence of the mirror halo at a radial distance slightly higher than the core radius r_s implies a smaller number of points to fit the power law profile in order to obtain the outer slope. Moreover, these points belong to the transient region (*e.g.* the zone between 60 kpc/h and 100 kpc/h in Figure 7.6), and thus the outer slope is underestimated. The situation gets better when analysing the contribution of a single particles type, as we will see further on.
Firstly, the fit of the total density profile of the halo composed by positively-coupled profile will be described. The fit with a simple power law function upon the inner part of the profile gives an inner slope of

$$\alpha = 1.83 \pm 0.05 \ ,$$

which is in good agreement with the slope found for the uncoupled profile. Moving to the outer part, however, some problems rise as described above. The outer slope results

$$\beta = 2.04 \pm 0.11 \ .$$

The core density contrast estimated by the broken power law imposing the obtained slopes results

$$\delta_0 = 475 \pm 5 \ .$$

The results are similar for the mirror structure, *i.e.* the halo composed mainly by negatively-coupled Dark Matter particles. The inner and outer slopes result, respectively,

$$\alpha = 1.82 \pm 0.03$$

and

$$\beta = 1.72 \pm 0.13 \ ,$$

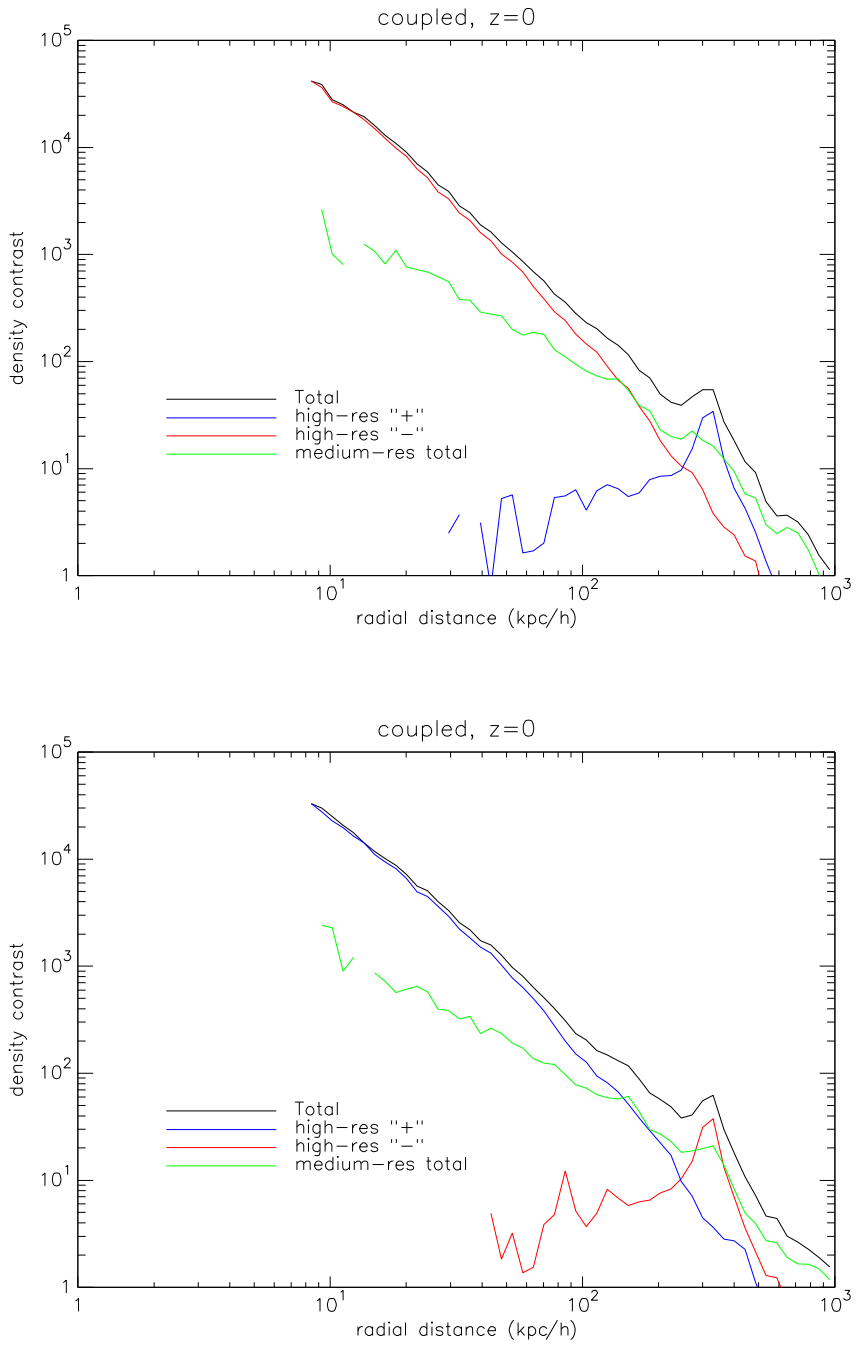

Figure 7.8: Radial density profiles of the "mirror" structures produced by the segregation of halo 204. The upper profile refers to the structure composed mainly by positively-coupled particles, while the one on the bottom refers to the one composed by negatively-coupled particles. In both the figures, the contributions of the different species of particles is reported. The discontinuities in some profiles at small radii are due to the absence of particles of the given type, which then give a null density contrast, clearly not visible in a logarithmic plot. The "+" and "-" signs in the legend label the positively- and negatively-coupled species, respectively.

while the core density contrast is estimated to be

$$\delta_0 = 380 \pm 3 \ .$$

It is remarkable that, even if the outer slopes can not be estimated with precision, the core densities roughly sum giving the core densities estimated for the uncoupled halo. This result shows that there is not a particles loss in the segregating process.

As stated above, the fitting procedure improves when only the contribution of the main particle type to each halo is considered. This happens since the distribution is not affected by the superposition with the outer part of the mirror halo, which modifies the profile lowering the outer slope as a result of the reduced decrease in the density. Thus, in this case there is no need for applying the fitting algorithm only to a subset of the points of the profile, but it can conversely be applied to the whole profile, providing a better estimation of the outer slope. The same procedure adopted above has been applied to the main contribution of both halos and the results are reported below:

- for the positively-coupled halo

$$\alpha = 1.91 \pm 0.04 \ ,$$

$$\beta = 2.84 \pm 0.07 \ ,$$

$$\delta_0 = 413 \pm 3 \ .$$

- for the negatively-coupled halo

$$\alpha = 1.88 \pm 0.02 \ ,$$

$$\beta = 3.10 \pm 0.16 \ ,$$

$$\delta_0 = 228 \pm 6 \ .$$

The profiles obtained are now more similar to the one obtained for the uncoupled halo, in particular the outer slope is much more similar. The core densities do not sum to the uncoupled core density anymore, but this is not unexpected since now only a partial contribution, even if the principal one, is considered, and thus the sum of this *partial* core densities is not expected to be equal to the *total* core density of the uncoupled case. Moreover, the difference in the values of the central density contrast δ_0 for the two species of Dark Matter is expected as a consequence of their time-dependent mass, whose evolution is described by equation 3.29.
The similarity between the profiles obtained in the coupled and uncoupled case can be better appreciated looking at Figure 7.9, where the obtained profiles are reported after being normalized to their maximum value. It can be clearly seen that for the profiles obtained fitting the total density of the two fragmented halos, the resulting profile is starkly different from the uncoupled one at large radii, as a consequence of the reasons described above. However, when only the predominant component is considered, the

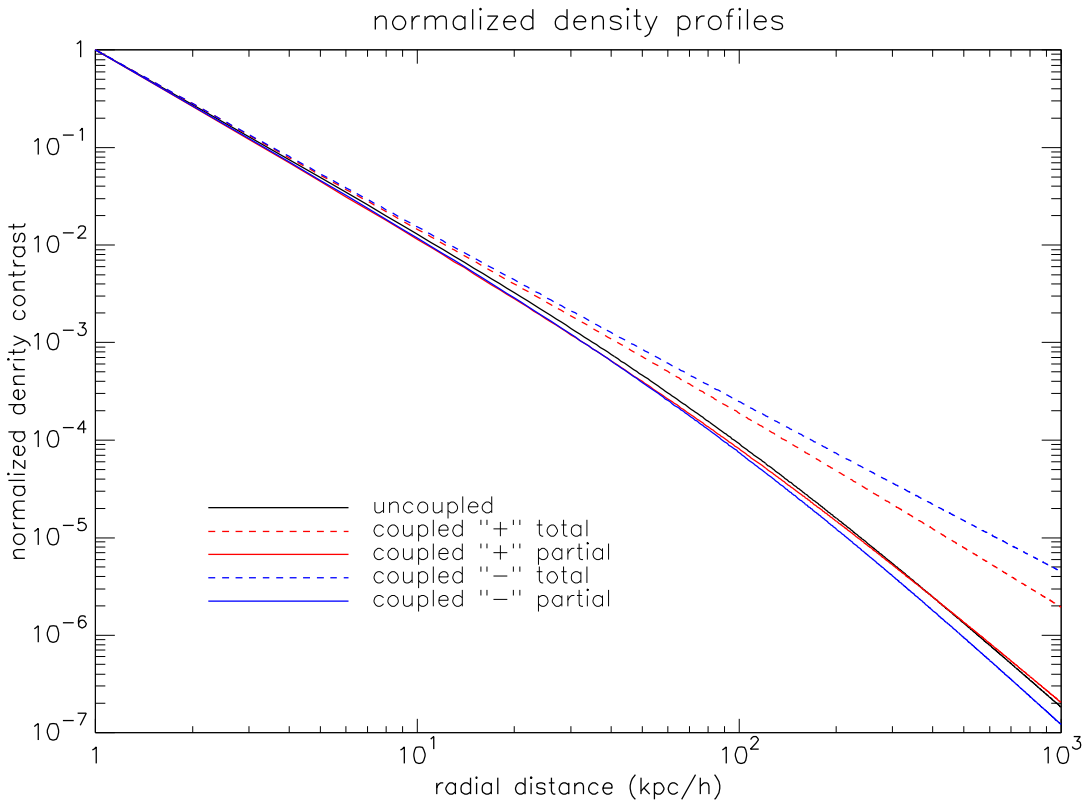

Figure 7.9: The radial density profiles obtained for the uncoupled and coupled halos, normalized to their maximum value. The "+" and "-" signs in the legend label the positively- and negatively-coupled species, respectively.

obtained profiles become similar.

The results presented above show that the fragmentation process produces two mirror halos that have the same density profile of the uncoupled case. Although expected, this result ensures that there are no additional processes, at least for the Dark Matter, which modify the matter distribution in the resulting halos. However, the presence of the companion structure modifies the outer total density profile, reducing its slope.
Observationally, this could rise some problems in the case of a full segregation. However, since no mirror structures are observed in the real Universe, the coupling strength must be sufficiently low to avoid a complete segregation at present times. Thus, the profile which must be compared to the observed ones is the one featuring sub-halos non completely segregated, *i.e.* in the early phases of the fragmentation.

7.2.3 Profiles at high redshift

The latter profile to analyse is also the more interesting, since is the one which could help alleviate the "cusp-core" problem since it is expected to feature a significantly modified profile with respect to the usual profile found in the uncoupled simulations. Namely, it is the profile of halo 204 in the coupled simulation at redshift $z = 5$, where the segregation process began (see Section 7.1). It is shown in Figure 7.10. For the reasons explained earlier, this profile can not be as precise as the ones presented above.
The centre of the profile was taken as the middle point between the centres of the two sub halos, obtained processing with the geometrical algorithm described in Section 4.1.3 only the particles of a given species. The choice is obviously not unique, another one is *e.g.* the centre of mass of the two halos. However, since the two mirror structures have approximately the same mass (a feature confirmed by the analysis of the density profiles at redshift $z = 0$ in the coupled model), the two choices give very close results. It is however important to underline that the density profile is very sensible also to small changes of the centre location, thus the centre must be in general carefully chosen.
The most remarkable feature of the profile in Figure 7.10 is the presence of a central region featuring a constant density, *i.e.* a "core". The core radius is approximately of 50 kpc/h. For larger radii the profile drops following a power law $\rho \propto r^{-\alpha}$ with slope $\alpha = 2.23 \pm 0.05$. The contributions from the two Dark Matter species are also reported: the negatively-coupled species is sub-dominant in the halo core, confirming the picture outlined by the fitting procedure, which found a lower inner density for the negatively-coupled halo.

Profiles featuring a core in the density distribution are commonly found in many observations of dwarf galaxies (*e.g.* in [93] and [94], while in [92] the same problem is found in galaxy clusters), but they are still difficult to explain in the framework of the ΛCDM model. This first flat profile, if confirmed by further simulations, could help explaining the observations of cores in the galaxy matter distribution. A McDE model featuring a coupling strength significantly lower than the gravitational threshold used in the simulations presented in this Thesis, in order to have a segregation mechanism which starts near

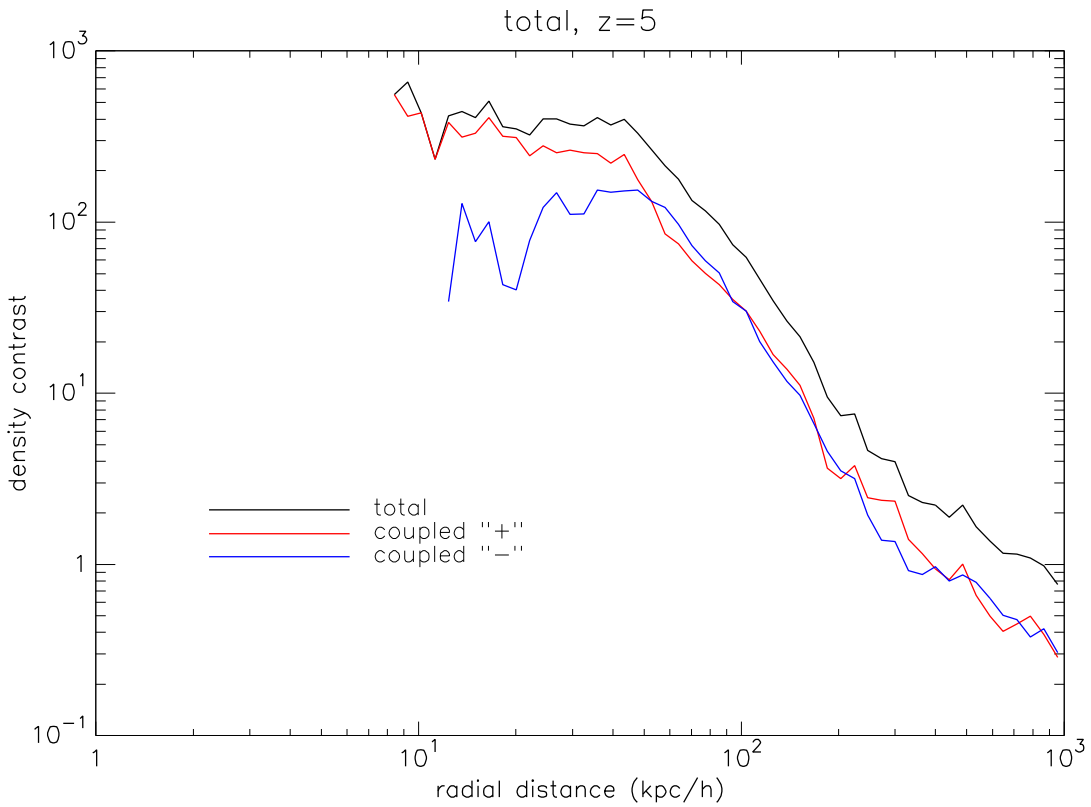

Figure 7.10: The radial density profiles of the total density contrast for the halo 204 at redshift $z = 5$. The centre of the profile was taken as the middle point between the centres of the two mirror halos which were starting to form. The "+" and "-" signs in the legend label the positively- and negatively-coupled species, respectively.

$z = 0$, could explain the flat core as result of the halo segregation which, in the earlier stages produces a flat profile due to the ongoing departure of the two mirror structures. From an observational point of view, since the observations do not distinguish between the different Dark Matter species hypothesised, the only relevant profile is the total one.

7.3 Halo Mass Function

The quantitative analysis of the outcomes of the simulations can be performed *e.g.* through the Halo Mass Function (described in Section 4.9, HMF hereafter), which quantifies the abundance of the collapsed structures as a function of their mass. The computation of the HMF presented here is based on the Friends-of-Friends algorithm implemented in the GADGET3 code, which provides a catalogue containing, among other information, also the mass of the halos.

The HMFs can be trustfully analysed only for the diluted simulations, where all the structures are equally represented, *i.e.* represented by the same particles. On the other hand, in the zoomed runs the different particles which form the three resolution regions introduces spurious effects on the HMF, as a consequence of their increased number density which could lead to a spurious increase in the small-mass halo number.
Hence, the HMFs obtained for the zoomed simulations should be considered only a qualitative way to test the goodness of the zooming procedure and not a physical description of the system studied. Conversely, the HMFs obtained for the diluted simulation really describe the statistical properties of the system studied and thus can be used to verify that the simulations performed trustfully reproduce the features of the McDE model.

The HMFs of the diluted simulations are shown in Figure 7.11. The high statistical noise which dominates at high masses is due to the fact that only a low number of halos with such high masses are present in the simulation box. Thus, for a statistically significant analysis of the high-mass tail of the HMFs, a bigger simulation box is required (see [4] for such analysis). Restricting to the low-mass region of the HMF, it is visible a lowering in the quantity of halos in the coupled scenario with respect to the uncoupled one. In particular, the dip reaches a minimum value of 0.7 for a mass approximately of $2 \cdot 10^{11}\ M_{\odot}$, *i.e.* the number of halos with approximately this mass in the McDE model is about the 70% of the number of halos in the standard ΛCDM cosmology. The latter feature is better visible in Figure 7.12, where the ratio between the coupled and the uncoupled Halo Mass Functions is shown.
The latter feature matches the previous finding described in [4], where it was shown to be a consequence of the fragmentation process which splits halos in two mirror structures with mass roughly half the mass of the original one. Also, in the paper is described how this feature could help reconciling the last PLANCK results with the prediction of the ΛCDM-based simulation, but at the same time it exacerbates the missing-satellites problem, since it predicts a higher number of small objects.

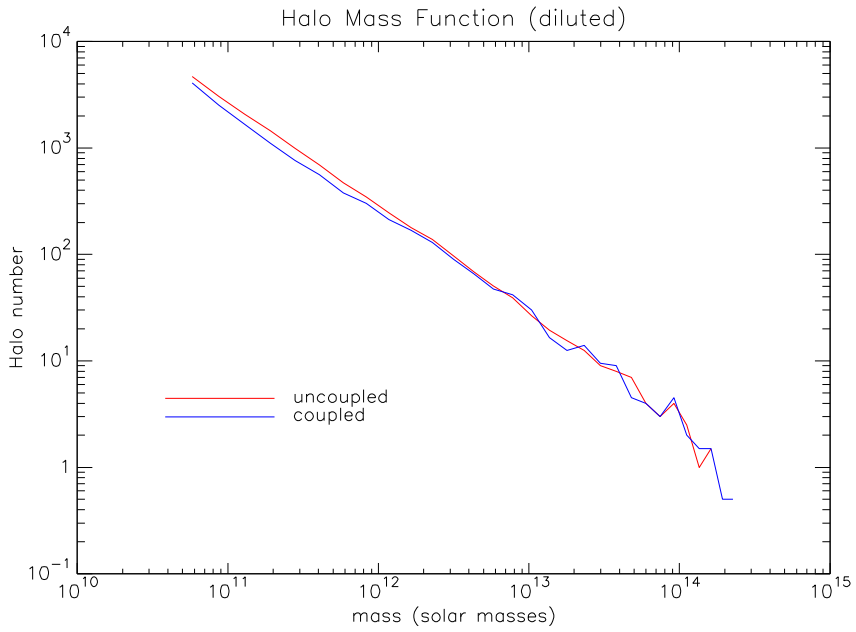

Figure 7.11: Halo Mass Function from the diluted simulations. The statistical noise which dominates for high values of the mass is due to the low number of halo featuring a such high mass.

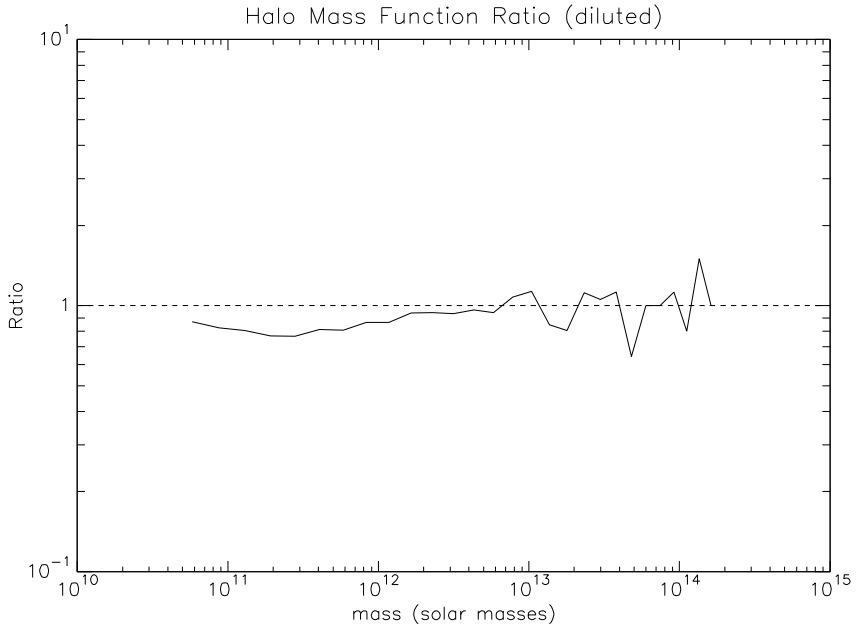

Figure 7.12: Ratio of the Halo Mass Function for the coupled and the uncoupled diluted simulations. The statistical noise which dominates for high values of the mass is due to the low number of halo featuring a such high mass.

For what concerns the zoomed simulations, the HMFs are shown in Figure 7.13, and their ratio is shown in Figure 7.14. In this case also, the profiles follow the behaviour described for the uncoupled simulations, featuring a HMF decreased in the coupled model for low-masses with respect to the uncoupled one.

Taking into account the higher statistical noise which appears in the HMFs presented here with respect to the ones in [4], which is a consequence of the approximatively 2000 times smaller simulation box, the HMFs for both the models are quite similar. This should be considered as a proof of the goodness of the performed simulations, which replicate the previously-discovered features of the McDE model.
The latter result, in particular, is not trivial since the simulations presented in this Thesis are the first ones performed using particles of different resolution in the McDE cosmological context. Once again, the agreement between the predictions of the McDe model and the obtained results shows that the zooming procedure adopted (described in Chapter 5) is viable for trustful zoomed simulations, since the global properties of the McDE model are well preserved by the zooming procedure. Consequently, also the new results shown in the present Chapter are reinforced.

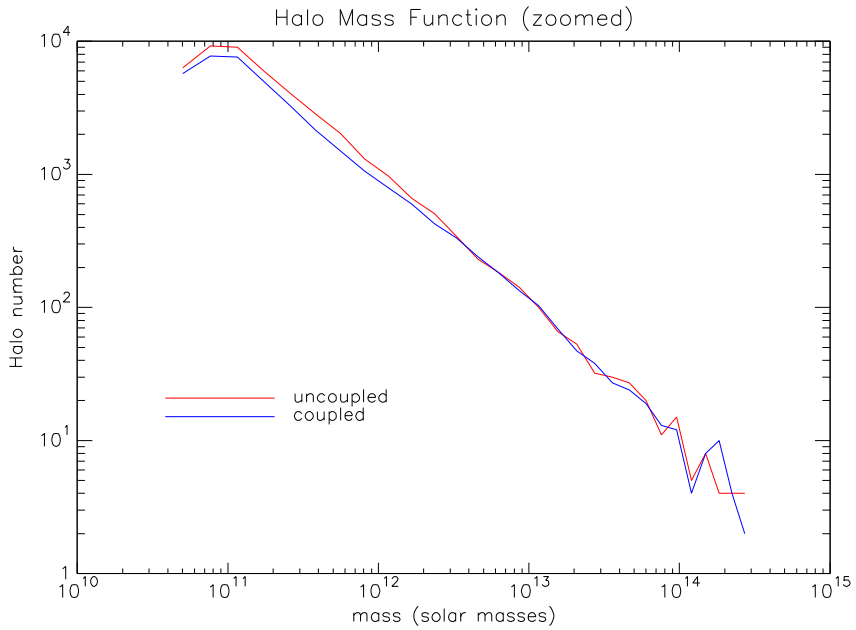

Figure 7.13: As Figure 7.11 but for the zoomed simulations.

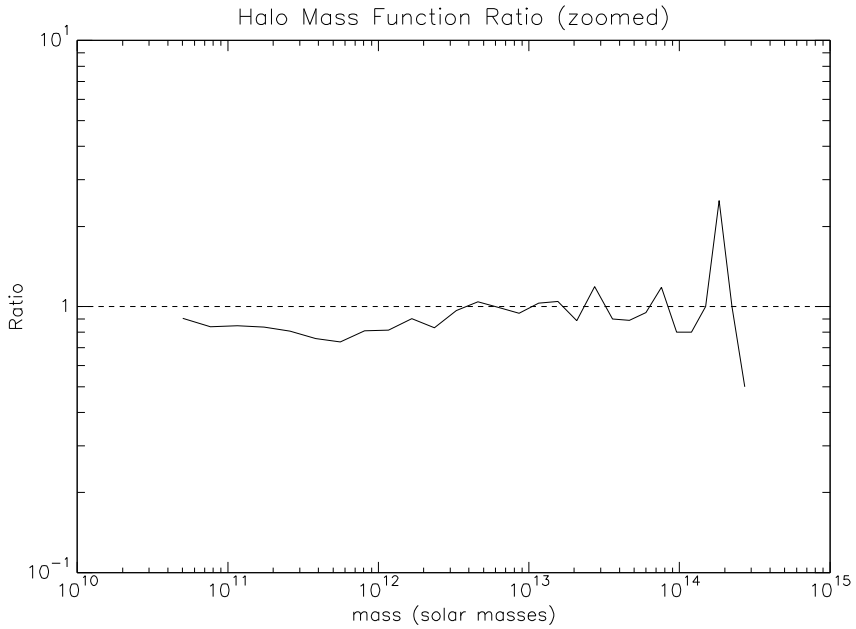

Figure 7.14: As Figure 7.12 but for the zoomed simulations.

Chapter 8

Conclusions

In this Thesis the first series of zoomed simulations of the Multi-coupled Dark Energy model has been presented. The McDE model is characterised by two distinct species of Cold Dark Matter particles coupled with a scalar field which plays the role of Dark Energy. The coupling gives rise to an additional long-range interaction, which can be both repulsive or attractive, depending on the types of the involved particles.
No significant differences with respect to the ΛCDM cosmology are expected both in the background and in the linear perturbations regimes for a coupling giving rise to a fifth force with strength comparable to the gravitational one. However, a series a characteristic features are expected to appear in the non-linear regime, the most remarkable being the fragmentation of cosmological structures into pairs of "mirror" structures. The detailed study of the latter is the main motivation for the development of the simulations presented in this Thesis.

Moreover, one of the main results of the present Thesis is the development of a flexible and robust code for the production of multi-species zoomed initial conditions. It is important to note that the initial conditions produced might be used for a wide range of other applications in computational cosmology. Therefore, the McDE scenario under investigation is just the first one of the many possible applications of the code. The detailed description of a code for the production of zoomed initial conditions I wrote is provided.

8.1 The ZInCo code

The code I developed in order to produce suitable initial conditions for zoomed simulations (called ZInCo) proved to be reliable and sufficiently adaptable to different situations. The initial conditions produced by the ZInCo code turn out to be fully compatible with the simulation code they were produced for (*i.e.* GADGET) and to result in cosmological simulations fully consistent with the usual (*i.e.* non-zoomed) ones.
In particular, as shown in Section 5.3 and Chapter 6, the large scale structure of the zoomed and non-zoomed simulations are the same, allowing a direct comparison between the two of them as desired. This feature is a consequence of the chosen algorithm, which uses as a

starting point high-resolution initial conditions and then dilutes the region outside the one of interest. Such a procedure ensures that the random realization of the initial conditions is the same as the original initial conditions, and thus the "seeds" of the cosmic structures are preserved, even if with different mass resolution.
This has been tested also by checking that the primordial power spectrum of the model imposed in the initial conditions is preserved by the zooming procedure, with the exception of the shot noise due to the reduced number of particles.
Further details of the code are provided in Appendix A, along with a series of benchmark tests. The code has been parallelized through the Message Passing Interface (MPI) and features a number of different input parameters which allow to modify its behaviour in order to match the needs of the simulations to be performed, thereby making the code very flexible and easy to use.

8.2 Zoomed simulations of the McDE model

The ZInCo code has been used to produce a series of cosmological simulations with the aim of studying the details of the segregation process that characterises the McDE model. The simulations were performed relying on the CINECA computing cluster called PLX. The possibility to use such a cluster was granted by winning computational time thanks to a C2 class application for scientific purposes, evaluated and approved by the CINECA referee.
A pair of preparatory simulations were performed with diluted initial conditions, *i.e.* reducing uniformly the resolution of the original initial conditions in the whole simulation box. The original ones feature 1024^3 particles for each species of Dark Matter particles, while the diluted ones feature 256^3 particle for each of them. These simulations, one for the standard ΛCDM model taken as reference and one for the McDE model, were aimed to ensure the goodness of the dilution procedure and to identify a target halo to be studied with the zoomed runs. The halo was chosen among the ones which showed a clear segregation at the final redshift of the diluted simulation, *i.e.* $z = 0$. In particular, it was chosen in such a way to contain a suitable number of sample particles, in order to have statistically significant results, and to produce an acceptably small high-resolution region. The zoomed initial conditions were then produced and the zoomed simulations performed. The outcomes of these simulations partially match with the previous findings related to the specific model, but also show some new features observed for the first time in the simulations presented in this Thesis.

8.3 Early Segregation

On the one hand, the global statistical properties of the simulated system, as the halo mass function or the non-linear matter power spectrum, coincide with the ones observed in earlier lower-resolution simulations of the McDE model. The number of halos is reduced with respect to the ΛCDM model for intermediate masses as a consequence of the

segregation process which splits a single structure into two mirror halos, and consequently the halo number at even lower masses is correspondently increased.
Also the qualitative evolution of the large-scale structure fully reproduces the one observed in earlier simulations. The structures appear to be the same of the ΛCDM model with the exception of the appearance, for enough large coupling strengths, of mirror structures which increase the number of halos present in the simulation box and consequently produces a reduced density contrast between the collapsed regions and the surrounding voids. The latter effect is once again due to the segregation process of the McDE model, which promises to be the main source of constraints on the model and also the main source of interest, for its possible effects on the mass distribution at small scales that have been described in this Thesis.

On the other hand, an important unexpected feature was found. In particular, the earlier low-resolution simulations showed that the fragmentation was expected to occur between redshift $z = 1.5$ and redshift $z = 0.5$. The new zoomed simulations, thanks to their higher resolution in the region where the segregation process takes place, show that the segregation actually starts at significantly higher redshifts, namely between $z = 5$ and $z = 10$. However, the unexpectedness of this result prevented the possibility of accomplishing the detailed study of the process as originally planned, and thus it does not allow to put tighter constraints on the redshift where the segregation process occurs. This is due to the fact that the simulations were set up such to provide a high time resolution at the epochs when the segregation was supposed to occur, and not when it was actually found to occur.
Moreover, the earliness of this process is such that the studied halo is not fully formed, and thus it contains a reduced number of particles. Hence, the statistical noise is significant. However, the available data obtained from the simulations at redshifts $5 < z < 10$ are consistent with a scenario where the particles concentrate around two near cores, which remain close until lower redshift, where they depart from each other.

8.4 Radial Density Profiles

The main analysis of the simulation was performed by investigating the radial density profiles (see Section 4.1.3) of the studied halo, both in the uncoupled, *i.e.* ΛCDM, and coupled, *i.e.* McDE, models.
In the uncoupled case, the profile obtained is steeper near the centre of the halo with respect to the ones usually obtained in numerical simulations of the ΛCDM model. Although the source of steepness is not clear and will be investigated further in the near future, it should be recalled that, a number of other simulations found profiles steeper than the usual NFW one, *e.g.* the Moore profile.
In the coupled simulations, the profiles of the two mirror halos at redshift $z = 0$ were analysed. They turn out to be fully compatible with the one obtained in the uncoupled model, showing that the segregation process does not modify the final profiles of the mirror structures. However, during the process of fragmentation the global profile is modified as

a result of the departing profiles for the different Dark Matter species.
The profile was also analysed at higher redshift, namely at $z = 5$, when the fragmentation process is still in its early stages, and it shows a flattened profile in the inner regions, with a clear core that extends out to a radius $R_S \approx 40\ kpc/h$. This result, if confirmed by further simulations, could help solving the long-standing "cusp-core" problem, consisting in the discrepancy between the steep profiles obtained in ΛCDM simulations and the flatter (cored) profiles observed for Dark Matter-dominated dwarf galaxies.
Such flattened profile, obtained for the first time in the framework of the McDE model by the simulations described in this Thesis, provides a viable solution to the described tension between observations and numerical predictions, since it is obtained using a model which does not feature any appreciable differences both at the background and linear perturbation regimes.

8.5 Problems and Perspectives

It must be said that a series of unsolved problems are present. As first, it is important to specify that the baryons were excluded from the simulations, as a result of their negligible impact on the evolution of the model. However, their impact on the deeply non-linear regime is non-trivial. Thus, in order to produce fully-trustful results also the baryonic component of the matter should be included in the simulations. However, as explained in this Thesis, its impact on the results obtained is estimated to be small.

The discovery of the early segregation requires new simulations to be performed, in order to allow a better analysis of the fragmentation process in its earlier stages. They should feature a higher resolution in the region of interest, since at high redshift the forming halo is composed by a reduced number of particles.
Moreover, since the zoomed simulations allow to study only a single halo of interest for every simulation, in order to reach an acceptable statistical significance a larger number of simulations are required. As the zoomed simulations will pile up, the results obtained will become stronger, if consistent.

Finally, the ZInCo code I developed is suitable for a number of different cosmological simulations which go beyond the McDE model studied in this Thesis. In particular, its uniqueness lays in the possibility of treating at the same time different species of matter during the zoom process. This feature allows to produce zoomed initial conditions for scenarios involving multiple types of matter, which are not usually investigated through zoomed simulations, as *e.g.* mixed Dark Matter (warm and cold Dark Matter, hot and cold Dark Matter, ...) or models featuring massive neutrinos. Moreover, it can be obviously used to produce suitable zoomed initial conditions for cosmological simulations with hydrodynamic, *i.e.* involving baryonic matter, aiming to study *e.g.* clusters of galaxies.
Since the ZInCo code is not bound to necessarily treat multiple species of matter at the same time, it is also suitable for standard cosmological simulations featuring a single species of matter.

Acknowledgements

I would like to thank prof. Lauro Moscardini and Dr. Marco Baldi for their precious help during the whole project, for their willingness and for giving me the opportunity to learn exciting new things.

***

Questa Tesi è sicuramente un passaggio importante del mio personale viaggio. Ci sono molte persone che meritano un ringraziamento, e credo che questa sia l'occasione giusta per mostrare loro la mia gratitudine.

Grazie ai miei genitori, per avermi appoggiato in ogni mia scelta.

Grazie a mia sorella Alice, per aver tenuto sveglio il bambino che c'è in me.

Grazie a Lisa, per essere qui a condividere il mio viaggio.

Grazie a Giacomo, Eugenio e tutti gli altri amici e compagni di avventura, passati e presenti, per aver condiviso esperienze, per l'aiuto e soprattutto per le risate.

Bibliography

[1] F.Zwicky, *Astrophysical Journal* **86**, 217-246 (1937).
[2] M.Baldi, *Annalen der Physik* **524**, 602-617 (2012).
[3] M.Baldi, *MNRAS* **428**, 2074-2084 (2013).
[4] M.Baldi, *Phys. Dark Universe* **3**, 4-17 (2014).
[5] M.Baldi, *MNRAS* **411**, 1077-1103 (2011).
[6] M.Baldi et al., *MNRAS* **403**, 1684-1702 (2010).
[7] A. Piloyan et al., *JCAP* **07-2013**, 042 (2013).
[8] A. Piloyan et al., *JCAP* **02-2014**, 045 (2014).
[9] T.Clifton, C. Clarkson, P. Bull, *Phys. Rev. Lett.* **109**, 051303 (2012).
[10] E. Gaztañaga, R. Miquel, E. Sánchez, *Phys. Rev. Lett.* **103**, 091302 (2009).
[11] M. Persic, P. Salucci, *Mont. Not. R.astr. Soc.* **258**, 14 (1992).
[12] S. Sarkar, *"Frontiers of the Universe" eds L. Celnekier and J. Tran Thanh Van (The Gioi Publishers, 2004)* , 53-63 (2002).
[13] Planck Collaboration, *arXiv:1303.5076* , preprint (2013).
[14] Planck Collaboration, *arXiv:1303.5080* , preprint (2013).
[15] L. Bergström, *Rep. Prog. Phys.* **63**, 793 (2000).
[16] G. Bertone, D. Hopper, J. Silk, *Phys. Rep.* **405**, 279-390 (2005).
[17] A. G. Riess et al., *Astron. J.* **116**, 1009 (1998).
[18] S. Perlmutter et al., *Astrophs. J.* **517**, 565 (1999).
[19] A. Sandage et al., *Astrophs. J.* **653**, 843-860 (2006).
[20] R. Lieu, J. Mittaz, S. Zhang, *Astrophs. J.* **648**, 176-199 (2006).
[21] R. Bielby, T. Shanks, *MNRAS* **382**, 1196-1202 (2007).
[22] W. Freedman et al., *Astrophs. J.* **553**, 47-72 (2001).
[23] M. Bonamente et al., *Astrophs. J.* **647**, 25-54 (2006).
[24] J. H. Jeans, *Phil. Trans. R. Soc. London A* **199**, 1-53 (1902).
[25] P. Coles, F. Lucchin, "Cosmology. The origin and evolution of cosmic structures", ISBN: 978-0-471-48909-2
[26] R. K. Sheth, G. Tormen, *MNRAS* **308**, 119 (1999).
[27] A. Jenkins, C. S. Frenk, S. D. M. White, J. M. Colberg, S. Cole, A. E. Evrard, H. M. P. Couchman, N. Yoshida, *MNRAS* **321**, 372 (2002).
[28] R.H. Brandberg, C. Vafa, *Nucl. Phys.* **B326**, 391 (1989).
[29] S.S. Gubser, P.J.E. Peebles, *Phys. Rev. D* **70**, 123510 (2004).
[30] C. Wetterich, *Astron. Astrophys.* **301**, 321-328 (1995).
[31] R. Bean, E.E. Flanagan, I. Laszlo, M. Trodden, *Phys. Rev. D* **78**, 123514 (2008).

[32] G. La Vacca et al., *JCAP* **0904**, 007 (2009).
[33] J.Q. Xia, *Phys. Rev. D* **80**, 103514 (2009).
[34] M. Baldi, M. Viel, *MNRAS* **409**, 89 (2010).
[35] B. Bertotti, L. Iess, P. Tortora, *Nature* **425**, 374 (2003).
[36] C.M. Will, *Living Rev.Rel.* **9**, 3 (2005).
[37] E. Komatsu et al., *Astrophys. J. Suppl.* **192**, 18 (2011).
[38] A.W. Brookfield, C. van der Bruck, L.M.H. Hole, *Phys. Rev.* **D77**, 043006 (2008).
[39] V. Springel, *MNRAS* **364**, 1105-1134 (2005).
[40] V. Springel, N. Yoshida, S.D.M. White, *New Astronomy* **6**, 79-117 (2001).
[41] http://www.mpa-garching.mpg.de/gadget/
[42] Y. Zel'dovich, *A&A* **5**, 84 (1970).
[43] C. Wetterich, *Nuclear Physics B* **302**, 645-667 (1988).
[44] P.J.E. Peebles, B. Ratra, *Astroph. Journal* **325**, L17-L20 (1988).
[45] R.R. Caldwell, *Brazilian J. of Phys.* **30**, 215 (2000).
[46] L. Amendola, *Phys. Rev. D* **62**, 043511 (2000).
[47] T. Damour, G.W. Gibbons, and C. Gundlach, *Phys. Rev. Lett.* **64**, 123 (1990).
[48] G.R. Farrar, P.J.E. Peebles, *Astrophys. J.* **604**, 1 (2004).
[49] S. Weinberg, *Phys. Rev. Lett.* **59**, 2607 (1987).
[50] S. Perlmutter et al., *Astrophys. J.* **517**, 565 (1999).
[51] A G. Riess, B.P. Schmidt et al., *Astrophys. J.* **560**, 49 (2001).
[52] J. Dubinski, R.G. Carlberg, *Astrophys. J.* **378**, 496 (1991).
[53] W.J.G. de Blok, *Advances in Astronomy* **2010**, 789293 (2010).
[54] A. Klypin et al., *Astrophys. J.* **554**, 903 (2001).
[55] J.E. Taylor, J.F. Navarro, *Astrophys. J.* **563**, 483 (2001).
[56] E. Hayashi et al., *MNRAS* **355**, 794 (2004).
[57] R.A. Flores, J.R. Primack, *Astropys. J.* **427**, L1 (1994).
[58] R. Kuzio de Neray, S.S. McGaugh, W.J.G. de Blok, *Astropys. J.* **676**, 920 (2008).
[59] R.A. Swaters, B. F. Madore, M. Trewhella, *Astrophys. J.* **531**, L107 (2000).
[60] S.D.M. White, J.F. Navarro, A.E. Evrard, *Nature* **366**, 429 (1993).
[61] B. Fort, Y. Mellier, *A&AR* **5**, 239 (1994).
[62] G. Squires et al., *Astrophys. J.* **482**, 648 (1997).
[63] G. Squires et al., *Astrophys. J.* **469**, 73 (1996).
[64] G. Squires et al., *Astrophys. J.* **461**, 572 (1996).
[65] Planck collaboration, *arXiv:1303.5062* , preprint (2013).
[66] J.L. Tonry, *Astrophys. J.* **373**, L1 (1991).
[67] D.A. Vanden Berg, *Astrophys. J. Suppl.* **51**, 29 (1983).
[68] M. Fukugita et al., *Astrophys. J.* **361**, L1 (1990).
[69] K.-H. Chae et al., *Phys. Rev. Lett.* **89**, 151300 (2002).
[70] T.M. Niebauer, M.P. McHugh, J.E. Faller, *Phys. Rev. Lett.* **59**, 609 (1987).
[71] B. Jain, J. Khoury, *Annals of Phys.* **325**, 1479 (2010).
[72] T. Damour, G.W. Gibbons, C. Gundlach, *Phys. Rev. Lett.* **64**, 123 (1990).
[73] W.H. Press, P. Schechter, *Astrophys. J.* **187**, 425 (1974).
[74] M. Kuhlen, M. Vogelsberger, R. Angulo, *Phys. Dark Universe* **1**, 50-93 (2012).
[75] obswww.unige.ch/lastro/conferences/sf2013/pdf/lecture1.pdf

[76] C.C. Dyer, P.S.S. Ip, *Astrophys. J.* **409**, 60-67 (1993).
[77] T. Quinn et al., *arXiv:astro-ph/9710043* , preprint (1997).
[78] http://www.fftw.org/
[79] http://www.mpa-garching.mpg.de/~volker/
[80] S.D.M. White, *arXiv:astro-ph/9410043* , preprint (1994).
[81] www.mpich.org/
[82] www.open-mpi.org/
[83] J.E. Gunn, J.R. Gott, *Astrophys. J.* **176**, 1 (1972).
[84] J.A. Fillmore, P. Goldreich, *Astrophys. J.* **281**, 1 (1984).
[85] Y. Hoffman, J. Shaham, *Astrophys. J.* **297**, 16 (1985).
[86] J.F. Navarro et al., *MNRAS* **349**, 1039 (2008).
[87] B. Moore et al., *MNRAS* **310**, 1147 (1999).
[88] V. Springel et al., *MNRAS* **328**, 726-750 (2001).
[89] V. Robin, W. Ford, *Astrophys. J.* **159**, 379 (1970).
[90] http://www.hpc.cineca.it/hardware/ibm-plx
[91] http://www.rzg.mpg.de/services/computing/hydra
[92] J.S. Kaastra et al., *A&A* **365**, L99-L103 (2001).
[93] O. Valenzuela et al., *Astrophys. J.* **657**, 773 (2007).
[94] M. Stiavelli et al., *The Astronomical J.* **121**, 1385 (2001).

Appendix A

Details and Tests of the ZInCo code

A.1 Input parameters

A brief description of the input parameters which can be set while running the ZInCo code (see Section 5) is provided here:

- **Dilution** is a switch variable; if set to 0 the code performs a zoom, while if set to 1 the code performs a uniform dilution of the simulation box.
- **[Snap/High-Res_ICs/Low-Res_ICs]Dir** is the directory where the [snapshot/high-resolution initial conditions/low-resolution initial conditions] files are memorised.
- **[Snap/High-Res_ICs/Low-Res_ICs]Name** is the name of the [snapshot/high-resolution initial conditions/low-resolution initial conditions] files, without the possible final number in the case of a snapshot spread over multiple files.
- **[SNAP/High-res/Low-res]_fnr** is the number of files containing the [snapshot/high-resolution initial conditions/low-resolution initial conditions].
- **ZoomDir** is the directory where the output of the code is saved.
- **Zoom_fnr** is the number of files upon which the zoomed initial conditions are written.
- **cubes_per_side** is the cubic root of the total number of cubic cells that are produced starting from the entire simulation box.
- **[x/y/z]_c** are the coordinates of the high- and mid-resolution regions centre (default: in the snapshot).
- **r_high** is the radius of the high-resolution regions (default: in the snapshot).
- **r_medium** is the radius of the mid-resolution regions (default: in the snapshot).

- **sm** is the cubic root of the total number of cubes averaged on for the mid-resolution region.
- **sl** is the cubic root of the total number of cubes averaged on for the low-resolution region.

The compilation options the code provides are:

- **[DEBUG/VDEBUG/VINFO]** force the code to print a high number of debug information.
- **PRINTIDSCORR** is used in order to make each processor to write on a file the correspondence between the IDs of the particles copied from the original initial conditions to the zoomed ones.
- **NO_CENTERING_OUTPUT** is used to force the code not to put the high-resolution region at the centre of the output file.

A.2 Benchmark Tests

In this Section the results of a small series of benchmark tests of the ZInCo code will be described.
The code has been tested performing a series of clocked dilutions in different situation. In particular the differences were in

- the initial conditions: the code was run with a series of initial conditions which differ each other both for the number of particles contained in the box and the number of files they are made of. The majority of the tests were made diluting initial conditions containing 256^3 or 512^3 particles per type, both of them spread upon 8 files, but a smaller number of test runs were made using initial conditions containing 1024^3 particles per type;
- the dilution factor: the dilution factor used are "2x", "4x", "8x", "16x". A dilution factor of *e.g.* "2x" means that the final number of particles one eighth (*i.e.* $1/2^3$) of the initial one. Thus, the grater the dilution factor, the smaller the final number of particles;
- the number of used processors: the tests were made using 2, 4, or 12 processors

Every other parameter was kept fixed, including the memory-per-processor and, obviously, the supercomputing cluster used (in this case the PLX cluster, see Section 6.1).

In Figure A.1 is shown the wall-clock time (*i.e.* the real time elapsed between the start and the end of the run) used for a dilution of 2×256^3 (left panel) and 2×512^3 particles (right panel) using different numbers of processors and different dilution factors (the different colors in the plots). The plot clearly shows that the time needed by the code is substantially independent of the dilution factor. This feature is not unexpected, since the

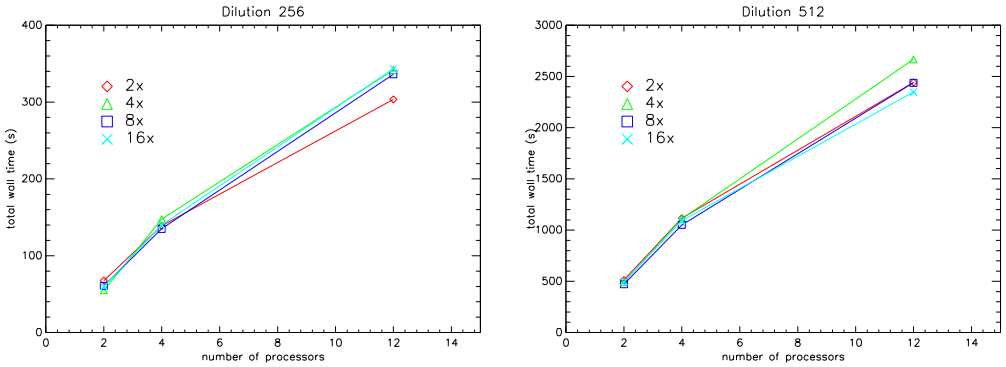

Figure A.1: Wall-time used by different runs of the ZInCo code for two different sets of initial conditions: the ones relative to the left-hand-side panel contain 2×256^3 particles, whilst the ones on the right-hand-side panel contain 2×512^3 particles.

code has to read each particle independently by the final number of diluted particles. The only difference is in the number of average operations (*i.e.* the computation of the center of mass of a group of particles). Since they are much faster with respect to the reading of the particles from the initial conditions files, the elapsed wall-clock time is essentially independent of the dilution factor.

For the same reason, *i.e.* the predominance of the time necessary to the reading of the particles from the file they are written in with respect to the time required by the arithmetical operations performed by the code, there is a large increase of the elapsed time when passing from the initial conditions with 2×256^3 particles to the one with 2×512^3 particles.

At a first glance, it could result surprising that the code does not improve its performances increasing the number of cores but, on the contrary, the elapsed wall-clock time increases for larger number of cores. This is due to the time necessary for the communication between the different cores, which obviously increases as the involved processors increase in number. Thus, the number of processor used should be as small as possible. However, the code has been written in a parallel way since there are cases in which the processors number must be increased. This typically happens when the memory-per-processor is low, or vice versa when the diluted initial conditions contain a high number of particles, and in turn also the original ones do. In the latter cases, the parallelization allows to lower the memory requested by each processor since each of them has to store a smaller number of diluted particles (only the ones relative to the portion of simulation box assigned to it).

A further factor which modifies the time needed by the code is the dislocation of the processors. Typically the processors within the same core of the supercomputing cluster are equipped with a much faster interconnection with respect to the interconnection between different cores. Thus, if the processors used are located in different cores, the measured wall-clock time becomes much greater. Thus, the almost linear growth shown in Figure A.1 is bound to become non-linear as soon as the number of used processors exceeds the number of processors within a single node.

This effect can be qualitatively evaluated running the code on the 2×256^3 particles' initial conditions with two processors located in the same core (named "2 cores") or in different cores (named "1+1 cores") of the PLX cluster. The results are shown in Table A.1, where a significant increase (more than 30%) in the elapsed wall-clock time is found.

	elapsed wall-clock time (s)
2 cores	63.89
1+1 cores	83.53

Table A.1: Comparison between the performances of the ZInCo code run with two processors in the same core (named "2 cores") or in different cores (named "1+1 cores").

As stated earlier, a small number of runs using initial conditions with 2×1024^3 particles were performed. Although not extensive as the ones described above, the results uphold the trends and conclusions obtained for smaller initial conditions. The results available for these larger initial conditions are reported in Table A.2. They show that the wall-clock time is in fact independent of the dilution factor (a dilution factor of 2x or 8x produce a difference in the elapsed time smaller than 16%), whilst it is almost linearly increasing with the number of used processors.

np	dil	elapsed wall-clock time (s)
2	2x	4722.79
4	2x	9504.46
2	8x	3975.27

Table A.2: The available benchmark results for the 2×1024^3 particles initial conditions. "np" is the number of processors used and "dil" is the dilution factor.

Turning to analyse the dependence of the wall-clock time elapsed on the dilution factor used in the simulation, *i.e.* keeping fixed the number of used processors, it turns out that it is almost independent of the dilution factor, as shown in Figure A.2. This conclusion match with the observation that the code must read all the particles in every case, and since this is the most time-consuming operation, the elapsed time is almost constant as long as the same set of initial conditions is used.

The tests described were performed diluting the initial conditions to different final states. However, no significant differences in the performances are expected between the dilution or zooming procedure, with the exception of an increase in the elapsed time independent of the number of processors and roughly proportional to the number of particles present in the initial conditions. These effects are results of two different portions of the code: in the core, where the dilution or zoom take place, no differences are expected since the only difference is that in the first case the code averages over a certain number of particles while in the last case it simply copies the read particles. This operation, however, is much

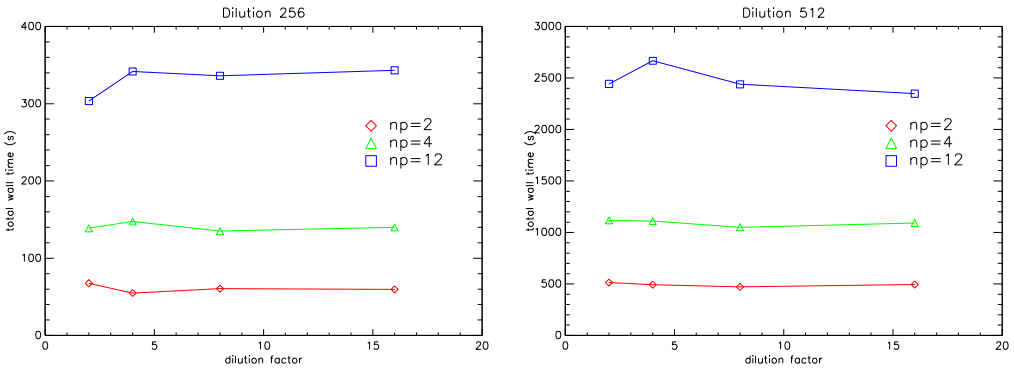

Figure A.2: Wall-time used by different run of the ZInCo code for two different sets of initial conditions: the ones relative to the left-hand-side contains 2×256^3 particles, whilst the one on the right-hand-side contains 2×512^3 particles. The different sets of points (each one of them denoted by a different colour) refer to different series of run using different number of processors (np).

faster than the reading of the initial conditions (as shown before) and thus do not significantly modify the code performance. The real difference is that in the case of a zoom the code must firstly read the snapshot file, identify the regions of different resolutions, trace back the particles to the initial conditions and then compute the new regions of high- and medium-resolution, while in the dilution case all these operations can be avoided, since there is no difference between the particles. Thus, the time employed for these preliminary operations increases the total wall-clock time. For the reasons described above, the added time is substantially independent of the dilution factor. Moreover, since the code performs such computations in a serial way (only one processor does the effective computation and then transmits the results to the other processors), it does not depend on the number of employed processors. However, as the number of particles increases, also the time required for them to be read increases, introducing a dependence on the initial conditions' size.
These conclusions are supported by the benchmark curves obtained for the zoom procedure (instead of the dilution) which are shown in Figures A.3 and A.4 which are similar to the ones discussed above for the dilution procedure.

Moreover, in Figure A.5 I plot only the time employed by the code for the computation of the new high- and medium-resolution regions. It is almost constant for different combinations of number of processors and dilution factors (in the Figure labelled on the x-axis as "run"), as expected, and varies only as a function of the initial conditions, since the number of particles to be read changes.

Finally, in the previous tests the code read the the input files (*i.e.* the initial conditions only, since they all refers to dilutions) with a serial algorithm. In the code it is also possible to perform the reading of the files using a parallel algorithm. However, this results in a very high increase in the wall-clock time employed by the code, as shown in Table A.3

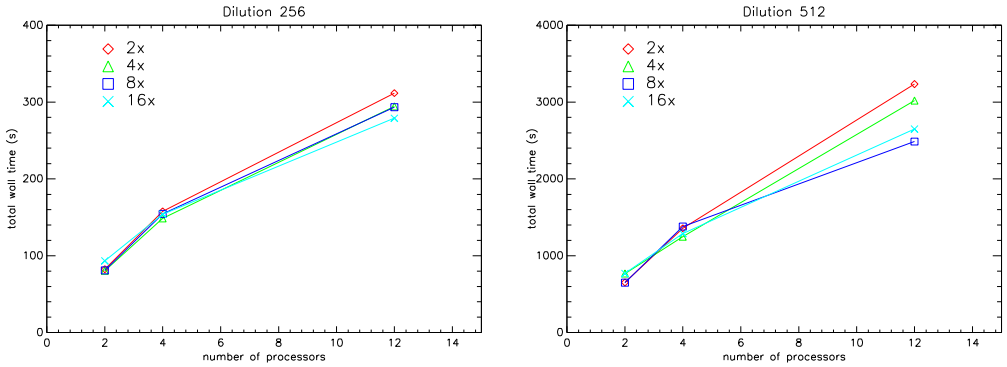

Figure A.3: Wall-time used by different run of the ZInCo code for two different sets of initial conditions: the ones relative to the left-hand-side contains 2×256^3 particles, whilst the one on the right-hand-side contains 2×512^3 particles.

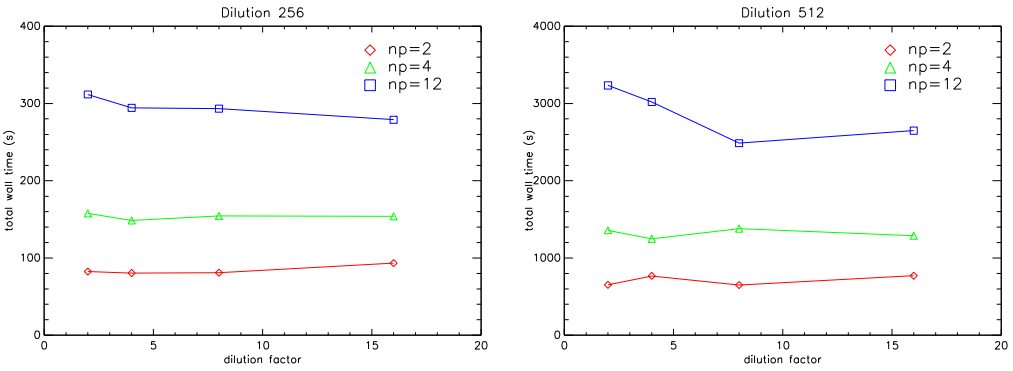

Figure A.4: Wall-time used by different run of the ZInCo code for two different sets of initial conditions: the ones relative to the left-hand-side contains 2×256^3 particles, whilst the one on the right-hand-side contains 2×512^3 particles. The different sets of points (each one of them denoted by a different colour) refer to different series of run using different dilution factors.

where the results for dilutions using different numbers of processors are presented (here, as in Table A.1, "1+1" means two processors located in different cores of the supercomputing cluster) both in the case of serial and parallel reading. In all the cases presented the parallel reading needs more than 45% the time needed by the serial reading. Since the difference in these two cases is just the parallel or serial nature of the algorithm used in reading the files, there are no reasons why this trend should be modified for different initial conditions or dilution factors.

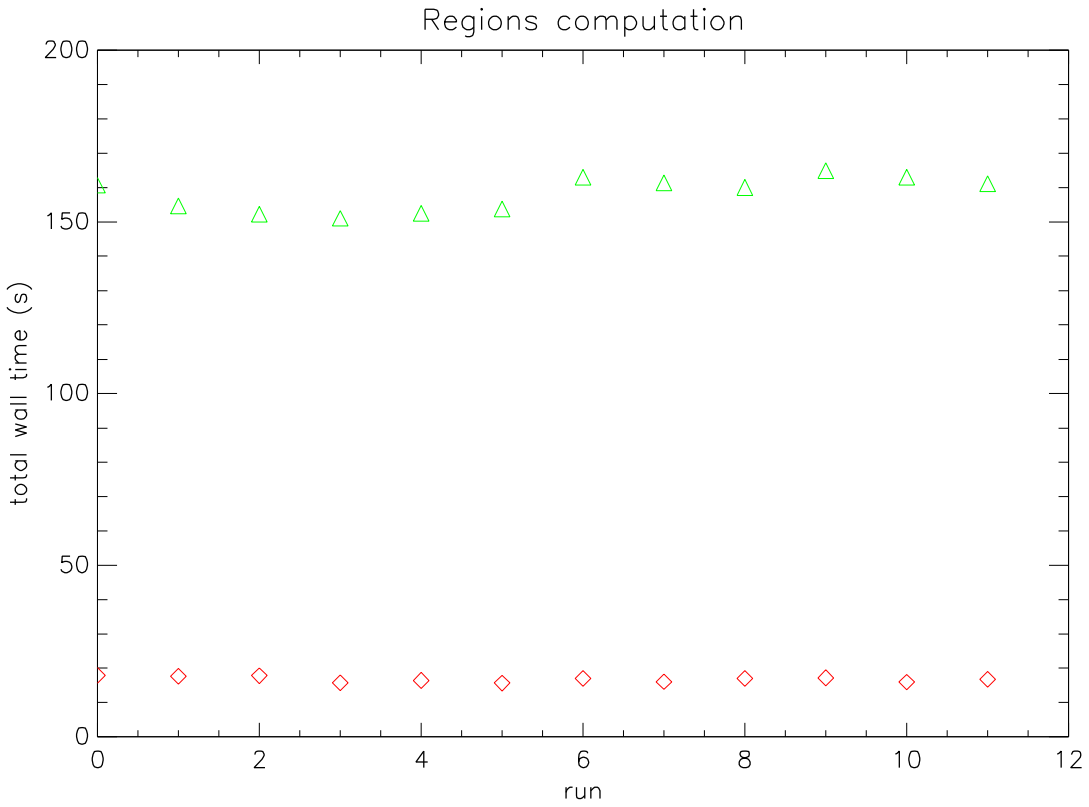

Figure A.5: Wall-clock time employed by the code to compute the new high- and medium-resolution regions for different numbers of processors, dilution factors and initial conditions. The label "run" represents all the possible different combinations of number of processors (2,4,12) and dilution factor (2x, 4x, 8x, 16x).

		wall-clock time elapsed (s)	
np	dil	parallel	serial
2	2	3195.10	67.59
1+1	2	4649.62	83.53
4	2	4750.41	138.83

Table A.3: The available benchmark results for the 2×256^3 particles initial conditions read using both serial and parallel algorithm. "np" is the number of processors used and "dil" is the dilution factor.

Appendix B

The Leapfrog algorithm

The leapfrog algorithm computes the velocity (the so-called "Drift-Kick-Drift") or the position (the so-called "Kick-Drift-Kick") of the particle in the middle of the time-step in order to compute the quantities at the end of the time interval, *i.e.* for an equation like $\ddot{x} = f(x)$ it becomes:

$$\begin{aligned} x_{n+1/2} &= x_n + v_n \frac{\Delta t}{2} & \qquad v_{n+1/2} &= v_n + f(x_n)\frac{\Delta t}{2} \\ v_{n+1} &= v_n + f(x_{n+1/2})\Delta t & \qquad x_{n+1} &= x_n + v_{n+1/2}\Delta t \\ x_{n+1} &= x_{n+1/2} + v_{n+1}\frac{\Delta t}{2} & \qquad v_{n+1} &= v_{n+1/2} + f(x_{n+1})\frac{\Delta t}{2} \end{aligned} \tag{B.1}$$

The leapfrog is a second-order method but, when compared to other algorithms of the same order, it is much more reliable. This is due to the symplectic nature of the leapfrog, *i.e.* it is formulated as a series of symplectic transformations. This fact guarantees that non-Hamiltonian perturbations, which would eventually change the long term behaviour of the system, are not introduced.
Since the Hamiltonian of the system (given by equation 4.30) can be split in a kinetic part and a potential part, the time evolution operator for each part can be computed analytically starting from the canonical transformation for a given time interval Δt, as shown in [77], obtaining the drift $D(\Delta t)$ and kick $K(\Delta t)$ operators. Thus the two schemes described above can be implemented as $U_{DKD}(\Delta t) = D(\Delta t/2)K(\Delta t)D(\Delta t/2)$ and $U_{KDK}(\Delta t) = K(\Delta t/2)D(\Delta t)K(\Delta t/2)$.
The error made using this algorithm can be estimated using $H_{err} \equiv H - H_{approx}$, *i.e.* the difference between the real Hamiltonian and the one of the leapfrog algorithm, which results to be

$$H_{err} = \frac{\Delta t^2}{12}\left\{\{H_{kin}, H_{pot}\}, H_{kin} + \frac{1}{2}H_{pot}\right\} + \mathrm{O}(t^4) \tag{B.2}$$

where "{}" denotes the Poisson brackets.

In order to further improve the integration method, the so-called multi-timestep algorithms are usually employed. In order to have a reliable approximation of the real dynamic

evolution, particles with high acceleration, *i.e.* high forces acting upon them, require a small timestep since the approximations made give results close to the real evolution of the system only for small steps. On the contrary, the evolution of particles with small accelerations can be estimated using a bigger timestep.
In a cosmological simulation there are particles in high-density regions, as the halo cores, that feel a high gravitational field and thus have high accelerations, and also particles in the voids between the halos that experience small accelerations. Running the simulation using the smallest timestep among the timesteps computed for the particles would be a waste of computational time and resources, thus an individual timestep is used for each particle (or group of particles), resulting in an extremely more efficient integration scheme. However, the potential part of the Hamiltonian is not separable in a sum of single-particle Hamiltonians, and thus computing forces only for a group of particles at a certain time can not be done through a symplectic algorithm.
To overcome this problem, the forces acting on a particle can be divided in long- and short-range forces. Thus:

$$H = H_{kin} + H_{sr} + H_{lr} \tag{B.3}$$

and a leapfrog algorithm is used for H_{lr} and $H_{kin} + H_{sr}$ and a sub-leapfrog is applied to the last term, obtaining

$$U(\Delta t) = K_{lr}\left(\frac{\Delta t}{2}\right)\left[K_{sr}\left(\frac{\Delta t}{2m}\right) D\left(\frac{\Delta t}{m}\right) K_{sr}\left(\frac{\Delta t}{2^m}\right)\right]^m K_{lr}\left(\frac{\Delta t}{2}\right) \tag{B.4}$$

An algorithm of this type is implemented as follows: at the beginning (first synchronization point) the force acting on every particle is computed; then, the large-timestep particles are drift-kicked to the next synchronization point, while the short-timestep particles are drift-kicked to the next intermediate point, where the forces acting on them are computed again, and so on until they reach the synchronization point; here again the force is computed for every particle.
Even if this scheme is not formally symplectic, in the case of collisionless dynamics and for a very high number of particles, the particles move in a collective potential and the force between two of them is always negligible when compared to the global force. Under these approximation, the total Hamiltonian can be recast as a sum of single-particle Hamiltonians, justifying the individual timesteps discussed above. Thus, this scheme is expected to reach an accuracy comparable to the one that can be obtained using the symplectic global-timestep leapfrog algorithm. However, the long-term stability that characterizes the fixed-timestep leapfrog is lost in the variable-timestep case, since the variation of Δt introduces a fictional time-dependence in the numerical Hamiltonian. Moreover, the two leapfrog schemes (*i.e.* KDK and DKD) are no longer equivalent, with the KDK which turns out to be four times more precise, *i.e.* it introduces a four times smaller error.

In cosmological simulations, usually the time integration variable is chosen as the logarithm of the expansion factor.

Simulation Boxsize (256^3)	$256\,h^{-1}$Mpc	$64\,h^{-1}$Mpc
Timesteps	2648	5794
Total wallclock time [sec]	60600	173700
Tree walk	52.8 %	41.0 %
Tree construction	4.6 %	6.4 %
Tree walk communication	0.9 %	1.6 %
Work-load imbalance	6.7 %	14.4 %
Domain decomposition	13.0 %	15.2 %
PM force	4.4 %	4.9 %
Particle and tree drifts	5.3 %	4.9 %
Kicks and timestepping	1.4 %	1.1 %
Peano keys and ordering	8.0 %	7.8 %
Misc (I/O, etc.)	2.9 %	2.6 %

Figure C.1: The CPU time consumption of the code, for a given number of particles (256^3) and two different box sizes. The Figure is taken from [39].

Appendix C

Details of the GADGET code

In the present Appendix, some details of the GADGET code are described. In particular, the performance analysis and the available input parameters will be considered.

C.1 Performance

Starting with the performance analysis, in Figure C.1 is reported the time consumption of the code for a given number of particles (256^3) and two different box sizes. Approximatively half of the computation time is used in order to walk the tree, *i.e.* computing the force acting on the particles through a Tree method as described in Section 4.2. Next

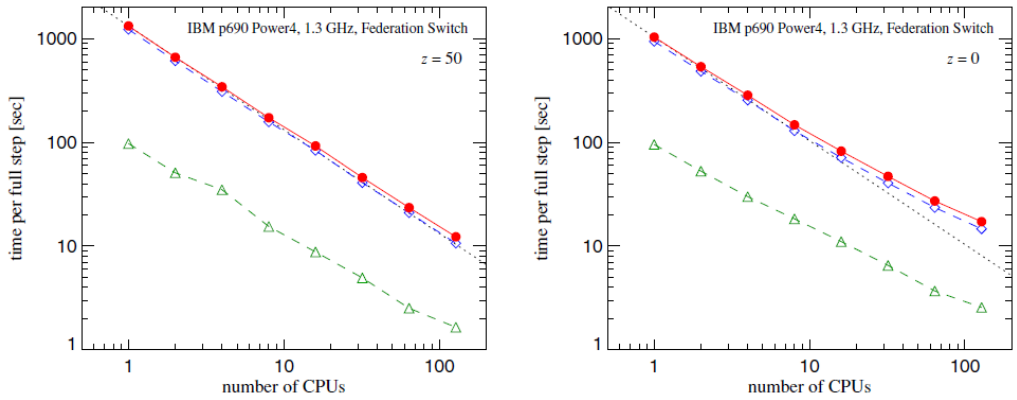

Figure C.2: The time used for each timestep as a function of the number of processors for a clustered (left panel) and un-clustered (right panel) system. The triangles and the diamonds represent the time used for the PM and Tree computation, respectively, while the dots represent their sum. The Figure is taken from [39].

in consumption order is the domain decomposition, while auxiliary tasks like I/O requires only a small percent of the time used by the code.
Moreover, granted that a perfectly linear scalability can not be reached for a number of reasons, mainly the irreducible serial part of the code and the work-balance difficulties that arise when the number of particles per processor becomes small, GADGET provides a good almost-linear scalability as shown in Figure C.2. The scalability of the code is also limited by the fact that the PM part of the code is strongly limited by the performance of the communication network between the processors, while the Tree part is less sensitive to it.
For what concerns the combined impact of system size and processors number on the performances of the code, Figure C.3 shows the wall-clock time needed by a series of simulations, each one of them performed with $\sqrt{10}$ times the number of particles and twice the processors than the previous one. For a perfect scaling, one should find $T_{wall-clock} \propto {}^{N_{particles}}/_{N_{CPUs}}$, *i.e.* a slope of $\alpha \approx 0.4$, while from the plot a slope of $\alpha = 0.52$ is found, slightly steeper.

C.2 Input

Several parameters that characterise the simulation are given to the code through a parameters file which is passed as input parameter when the simulation is run. There are six different supported particle types. By default, the hydrodynamics is applied only to the first one (type 0). Each particle must be labeled in input using a unique ID, *i.e.* an integer number which is different for each particle.
The code reads the initial conditions of the simulation, *i.e.* positions, velocities, masses IDs and internal energies of all the particles, from one or more file(s). It also provides the possibility to print a snapshot at a certain point of the simulation, *i.e.* write all the particles variables in one or more file(s), the number of which can be set in input, along

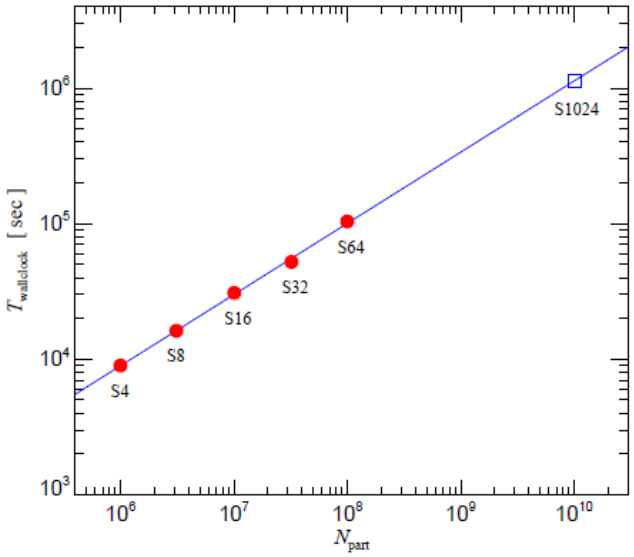

Figure C.3: Total wall-clock time spent by a series of test simulations. The S1024 point is an extrapolation based on the other data. The Figure is taken from [39].

with the output directory. The code can be stopped at any time by creating a file named "stop" in the output directory.
The main parameters that can be set are:

- **InitCondFile** is the location of the file(s) containing the initial conditions;
- **OutputDir** is the directory where the output has to be saved;
- **TimeLimitCPU** is the maximum time allowed for the simulation. The code will automatically stop when the wall-clock time is near the limit set after writing a series of "restartfiles" that can be used to continue the simulation from the point where it has been interrupted;
- **NumFilesPerSnapshot** is the number of files in which a single snapshot is divided;
- **TimeBegin** is the initial time for the simulated system;
- **TimeMax** is the ending time for the simulated system;
- **BoxSize** is the side of the cubic simulation box, expressed in kpc/h;
- **PeriodicBoundariesOn** is a switch used to turn on (1) or off (0) the periodic boundaries;
- **SofteningGas/Halo/Disk/Bulge/Stars/Bndry** are the softening lengths for the six particles types;
- **OutputListFilename** is a file containing a list of time values at which the code has to print a snapshot of the simulation.

The initial conditions and snapshot files can be written in three different ways. The default format is built as a series of blocks, each one of them containing a different quantity about the particles. Every block is preceded and followed by a header containing the length, expressed in bits, of the following/preceding block, respectively. In particular, the blocks are: header (containing global information about the simulation), positions, velocities, IDs, masses (if not the same for all the particles of the same type) and, only for baryon, particles internal energies, smoothing lengths and, only if enabled, gravitational potentials, accelerations, rates of entropy production and timesteps. The main information that is written in the header block is represented by the total number of particles (divided by type) and the number of particles in the present file, the masses of the particles (only if the same for all the particles of a given type), the time and the redshift of the initial conditions/snapshot and the box size.